ABSTRACT

ROYSE, CAMEN ANDREW. Fermi Suppression of Optically Induced Inelastic Scattering: Toward Optical Control of a Weakly Interacting Fermi Gas. (Under the direction of John Thomas).

For small s-wave scattering lengths a_s where energy-changing collisions are negligible, a single, trapped cloud of ultracold fermionic atoms behaves as a lattice in energy space. A radio-frequency pulse coherently prepares a pseudo-spin at each energy site. The site-to-site couplings between spins in the lattice are effectively long-range and proportional to a_s. Optical control of a_s enables tailoring of the site-to-site couplings, opening the door for the simulation of exotic Hamiltonians. This method of control is, however, accompanied by optically induced inelastic scattering, which causes atoms to be lost from the trap and affects the many-body evolution. This loss had not been understood theoretically prior to this work. In this thesis, we develop a model for the loss that accounts for the many-body spin dynamics, and incorporate it into the energy-space spin-lattice model of the weakly interacting Fermi gas. We further report our measurements of the optically induced loss rates to test this model. We find that the loss is strongly suppressed as a_s is increased. The loss suppression occurs as the lattice transitions into a magnetized state, where the fermionic nature of the atoms inhibits interactions. In this way, the loss serves as a probe of the magnetization of the gas. Our observations agree with the model, although the loss constant used in the model is unexpectedly *half* that measured in an incoherent mixture. The success of our loss model enables the application of optical control to this system.

Fermi Suppression of Optically Induced Inelastic Scattering:
Toward Optical Control of a Weakly Interacting Fermi Gas

by
Camen Andrew Royse

A dissertation submitted to the Graduate Faculty of
North Carolina State University
in partial fulfillment of the
requirements for the Degree of
Doctor of Philosophy

Physics

Raleigh, North Carolina
2024

APPROVED BY:

Thomas Schaefer	Lubos Mitas
Kenan Gungdogdu	Brian Space
Ilya Arakelyan	John Thomas Chair of Advisory Committee

BIOGRAPHY

Camen Royse was born in Fort Wayne, Indiana in 1992. He attended high school in Hendersonville, North Carolina and received his Bachelor of Science degree in Physics at North Carolina State University in 2015. He went on to enroll in the same department's Ph.D. program in 2016.

ACKNOWLEDGEMENTS

I would like to thank my advisor Dr. John Thomas, who offered me this opportunity. He is genuine and genuinely cares for his students. He encourages curiosity, and not only answers, but engages with questions. He is able to push his students while remaining open to feedback, and continues to be quick-witted into his seventies. I am lucky to have had him as an advisor.

There is no way for me to properly thank Dr. Ilya Arakelyan, who patiently tolerated my chronic barging-into-his-office. I was quite fortunate to be a beneficiary of all of the time he spent mastering the lab, as well as his well-developed ability to teach and mentor students. He has played a major role in my education so far.

I would like to thank Dr. Jingjing Huang for all of the help, insights, and discussions over the years, and not only in the lab. Like Ilya, I cannot properly thank her, and I am happy that I had the chance to work with her.

I thank Xiang Li for always being flexible as we shared lab space and equipment; Xin Wang, who was always quick to help when he could; and Saeed Pegahan, who helped me get to the point at which I could measure my first spectrum in the lab. I also thank labmates DeChau Zhang and Lorin Baird.

I would like to thank Joel Greenberg for giving me the opportunity to work with him at Duke, and for modeling how to be a young professional. I'm happy to have witnessed Mike Gehm in action while I was there, before I left to work with his same Ph.D. advisor. I also enjoyed working with David Coccarelli during my time there.

I thank Program Coordinator Rhonda Bennett for keeping me aware of all free food options, as well as being a great example of how to handle one's business.

I want to thank so many of the faculty at NC State, not only for their effort in the classroom, but also for giving their time to help direct me as I floundered about. First of all, if not for Albert Young, I would very possibly not be getting a Ph.D. in Physics. When I found myself without academic options, he offered me a position at NC State. In the classroom, I got so much out of Lubos Mitas' Computational Physics course, and being taught by Stephen Reynolds for two of my introductory physics courses was an honor. I also consider myself fortunate for having taken multiple courses with Thomas Schaefer, as well as with David Haase. Laura Clarke, who gave a very strong push to my class, always took the time to give thoughtful advice. Karen Daniels also gave thoughtful advice, and has gone out of her way to help me on multiple occasions. Paul Huffman has helped me as well,

and is always a good guy. I enjoyed my class with David Brown, and appreciate the advice that I've received from David Aspnes. I also thank Leslie Sombers and Lars Dunaway for the research experience that I received as an undergraduate in the chemistry department.

I'm grateful to my high school teachers, in particular Brenda Gorsuch, whose intensity was contagious; Amy Zalevskiy, who was an excellent teacher for my first "hard" science class; and Kerry Ravan, who nutured my interest in calaculus and encouraged the same kind of learning environment that I loved in my university physics courses.

Lastly, I would like to thank close friends and family for their love and support. First and foremost among them being my mother, who raised me on her own. If not for the effort that she put into being a parent, I would certainly not be earning this degree.

TABLE OF CONTENTS

LIST OF TABLES

LIST OF FIGURES

CHAPTER 1

INTRODUCTION

The thermal isolation of trapped, ultracold gases allows the free evolution of a quantum many-body dynamical system to be studied in a laboratory setting. A neutral gas is dilute enough that two-body interactions dominate, and can be cold enough (with atomic speeds on the order of centimeters per second) that only the spherically-symmetric scattered (s-)wave need be considered during an interaction. For ultracold fermionic atoms, the consequence of this spatial symmetry is that the two-atom spin state plays a determining role in the interactions.

Such systems may be manipulated with electromagnetic fields, allowing for the control of the trapping forces, single-atom internal states, and the interactions between pairs of atoms. This toolbox enables some freedom to engineer the Hamiltonian describing the system, and can allow picturesque models of many-body quantum phenomena to be physically realized [Georgescu et al. (2014); Hazzard and Gadway (2023)]. One such tool is the control of the s-wave scattering length a_s using lasers. This enables a_s to vary inside the gas with high spatial resolution, as well as the ability to change a_s in time with high temporal resolution. The drawback is, however, that optical methods induce inelastic scattering, causing atoms to be lost from the trap. Recently, our group has demonstrated a way to significantly reduce this loss and therefore greatly improve the timescales over which experiments can be run with optical control [Jagannathan et al. (2016a); Arunkumar (2018); Jagannathan (2016)]. While the new methods optimize the tradeoff between optically induced loss and tunability of a_s, loss cannot be completely mitigated.

A weakly interacting gas of ultracold fermionic atoms, with spin states coherently pre-

pared orthogonal to an applied magnetic field, exhibits a many body evolution which can be modeled as that of a spin-lattice (i.e., the Ising model) [Du et al. (2008); Pegahan et al. (2019)]. Here, groups of atoms can behave collectively, allowing a gas of $\approx 10^5$ atoms to be conceptualized as $\approx 10^2$ coupled, collective spin vectors. The application of optical control to this system allows the tailoring of the couplings between the spin vectors, whereas non-optical methods only allow the couplings to be scaled globally. Furthermore, the optical control in this system can be used to calibrate a_s as a function of the frequencies and intensities used. The accompanying loss has not been understood in this system, where the atoms are in evolving spin superposition states which scatter in a state-dependent manner.

Motivated by the optical control of the many-body evolution of the weakly interacting Fermi gas, in this thesis, we present a study of the optically induced loss in this system. The effect of loss is incorporated into the spin-lattice model of the weakly interacting Fermi gas, which is shown to be in quantitative agreement with observations. We find that the loss is suppressed by as much as $\approx 45\%$ as a_s is increased due to the the fermionic nature of the atoms.

1.1 Optical Control of Two-Body Interactions in Ultracold Gases

In ultracold atoms that exhibit a magnetic Feshbach resonance, the s-wave scattering length a_s can be continuously tuned from $-\infty$ to $+\infty$ by varying an applied magnetic field. The field strength must be on the order of hundreds of Gauss for alkali atoms. The magnetic field tunes the energy E_T of an incoming pair of atoms for which the valence electrons are in the symmetric spin state $|S=1\, M_S=-1\rangle$. While interacting, the two-electron spin state couples to the anti-symmetric spin state $|S=0\, M_S=0\rangle$, which is a *closed* channel (i.e., the amplitude that the atoms are in the state $|S=0\, M_S=0\rangle$ is zero as $r\rightarrow\infty$) and is associated with a different interaction potential $V_s(\mathbf{r})$. The magnetic Feshbach resonance occurs when the E_T is magnetically tuned to be equal to the energy E_g of a bound state $|g\rangle$ in $V_s(\mathbf{r})$. The atoms exit in the state $|S=1\, M_S=-1\rangle$, with a scattering amplitude which is set by E_T-E_g.

There are other methods of manipulating a_s via applied electromagnetic fields [Bauer et al. (2009); Fedichev et al. (1996); Marinescu and You (1998); Moerdijk et al. (1996)]. While the magnetic field method allows for continuous tuning, it is limited in its spatial and temporal resolution. High spatio-temporal resolution may be obtained using lasers. Lasers can be used to control a_s by either directly coupling an incoming pair of atoms to a

(quasi-)bound state in a closed channel, a so-called "optical Feshbach resonance," or by manipulating the states in the magnetic Feshbach resonance. In either case, the undesirable effects that accompany of optical control of a_s are loss due to spontaneous emission and extraneous trapping forces.

In the optical Feshbach resonance, "a pair of atoms absorbs a photon and undergoes a virtual transition to an electronically excited quasimolecular state. Then it reemits the photon and returns to the initial electronic state at the same kinetic energy" [Fedichev et al. (1996)]. The scattering length is a function of the frequency and intensity. This elastic process is accompanied by inelastic processes, though. Single-atom absorption and emission and decay from a photo-associated state leads to the loss of atoms from the trap.

As an alternative to the optical Feshbach resonance, one may use the magnetic Feshbach resonance in conjunction with optical effects [Bauer et al. (2009)]. As mentioned above, the amplitude of the scattered wave from the magnetic Feshbach resonance is determined by the difference between the incoming energy and the energy of the bound state, $E_T - E_g$. To control a_s, a magnetic field tunes E_T relative to E_g. By using an optical field (i.e., a laser) to couple $|g\rangle$ to an electronically-excited molecular state $|e\rangle$, E_g may be tuned by a light shift. The degree of this shift can be controlled by changing the frequency of the beam (avoiding changes in the intensity avoids changes in the trapping potential). This method comes with less loss than the optical Feshbach resonance. However, loss remains, as energy is deposited into the pair of atoms upon spontaneous emission from $|e\rangle$. This method does not give the infinite tunability that the magnetic field control allows, so the magnetic field can be used to bring a_s close to the desired value, and the optical control beam may be used to vary a_s about this point. In Ref. Clark et al. (2015), this method was used to achieve high tunability by working exclusively near a very narrow Feshbach resonance, where only small shifts in the bound state result in large changes to the scattering length. By working at a "magic wavelength" far off the optical resonance, the states could be shifted without a resulting trapping force (as the states shift the same way for the "magic wavelength"). This allowed the intensity to be used to control the interactions, which made it easy to spatially modulate the scattering length.

Our lab has developed a way to suppress the loss that accompanies the light shift of E_g via Electromagnetically-Induced Transparancy (EIT) [Wu and Thomas (2012b,a); Jagannathan et al. (2016a); Arunkumar (2018); Arunkumar et al. (2018)]. As will be discussed in § 2, the introduction of a second beam allows for control over the amplitude to be in the excited state. The result is that the tradeoff between tunability and loss changes— in the single beam method, maximum tunability of a_s occurs in the same frequency range

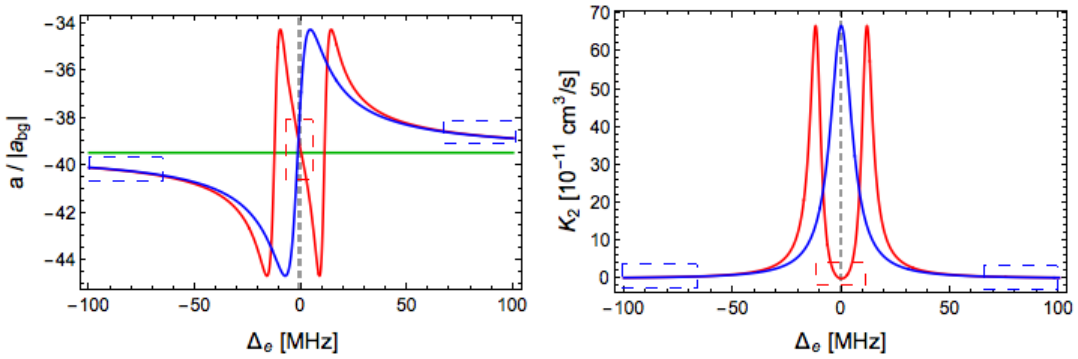

Figure 1.1: Modeling of the tradeoff between tunability of a_s and loss for the single-beam (blue) and two-beam (red) methods of optical control. Here, Δ_e is the detuning of the beam coupling the $|g\rangle$ to $|e\rangle$, $a_s/|a_{bg}|$ is the scattering length in units of the background scattering length (from the triplet channel), and K_2 is the two-body loss constant. The blue boxes emphasize the region of Δ_e for which loss is minimized in the single beam case, which coincides with the points of minimal tunability of $a_s/|a_{bg}|$. In the two-beam case, the red boxes emphasize the point of minimum loss is now at $\Delta_e = 0$, which corresponds to a region of high tunability in $a_s/|a_{bg}|$. This figure was taken from [Jagannathan (2016)].

as the maximum loss point. To reduce loss, one may detune far from resonance, but both the magnitude and the tunability of a_s are very small. With the two-beam method, the frequency range of maximum tunability is the same range as the minimum loss point. This is displayed in Fig. 1.1.

1.2 The Energy-Space Spin-Lattice Model of the Weakly Interacting Fermi Gas

The magnetic Feshbach resonance can be used to reduce a_s so that the rate of energy-changing collisions is negligible on the timescales of the experiment. The motional energies of *individual atoms* are, then, conserved. Interactions still occur in the form of forward s-wave scattering, affecting the spin state of the two interacting atoms. This system has been described as a spin-lattice in energy space, where it is assumed that there is no energy-space coherence (i.e., the atoms are not in superpositions of different motional energy states). Similar to the Ising model of magnetism in a crystal, spins are fixed at energy "sites" and couple to one another. Every spin is coupled to every other spin. This is depicted in Fig 1.2.

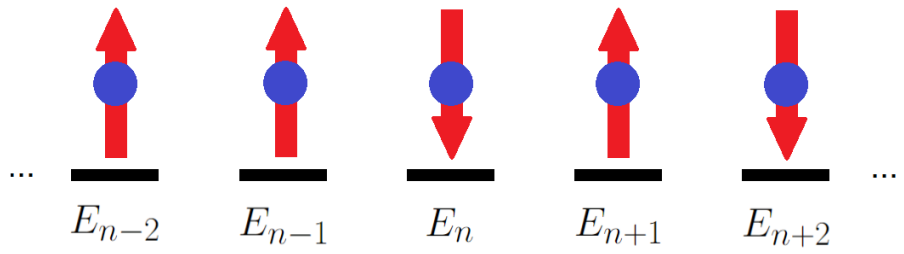

Figure 1.2: A depiction of the energy-space spin-lattice for one energy dimension. Atoms are fixed at energy "sites" labeled by E_n. Each site is associated with a spin vector, and all sites are able to rotate the spin vectors of all other sites. We use a classical implementation of the model, for which the spin vectors have well-defined spatial components in three dimensions.

The spins evolve by a rotation, and thereforehe magnitude of the spin vector at each energy site E, $\mathbf{S}(E)$, is conserved. As we will see in Chapter 3, the evolution equation is

$$\dot{\mathbf{S}}(E) = \mathbf{\Omega_B}(E) \times \mathbf{S}(E) + \sum_{E'} g(E,E')\mathbf{S}(E') \times \mathbf{S}(E) \tag{1.1}$$

where $\mathbf{\Omega_B}(E)$ is the *energy-dependent* precession rate in the magnetic field and the site-to-site couplings

$$g(E,E') \propto \int dx\, |\phi_E(x)|^2 |\phi_{E'}(x)|^2\, a_s \tag{1.2}$$

where $\phi_E(x)$ is the eigenstate of the trap with energy eigenvalue E. The energy-dependent precession rate is essential: the collective spin vectors are coherently prepared orthogonal to an applied magnetic field, and will not interact unless the vectors separate (due to the fermionic nature of the atoms and the spatial symmetry of s-wave scattering). The energy-dependent precession rate enables this, allowing the $\mathbf{S}(E') \times \mathbf{S}(E)$ term to contribute.

The framework for this model was not developed specifically for this system. It originated with the aim of boosting the signal-to-noise ratio in an atomic clock by increasing the density of atoms. In the clock, atoms are illuminated with a beam which cycles the atoms between a ground $|g\rangle$ and an excited $|e\rangle$ state at a (Rabi) frequency Ω_{ge}. The interactions between atoms cause a shift the resonant frequency between $|g\rangle$ and $|e\rangle$. To mitigate this, fermionic atoms, cold enough that only s-wave interactions occur, were prepared in an identical

state and used in the atomic clock. All interactions should, then, be suppressed. However, *density-dependent* shifts were still observed, indicating that the interaction-dependent effect was not suppressed [Campbell et al. (2009)]. The accepted explanation was that inhomogeneities in the illuminating beam caused a differing values of Ω_{ge} for different atoms, which resulted in dephasing, breaking the symmetry and enabling interactions [Gibble (2009)]. These interactions were considered weak enough that the motional energies of the atoms were fixed [Gibble (2009); Rey et al. (2009); Yu and Pethick (2010)], so that only the internal state of the atoms were affected. Here, the two-state atoms constituted "psuedo-spins," but the logic is identical to that of two spin states as described above, with the varying Ω_{ge} playing the role of the $\Omega_B(E)$ in Eq 1.1.

This formalism was applied to the weakly interacting Fermi gas [Koller et al. (2016)] in order to understand the anomalous spin segregation first observed in Ref. Du et al. (2008). Absorption images of a Fermi gas before and after spin segregation are shown in Fig. 1.3. The atoms begin in an identical internal state; a 50-50 superposition of hyperfine states $|1\rangle$ and $|2\rangle$. The presence of interactions, is, however, made apparent as the system evolves towards a state in which one spin state is correlated with atoms in the center of the trap, and the other spin state is correlated with atoms at the edge of the trap. Throughout the evolution, the sum of the two profiles remains fixed. Spin segregation had first been observed in an ultracold bose gas, where it was shown that it could not be a direct consequence of the spin-dependence of the trapping forces, and was instead due to the many-body evolution of the system [Lewandowski et al. (2002); Oktel and Levitov (2002)]. However, the theory used to understand these results did not agree with the results in the Fermi gas [Du et al. (2008)]. The energy-space spin-lattice model, however, was able to reach quantitative agreement with the observed spatial profiles (though, for the higher scattering lengths used, the model disagreed with the measurements for long evolution times) [Pegahan et al. (2019)] .

When the energy-dependent Zeeman precession $\Omega_B(E)$ dominates, the vectors fan out. But when the values of the lattice couplings $g(E, E')$ are increased, this system undergoes a phase transition into a magnetized state. This transition between dynamical phases was observed in Refs. [Smale et al. (2019a), Huang and Thomas (2024)].

1.3 Optical Control in the Lattice

As seen in Eq. 1.2, the lattice couplings $g(E, E')$ can be tuned by changing a_s via the magnetic Feshbach resonance, so long as the rate of energy-changing collisions remains negligible.

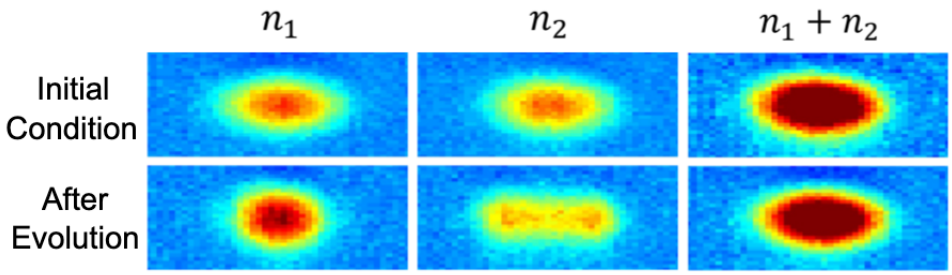

Figure 1.3: Spin segregation in a trapped Fermi gas, with atoms in a superposition of the two lowest hyperfine states $|1\rangle$ and $|2\rangle$. The color scale encodes the density of atoms, with red being the most dense and blue being the least dense. The top row shows the imaged densities n_1 and n_2 of the two spin states before the system evolves, and the bottom row shows the densities after 800 ms of evolution. For the $a_s = 5.2a_0$, the spin state $|1\rangle$ has become correlated with atoms at the center of the trap, and the spin state $|2\rangle$ has become correlated with atoms on the edge of the trap. The sum of these two profiles $n_1 + n_2$ is seen to be constant. The dimensions of the images are $50 \times 950\mu$m. This figure was taken from Ref. [Pegahan et al. (2019)].

The couplings are then *globally* scaled. With the high-resolution spatial control enabled by optical control methods, we can realize $a_s \rightarrow a_s(x)$ in Eq. 1.2. The spatial variation causes the couplings between each pair of energies $g(E, E')$ to change in a unique way. As a simple example, if optical control beams illuminate only the edges of the trap, then only the high-energy sites in the lattice would be coupled to one another. Further, focusing the beam on the center of the trap would result in interactions between atoms with *even* quantum numbers to dominate.

To demonstrate that optical control of a_s is possible in this system, the ultracold gas can be made to be completely non-interactiong ($a_s = 0$) with the applied magnetic field, and then be uniformly illuminated with the optical control beam. If the beam shifts the scattering length, then it will induce spin segregation. We have performed this experiment with our two-beam method, using the detuning of the second beam Δ_2 to tune a_s. The (axial, 1-D) spin densities before and after the evolution are shown in Fig. 1.4. When both beams are on resonance, the amplitude to be in the excited state is zero, and there is no change in the scattering length. We see that, for $\Delta_1 = \Delta_2 = 0$, the spin density profiles are static. This case is identical to that case that no optical control beams are introduced. Tuning Δ_2 to 13.75 MHz, spin segregation is observed, indicating that the scattering length has been shifted by the optical beams. Tuning Δ_2 to -13.75 MHz, spin segregation is again observed with the two spin states exchanged, indicating that the scattering length has again

been shifted by the beams, this time with $a_s \rightarrow -a_s$ from the $\Delta_2 = 13.75$ MHz case. This confirms that the optical control methods may be used to control the evolution of the weakly interacting Fermi gas.

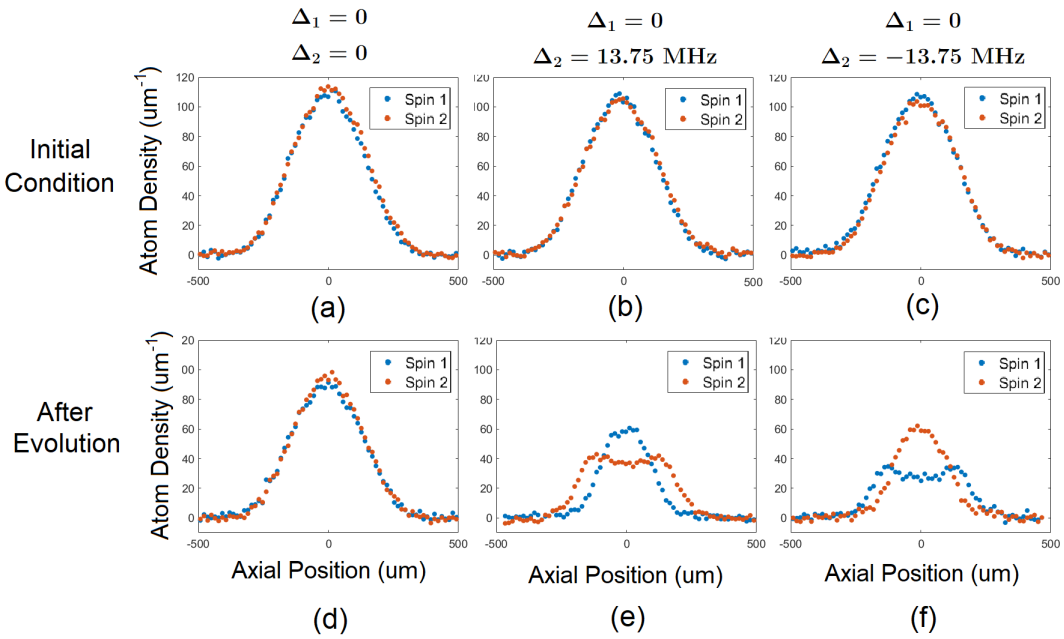

Figure 1.4: Inducing spin segregation by optical control after 300 ms of evolution. The magnetic field is tuned such that $a_s = 0$ and the two optical control beams uniformly illuminate the sample. With both beams tuned to resonance, there is no shift in the scattering length and the axial profile $\int dy\, n(x,y)$ (i.e., obtained summing the 2-D densities over the vertical direction y in Fig. 1.3) is essentially static. a_s is controlled by varying the detuning of the second beam. For positive detuning, the same segregation pattern observed in Fig. 1.3 is reproduced. For negative detuning, the roles of the spin states are exchanged. This occurs in the magnetic tuning case as well when $a_s \rightarrow -a_s$ [Pegahan et al. (2019)].

1.4 Optically Induced Loss in the Lattice

Note that in the Fig. 1.4, the density has decreased after segregation. This is due to the loss that accompanies optical control and affects the many-body evolution of the energy-space spin-lattice. Prior to this work, loss had not been studied in this system— unlike the lossless case, these profiles were unable to be reproduced theoretically. This loss must be

understood in order to apply optical control to this system.

Two-body loss is understood for pairs of atoms in well-defined, distinct spin states undergoing inelastic scattering. In this system, however, the spin states of the atoms are determined by a many-body evolution which arises from the spin-dependent forward scattering. This spin-state dependence of the scattering cross-section is a consequence of the Pauli principle: for fermionic atoms to interact via s-wave scattering, their internal states must differ.

This becomes especially relevant when the spin-lattice evolves into a magnetized state, which occurs at a sufficiently large scattering length [Smale et al. (2019b); Huang and Thomas (2023)]. In this phase, the spin states of all of the atoms are nearly identical, and we would predict that the optically-induced loss would be significantly suppressed. Fermi gases have recently provided new demonstrations of the Pauli principle in degenerate samples, including the suppression of light scattering [Margalit et al. (2021); Sanner et al. (2021); Deb and Kjærgaard (2021)] and the suppression of stimulated emission [Jannin et al. (2022)], which arise from Pauli blocking, where optical momentum transfer to single atoms is inhibited by occupied final momentum states. In contrast, the suppression of light scattering in this system would be both dynamical and collective, emerging from effective long range spin-spin interactions.

1.5 Outline of this Thesis

In this thesis, we generalize the two-body loss model for atoms in an incoherent mixture to account for loss when the atoms are in groups of evolving superposition states. The loss model, which accounts for Fermi suppression, is integrated into the energy-space spin-lattice model of the weakly interacting Fermi gas. Measurements of time evolution of the loss are obtained for different scattering lengths. We obtain measurements which agree with the model prediction, exhibiting a phase transition (Fig. 1.5). The loss is seen to be strongly suppressed —from losing $\approx 60\%$ of atoms to only losing $\approx 15\%$ of the atoms— as a_s is increased from 0 to $24\,a_0$.

In Chapter 2, we discuss the theory relevant to understand the two-body interactions in an ultracold gas for this work. The phenomenological definition of the scattering cross section is given and related to the quantum scattering picture, and the two-body loss equation for an incoherent mixture of (spin) states is obtained. With the necessary theoretical background, the magnetic Feshbach resonance is discussed, followed by a description of

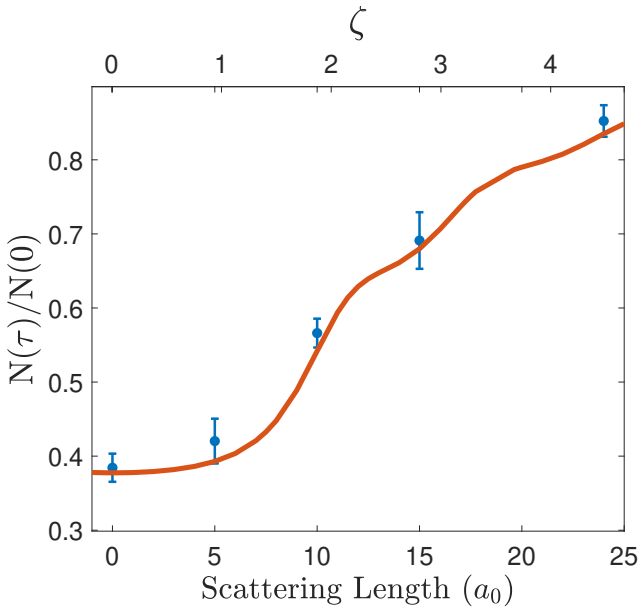

Figure 1.5: Measurements of the atom fraction $N(\tau)/N(0)$ remaining after τ =370 ms of illumination (with a beam tuned to the $|g\rangle \rightarrow |e\rangle$ resonance) as the scattering length is increased (blue points), compared to the prediction of the loss model developed in this thesis (red curve). As the scattering length is increased, the loss is dramatically suppressed, which we interpret to be the result of a phase transition to a magnetized state. The data are also plotted with the interaction strength ζ, which parameterizes the phase transition and will be introduced in § 3. This figure is also displayed in § 5, where it is discussed in detail.

the two-field method of optical control.

In Chapter 3, the energy-space spin-lattice model is derived and an intuitive picture of the spin dynamics is given. The loss model for this system is then derived and integrated into the spin-lattice model, providing all of the tools necessary to simulate the evolution of the system with loss. We finally describe how to measure the the relevant two-body loss constant, which we denote by K_2^a, using light-induced loss in an incoherent mixture.

In Chapter 4, we describe the methods used to physically realize an ultracold gas, starting from a thermal beam of atoms, using optical forces. We also show how the 2-D density of the ultracold gas may be observed. We then provide an overview of the system used to realize two-field optical control, which amounts to the frequency-stabilization of the absolute frequency of each beam as well as the *difference* in frequency between the beams. While the beam causing EIT is not used in our experiments, the entire locking scheme must be understood in order to generate the loss-inducing beam used in the experiment.

In Chapter 5, we describe how the system is prepared in the weakly interacting regime

after ultracold temperatures are reached, both for the coherently-prepared sample used to create the spin-lattice, and for the incoherent 50-50 mixture used to measure K_2^a. The details of how the sample is illuminated with the loss-inducing beam are given. We then report the measurements of K_2^a and of the loss in the coherently-prepared sample. Suppression of the loss is observed as the scattering length is increased. We find agreement between the theory and the measurements, but only if the value of K_2^a is *half* of what we extract from the measurements in the mixture.

In Chapter 6, we discuss this issue of the factor of two in the measurements of K_2^a. We also introduce ideas of how the spin-lattice can be manipulated, with and without optical control. We end on a discussion on possible reasons why the (lossless) model fails for longer evolution times.

CHAPTER 2

TWO-BODY INTERACTIONS IN ULTRACOLD GASES

As mentioned at the beginning of § 1, ultracold gases are dilute enough that two-body interactions dominate. This is why the sample does not naturally condense into a solid or liquid state at the ultracold temperatures— for atoms to bind during a collision, energy must be removed (say, via a third colliding atom). Though the sample is dilute, the ultracold atomic wavepacket is huge, with de Broglie wavelengths that are on the order of the interatomic spacing ($\approx 1\ \mu$m). Since the wavefunctions overlap, quantum statistics is necessary to describe the two-body collisions. The quantum-mechanical nature of the interactions also manifests in energy-dependent scattering resonances. "Controlling the interactions" is equivalent to tuning the difference between the energy of the colliding pair and the resonance energy.

As we will see, *two* potentials are needed to describe two-body s-wave scattering. This is necessary for the existence of a Feshbach resonance, which allows for control of the interactions. By light-shifting the quantum states involved in the Feshbach resonance, the interactions can be controlled optically.

In this chapter, we introduce the phenomenological scattering cross section and relate it to quantities that can be calculated with a quantum mechanical picture of the two-body interaction. We discuss the concepts necessary to understand the magnetic Feshbach resonance, and show how it can be used to tune the s-wave scattering length. Finally, we discuss how the magnetic Feshbach resonance can be optically controlled, and how the

associated loss may be suppressed via our two-field method.

2.1 Basic Scattering Theory

Atomic- or subatomic-scale properties of an unknown "target" substance can be probed via scattering experiments. In these experiments, a flux $\mathscr{F}_P$ of "probe" particles P (from molecules, to atoms, to subatomic particles, to photons) bombards a target T. Particles which come out of the target are then observed. The problem is then to infer the properties of the target based on the distribution of the scattering angle and energy of the redirected probe particles (or other types of particles which come out of the target). In a target with structure, the scattering experiments reveal more than information about the interactions between the probe particles and the particles comprising the target— they can provide information about how the particles are arranged in the target as well. For instance, Rutherford scattering allowed the spatial structure of the atom to be inferred, and Bragg scattering allowed the structure of a crystal to be determined down to the exact spacing between planes.

To extract a quantity that describes the nature of the interaction between the probe and target particles, we think of the target particles as appearing to the probe particles as, say, hard spheres uniformly distributed over the cross-section of the target, with a cross-sectional area σ. Assuming that the area per particle ΔA in the incoming beam of probe particles is much larger than σ, the probability that a probe particle hits a target particle is then $(\Delta N_T\,\sigma)/\Delta A$, where ΔN_T is the number of target particles in ΔA. The fraction of the probe particles incident on this window that are scattered is then equal to this ratio. To get the total number of scattered probe particles, we sum over all possible cross-sectional areas in three dimensions. Taking ΔA to be fixed, the total number of scattered probe particles $N_P^{sc} = N_T\sigma/\Delta A$. We multiply each side of this equation by the rate at which probe particles arrive and obtain the number of probe particles scattered per unit time $\dot{N}_P^{sc}$

$$\dot{N}_P^{sc} = \sigma \mathscr{F}_P N_T. \tag{2.1}$$

This provides our definition of the σ, for a uniform flux $\mathscr{F}_P$ over the target. Note that in practice, σ depends on the relative velocity of the probe and target particles as well. More

generally, we may consider a spatially-varying $\mathscr{F}_P$ and obtain

$$\dot{N}_P^{sc} = \sigma \int d^3\mathbf{r}\, \mathscr{F}_P(\mathbf{r}) n_T(\mathbf{r}) \tag{2.2}$$

where $n_T(\mathbf{r})$ is the three-dimensional density of target particles at location $\mathbf{r}$. Note that we can define a *differential* cross section by measuring the angular distribution of the scattered particles (assuming that the scattered particles are measured far enough away from the target that the position at which the scattering occurred in the target does not matter). In this thesis, we are not concerned with the differential cross section, and will only consider the total cross section. In this definition of σ, we obtain a phenomenological quantity that is specific to the nature of the interactions between probe and target particles (for a given relative velocity).

The theory used to understand the scattering of a probe beam off of a target can, of course, be used to understand the scattering of one atom off of another in our ultracold gas. The same quantities used to obtain σ can be used to understand the interaction-dependent behavior of the gas as a whole. Furthermore, our method of observation, absorption imaging (see § 4.1.5), can be thought as a kind of scattering experiment as described above.

In the following, we relate σ to the quantum picture of scattering and explore the phenomena which arise in this picture.

2.1.1 Quantum Picture of Scattering

In the quantum picture of scattering, the atoms are waves, and the potential acts as an effective refractive index. When a wave encounters a change in the potential energy and the total energy is higher than the new potential, it partially reflects and partially refracts, while the total energy is conserved. If the energy is less than the potential, the wave ceases to oscillate in space, but continues to oscillate in time at the same frequency. We frame the quantum picture of the scattering problem as the following: in the frame of one particle, an incident wave approaches the range of the interaction potential from ∞. Some fraction is transmitted through, and some fraction is scattered. We will relate the amplitude of the scattered wave as $r \to \infty$ to the cross section. We assume that the incident wave is a plane wave, and that the wavefront is much larger than the range of the interaction potential.

To gain some intuition, let us consider a 1-D case with a "box" potential. Working in the frame of one of the particles, $V(x=0) \to \infty$, $V(x<a) = -V_0$, and $V(x \geq a) = 0$. This is depicted in Fig. 2.1. The other particle approaches from $x \to +\infty$, with a wavevector $-\mathbf{k}$,

defined in the relative frame. When it hits $x = a$, most of the wave is transmitted, and some is reflected. The transmitted wave completely reflects off of the infinite repulsion at $x = 0$, and again approaches $x = a$. Here it partially transmits ans partially reflects. The cycle repeats, *ad infinitum*. For this 1D case, the set of waves transmitted in the $+x$ direction out of the region $0 < x < a$ constitute the scattered wave. It is equivalent in wavelength and frequency to the incoming wave, and only differs in the direction it is traveling, its amplitude, and its phase. The last two are intertwined, as we will see in § 2.1.2.

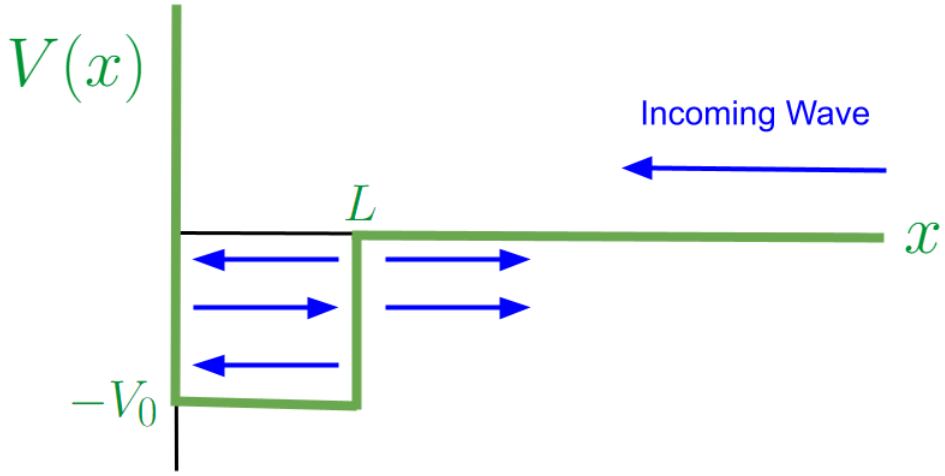

Figure 2.1: Depiction of 1D scattering for a "box" potential $V(x)$. A wave approaches from $x \to \infty$ towards the particle it will scatter off of. When it hits $x = L$, it encounters a non-zero potential $V = -V_0$, causing it to partially reflect and partially transmit. The wavelength of the transmitted wave changes. When the transmitted wave hits $x = 0$, it is completely reflected. Upon hitting $x = L$, the wave partially transmits and partially reflects, and the cycle repeats. The combination of all waves transmitted out of the region $0 < x < L$ constitute the "scattered" wave. Note that the vertical position of the arrows is not representative of the energy.

In three dimensions, the incoming plane wave is scattered in all directions. Working far away from the interaction potential and in the frame of the scattering particle, we write the

total wavefunction after scattering as

$$\psi = A(e^{ikz} + \psi_{sc}) \tag{2.3}$$

where ψ_{sc} is the scattered wavefunction. Since we are considering the region far away from the interaction potential, ψ_{sc} is also a free-particle solution to the Schroedinger equation. A-la Huygen's principle, we write the ψ_{sc} in spherical coordinates (taking only the solution which travels radially outwards)

$$\psi_{sc} = \frac{f_k(\phi,\theta)}{r} e^{ikr} \tag{2.4}$$

where $f_k(\phi,\theta)$ is the scattering amplitude (note from the above equation that it is the *fraction* of the amplitude of the transmitted wave), which can be written as the sum of spherical harmonics $Y_\ell^m(\phi,\theta)$ with coefficients B_ℓ

$$f_k(\phi,\theta) = \frac{1}{k}\sum_\ell \sum_m (-i)^\ell B_\ell^m Y_\ell^m(\phi,\theta) \tag{2.5}$$

Now, we aim to relate this expression for the wavefunction after scattering to the phenomenological quantity σ. We do this by first writing the probability flux associated with the wavefunctions. Since "probability is conserved" we can express

$$\frac{\partial}{\partial t}|\psi(\mathbf{r})|^2 = -\boldsymbol{\nabla}\cdot\boldsymbol{j}(\mathbf{r}). \tag{2.6}$$

Indeed, this is consistent with the Schroedinger equation, where, in the relative frame,

$$\boldsymbol{j}(\mathbf{r}) = \frac{\hbar}{i\mu}\mathrm{Imag}\big[\psi^*(\mathbf{r})\boldsymbol{\nabla}\psi(\mathbf{r})\big]. \tag{2.7}$$

For the incoming plane wave,

$$\boldsymbol{j}_k = |A|^2\frac{\hbar\mathbf{k}}{\mu} \tag{2.8}$$

for the scattered wave,

$$\boldsymbol{j}_{sc}(r) = |A|^2\frac{|f_k(\phi,\theta)|^2}{r^2}\frac{\hbar k}{\mu}\hat{\boldsymbol{r}} \tag{2.9}$$

In Eq. 2.1, we motivated the cross section by thinking in terms of hitting a target. In this picture, where the wavefront is much larger than the range of the potential, the cross section is not dependent on whether or not the target is hit, but rather what fraction of the wave

is scattered. To relate this picture to Eq. 2.1, we can consider only a single pair of atoms, setting $N_T = 1$, $\mathscr{F}_P \to j_k$ and let $\dot{N}_{sc} \to \oint d\mathbf{A} \cdot \boldsymbol{j}_{sc}$ (where the integral is over the surface of a sphere encapsulating the scatterer). With $d\mathbf{A} = r^2 d\Omega \hat{\mathbf{r}}$, we have

$$\sigma = \int d\Omega |f_k(\phi, \theta)|^2. \tag{2.10}$$

This is our connection between the phenomenological and the theoretical. Note that, for indistinguishable particles, the scattered wavefunction must either a symmetric or an antisymmetric. This results in a scattering cross section for indistinguishable particles σ_{ind}

$$\sigma_{ind} = \frac{1}{2} \int d\Omega |f_k(\phi, \theta) \pm f_k(\pi - \phi, \pi - \theta)|^2. \tag{2.11}$$

For a symmetric spatial state, the cross section will double.

To calculate scattering predictions of a known potential $V(\mathbf{r})$, the problem is to find f for $V(\mathbf{r})$ and k. This is not trivial. Using a Green's function approach, a recursive relationship for the scattered wavefunction (the Born series) may be set up. This approach may be used to find perturbative solutions. Limiting ourselves to the first term, we have the "first Born approximation" for the scattering amplitude

$$f_k^{(1)}(\phi, \theta) = -\frac{\mu}{2\pi\hbar^2} \int d^3\mathbf{r}\, V(\mathbf{r}) e^{ikr}. \tag{2.12}$$

Of course, this expression becomes less and less appropriate as the scattered wave amplitude becomes comparable to the incident wave amplitude.

2.1.2 Partial Wave Expansion

We noted in the 1D case that the scattered wave differed only in direction, phase, and amplitude from the incident plane wave (when far away from the range of the potential). While in that case the incident wave and the scattered wave propagated on the same axis, in the 3D case the incident wave and spherically-scattered waves cannot be directly compared. Here we deconstruct the incident plane wave into radial waves, allowing us to use the phase shifts of these radial waves to quantify the scattering. We will show how the amplitude and phase shift for each radial, or "partial" wave, are intertwined.

Expanding the plane wave in the spherical harmonic basis, we can write the incident wave in spherical coordinates. In this basis, the wave is quantized, even though its a free.

This is because a given eigenstate of the wave must constructively interfere with itself as it rotates about a given axis. While this is a seemingly obtuse way to express a plane wave, it will allow us to directly compare the incident wave with the scattered wave. Here we limit ourselves (for simplicity) to the cases in which the scattering amplitude is symmetric for rotations about the direction of the incident wave, $f_k(\phi,\theta)\to f_k(\theta)$. This means that we only consider *central* potentials, $V(\mathbf{r})\to V(r)$. For $r\to\infty$, the incident plane wave may be written as

$$e^{ikz}=\frac{1}{2ikr}\sum_\ell C_\ell(\theta)\left[e^{ikr}-e^{-i(kr-\ell\pi)}\right] \tag{2.13}$$

where $C_\ell(\theta)=P_\ell(\cos\theta)(2\ell+1)$ and the angle θ is defined relative to the direction of the plane wave $\hat{\boldsymbol{z}}$. Now, the total wavefunction Eq. 2.3 for $r\to\infty$ is also a free-particle solution, and, conserving probability, can only differ by a phase shift. So, the total wavefunction after scattering is simply

$$\psi=\frac{A}{2ikr}\sum_\ell C_\ell(\theta)e^{i\delta_\ell(k)}\left[e^{ikr}-e^{-i(kr-\ell\pi)}\right] \tag{2.14}$$

but this means that, from Eqs. 2.3, 2.4, and 2.5, the scattering amplitude is

$$f_k(\theta)=\sum_\ell C_\ell(\theta)\chi_\ell(k) \tag{2.15}$$

where

$$\chi_\ell(k)=\frac{e^{2i\delta_\ell(k)}-1}{2ik} \tag{2.16}$$

In the partial wave expansion, χ_ℓ is the amplitude of partial wave ℓ. We see that χ_ℓ and the phase shift are not independent. The scattering amplitude may then be found by solving the Schroedinger equation with $V(r)$ for the radial wave function and taking the asymptote $r\to\infty$ to compute the phase shift for each partial wave. Keeping $\delta_\ell(k)$ bounded between $\pi/2$ and $-\pi/2$, attractive interactions correspond to $\delta_\ell(k)<0$ and repulsive interactions correspond to $\delta_\ell(k)>0$. That is, the wave fronts are either pulled towards or away from the other particle.

Since the amplitude of each scattered wave can be written in terms of a phase shift and the $P_\ell(\cos\theta)$ are orthogonal, we can associate a different cross section to each partial wave ℓ

$$\sigma=\sum_\ell\sigma_\ell \tag{2.17}$$

then

$$\sigma_\ell=\frac{4\pi}{k^2}(2\ell+1)\sin^2\delta_\ell(k). \tag{2.18}$$

We can, then, imagine the scattering of each partial wave as an independent event.

Each partial wave ℓ is associated with a different rotational "kinetic energy," which is equivalent to an effective potential

$$V_\ell(r) = \frac{\ell(\ell+1)\hbar^2}{2\mu r^2}. \tag{2.19}$$

Thus, the higher ℓ is, the higher the energy of the incident wave needed to "excite" the partial wave ℓ. For low energy collisions, $k \to 0$, and we expect only the partial waves with low values of ℓ to contribute. In this low-energy limit, we expect $\delta_\ell(k) \to 0$. Then,

$$\lim_{k\to 0} \chi_\ell(k) = \lim_{k\to 0} \frac{\delta_\ell(k)}{k}. \tag{2.20}$$

We define the "scattering length" for a given partial wave a_ℓ as

$$a_\ell = -\lim_{k\to 0} \chi_\ell(k). \tag{2.21}$$

Now, for the ultracold temperatures used in our experiments, the $\ell = 0$ wave, or, "s-wave," dominates over the other partial waves (note that $V_{\ell=0} = 0$). Since $P_0(\theta) = 1$, this wave is spherically-symmetric— it has no angular momentum. It can be shown that the phase shift of the s-wave from a hard sphere of radius R is $-kR$. Then, the s-wave scattering length a_s (equivalent to $a_{\ell=0}$) corresponds to the radius of the hard sphere which reproduces the same phase shift as the real interaction potential.

The hard sphere of radius a_s is not the only potential that can be used in place of the real interaction potential to reproduce the same scattering amplitude. If we limit ourselves to the case that the scattered wave is small compared to the transmitted wave, then the first Born approximation Eq. 2.12 becomes an appropriate way to calculate the scattering amplitude from the interaction potential. Now, if we simply want to make the interaction potential result in an s-wave scattering length a_s, we can set

$$V(\mathbf{r}) = \frac{2\pi\hbar^2 a_s}{\mu}\delta(\mathbf{r}) \tag{2.22}$$

we then get back $f_k(\theta) = -a_s$. Note that $a_s > 0$ corresponds to an attractive interaction, and $a_s < 0$ corresponds to a repulsive interaction. For indistinguishable particles with spatial

symmetry, we must set $a_s \to 2a_s$ to obtain

$$V_{ind}(\mathbf{r}) = \frac{4\pi\hbar^2 a_s}{\mu}\delta(\mathbf{r}). \tag{2.23}$$

We refer to potentials that reproduce the desired scattering quantities, without the details of the real interaction potential, as "psuedo-potentials." They prove especially useful when modeling the two-body interactions in an ultracold gas.

2.1.3 Resonances

When conducting scattering experiments, it is found that, as the energy of the incoming particles change, the cross section can increase sharply and peak about a "resonance" energy. This phenomenon is expected from the quantum picture of scattering, and can be understood in terms of simple constructive interference. To see this explicitly for a simple case, recall the 1-D box potential in Fig. 2.1. The amplitude of the wave inside of the range of the potential ($0 < x < a$) will reach its maximum value when all of the waves bouncing back in forth are in-phase ($2k'a = 2\pi n$, where $k' = \sqrt{2\mu(E+V_0)}/\hbar$ and n is an integer). The amplitude of the reflected wave, playing the role of the scattered wave, will also be maximized when all of the waves leaving the range of the potential are in phase, which occurs under the same condition. That is, as the wave "builds up" around the scatterer, it is able to scatter more and more, "leaking" out of the edge of the range of the potential.

In general, if the potential can sustain a wave of frequency ω (that is, if the Hamiltonian has an eigenvalue $\hbar\omega$) then an incoming wave with frequency ω can "couple" to this state, building up the probability amplitude to be in this state by oscillating in-phase with it. The amplitude to be in a given eigenstate will be a function of the difference between the incoming wave energy and the energy of that state. To see this, let the Hamiltonian describing the scattering potential —kinetic and potential— be H_{sc}. We introduce a "driver" Hamiltonian $H_D = E_k |\psi_k\rangle \langle\psi_k|$, which only operates on the incoming plane wave $|\psi_k\rangle = A|\mathbf{k}\rangle$, where $\langle\mathbf{r}|\mathbf{k}\rangle = e^{i\mathbf{k}\cdot\mathbf{r}} = e^{ikz}$, to continuously propagate it through the scattering potential. We express H_{sc} in terms of the eigenstates

$$H_{sc} = \sum_E E\,|E\rangle\langle E| \tag{2.24}$$

We write the total wavefunction as $|\psi\rangle = |\psi_k\rangle + |\psi_{sc}\rangle$. The scattered wave function $|\psi_{sc}\rangle$ comes from the coupling of the incoming wave to the eigenstates of H_{sc}, so we can express

it in the $|E\rangle$ basis

$$|\psi_{sc}\rangle = \sum_E c_E |E\rangle . \tag{2.25}$$

With the driver Hamiltonian acting only on the propagating wave, we search for equilibrium solutions at a sustained vibration given by the incoming energy

$$H_D |\psi_k\rangle + H_{sc} |\psi\rangle = E_k |\psi\rangle \tag{2.26}$$

Since the time-dependence of the plane wave comes entirely from the driver,

$$H_{sc} |\psi\rangle = E_k |\psi_{sc}\rangle \tag{2.27}$$

this results in

$$\langle E|\mathbf{k}\rangle E A + E c_E = E_k c_E . \tag{2.28}$$

$|\psi_{sc}\rangle$ is then

$$|\psi_{sc}\rangle = A \sum_E \frac{E\langle E|\mathbf{k}\rangle}{E_k - E} |E\rangle \tag{2.29}$$

If $E_k = E$, the ratio of the amplitude to be in the state $|E\rangle$ to the amplitude of the outgoing plane wave approaches ∞. That is, *all of the incoming wave is scattered*, and the cross section hits its maximum value. This is a *resonance*— when the energy of the incoming wave is equal to the energy of an eigenstate $|E\rangle$ of the scattering potential, so long as $\langle E|\mathbf{k}\rangle \neq 0$. The equal energies correspond to equal oscillation frequencies, allowing $|\psi_k\rangle$ and $|E\rangle$ to oscillate in-phase so that $|\psi_k\rangle$ "pumps" directly into the state $|E\rangle$.

Since the energy of the incoming, free particle must be equal to the energy of an eigenstate in order to achieve resonance, it appears impossible to resonate with a bound state. Indeed, the concept doesn't even appear to make sense, as a the wavefunction of a bound state decays to zero for $r \to 0$, by definition. It is possible for the incoming particle to come in with a negative energy by introducing an offset energy $-U_0$ over all space (by, say, an interaction of the internal state with a uniform external field). However, this shifts the energy of the eigenstates as well, so that $E_k \to E_k - U_0$ and $E \to E - U_0$, resulting in no change to $E_k - E$. As will be discussed in § 2.2, however, it *is* possible to resonate with a bound state when multiple scattering "channels" are present.

2.1.4 Multiple Channels and Inelastic Scattering

In the quantum picture of scattering discussed so far, we've limited ourselves to elastic scattering— the internal state and total energy of the outgoing particles is identical to those of the incoming particles. It is possible that, during a scattering experiment, the probe particles emerge from the target in a different internal state and with a different energy than the incident beam. Or, some fraction of the probe particles do not emerge at all. Or, fundamentally different particles emerge. We refer to scattering of this sort as *inelastic* scattering. The different possible states that the pair of particles can be in during the scattering event are referred to as "channels." The quantum picture of scattering now goes beyond mere wave mechanics: *all* possible channels are simultaneously taken during the collision.

For two channels $|\alpha\rangle$ and $|\beta\rangle$, the scattering Hamiltonian now takes the form

$$H_{sc} = H_\alpha |\alpha\rangle \langle\alpha| + H_\beta |\beta\rangle \langle\beta| + \mathscr{C} |\beta\rangle \langle\alpha| + \mathscr{C}^* |\alpha\rangle \langle\beta| \tag{2.30}$$

where H_α and H_β are the kinetic energy and interaction potential operators for a a pair of particles in the two-particle states $|\alpha\rangle$ and $|\beta\rangle$, and $\mathscr{C}$ describes the coupling between the two states. It is possible that the potentials (external and interaction) can be different in the two states, so that the total potential in the interaction is

$$V(\mathbf{r}) = V_\alpha(\mathbf{r}) |\alpha\rangle \langle\alpha| + V_\beta(\mathbf{r}) |\beta\rangle \langle\beta| . \tag{2.31}$$

This opens up the possibility that the incoming pair of free particles couple to a channel with a potential from which they cannot escape. Such a channel, which is taken during the interaction but cannot be occupied by the scattered particle, is referred to as a "closed channel." Note that the particles return to the free state, since the coupling allows the particles to exit in "open" channel. Since the input channel must be open, there is always at least one open channel. It is then possible for elastic scattering to occur with multiple channels, if all channels are closed other than the input channel.

Separate cross sections can be defined for elastic events and and for inelastic events. The elastic cross section σ_{el} we define according to Eqs. 2.17 and 2.18, where $\delta_\ell(k)$ is the phase shift associated with the incoming state (i.e., the input channel). We note that the scattering amplitude associated with the other channels cannot be expressed as a phase shift, as they cannot be combined with the incoming wave. Since some of the wave is lost to other channels, the elastic cross section should be smaller than in the case that there

is no inelastic scattering. We can account for this by allowing for complex phase shifts $\delta_\ell(k) = \delta_\ell(k)' + i\delta_\ell(k)''$ (where $\delta_\ell(k)'$ and $\delta_\ell(k)''$ are real), with $\delta_\ell(k)'' > 0$ (note that this results in a complex scattering length). Computing σ_ℓ from Eq. 2.16, we see that $\delta_\ell(k)'' > 0$ will reduce this value, as desired. Now, the total cross-section σ_{tot}, which accounts for all scattering events can, remarkably, be expressed in terms of the elastic scattering amplitude in the direction of the incident beam $f_k(\theta = 0)$

$$\sigma_{tot} = \frac{4\pi}{k}\text{imag}\big[f_k(\theta = 0)\big] \tag{2.32}$$

(see the Optical Theorem). Then, the inelastic cross section σ_{inel} can be isolated and expressed in terms of the (complex) phase shift of the elastically-scattered wave

$$\sigma_{inel} = \sigma_{tot} - \sigma_{el} = \frac{\pi}{k^2}\sum_\ell (2\ell+1)(1-|e^{2i\delta_\ell(k)}|^2). \tag{2.33}$$

The form of the inelastic cross section is then to something we'd expect— if $\delta_\ell(k)'' = 0$, there is no inelastic scattering.

In this thesis, we will be concerned with inelastic two-body scattering in a trapped ultracold gas. In a gas, there are no "probe" and "target" particles; all interactions happen internally. We may still make use of Eq. 2.2 by expressing the flux in terms of the density

$$\mathscr{F}(\mathbf{r}) = v_{rel}\, n(\mathbf{r}) \tag{2.34}$$

We will consider the case that the atoms interact only if one atom is in a state A and the other is in a state B. From Eqs. 2.2 and 2.34, we can define a density of inelastic collisions $n_{IC}(\mathbf{r})$ between atoms in each state with a relative speed v_{rel}

$$\dot{n}_{IC}(\mathbf{r}) = \sigma_{inel}^{AB}\, v_{rel}\, n_A(\mathbf{r}) n_B(\mathbf{r}) \tag{2.35}$$

where $\dot{N}_A^{sc} = \dot{N}_B^{sc} = \int d^3\mathbf{r}\, \dot{n}_{IC}(\mathbf{r})$, $n_A(\mathbf{r})$ is the density of atoms in state A, $n_B(\mathbf{r})$ is the density of atoms in state B, and σ_{inel}^{AB} is the inelastic cross section between atoms in states A and B. Note that $n_A(\mathbf{r}) = n(\mathbf{r})\rho_{AA}$ and $n_B(\mathbf{r}) = n(\mathbf{r})\rho_{BB}$ (where ρ is the density matrix and $n(\mathbf{r})$ is the total gas density) are well-defined only when the gas is in an incoherent mixture of the states states A and B (that is, $\rho_{AB} = \rho_{BA} = 0$). If an inelastic collision jettisons the interacting atoms out of the trap, then $\dot{n}_A(\mathbf{r}) = \dot{n}_B(\mathbf{r}) = -\dot{n}_{IC}(\mathbf{r})$, and we have

$$\dot{n}_A(\mathbf{r}) = \dot{n}_B(\mathbf{r}) = -K_2^{AB} n_A(\mathbf{r}) n_B(\mathbf{r}) \tag{2.36}$$

where $K_2^{AB} = \langle v_{rel} \sigma_{inel}^{AB} \rangle$ is averaged over all relative speeds.

2.2 The Feshbach Resonance

As we saw in § 2.1.3, a resonance occurs when the energy of the incoming particle approaches the energy of an eigenstate of the system. We noted that, since the incoming energy could not be made equal to the energy of a bound state, resonance can only occur with unbound eigenstates. While the energy of the incoming state can be made negative, the energy of the bound state would be equally shifted. Furthermore, resonance with a bound state appeared paradoxical, since the wavefunction approaches zero as $r \to \infty$. This analysis, however, was limited to a *single-channel* collision. Here we will show that a different type of resonance, a "Feshbach" resonance, is possible when multiple scattering channels are present.

Consider two channels, with a scattering Hamiltonian H_{sc} of the form given in Eq. 2.30. Let the atoms approach each other in the two-atom (internal) state $|\alpha\rangle$. The interaction between atoms when they are in this state is described by the potential $V_\alpha(\mathbf{r})$. We introduce a negative energy offset $-U_\alpha$, constant over all space, for atoms in the state $|\alpha\rangle$ (which can be realized by introducing a uniform external field which interacts with the internal state of the atom). Without any coupling to other scattering channels during the interaction, the atoms scatter off of $V_\alpha(\mathbf{r})$, and resonate if the incoming energy is equal to the energy of a free eigenstate. Let the eigenvalues be E_α when $U_\alpha = 0$, and let the eigenstates with the arbitrary U_α be $|E_\alpha\rangle$. Then,

$$H_\alpha = \sum_{E_\alpha} (E_\alpha - U_\alpha) |E_\alpha\rangle \langle E_\alpha| \tag{2.37}$$

Note that the incoming energy has also been shifted, $E_k \to E_k - U_\alpha$.

Now, with $\mathscr{C} \neq 0$ in Eq 2.30, the atoms couple to another two-atom state $|\beta\rangle$ during the interaction. The interaction between atoms in this state is described by the potential V_β. The offset energy for atoms in this state is $-U_\beta$, and we have

$$H_\beta = \sum_{E_\beta} (E_\beta - U_\beta) |E_\beta\rangle \langle E_\beta| . \tag{2.38}$$

If $U_\alpha > U_\beta$, *the energy of the incoming state can be made equal to the energy of a bound state in* V_β. The incoming wave may then "build up" around the atom in the $|\beta\rangle$ channel, and scatter away as it couples to the unbound states in the $|\alpha\rangle$ channel.

To see this, we may repeat the analysis from § 2.1.3 using Eqs. 2.30, 2.37, and 2.38. In the steady state,

$$|\psi_{sc}\rangle = \sum_{E_\alpha} c_{E_\alpha} |E_\alpha\rangle |\alpha\rangle + \sum_{E_\beta} c_{E_\beta} |E_\beta\rangle |\beta\rangle . \tag{2.39}$$

As in Eq. 2.27, we have, since $E_k \to E_k - U_\alpha$,

$$H_{sc} |\psi\rangle = (E_k - U_\alpha) |\psi_{sc}\rangle \tag{2.40}$$

where H_{sc} is given by Eq. 2.30, the total wavefunction $|\psi\rangle = |\psi_k\rangle + |\psi_{sc}\rangle$, and the incoming wavefunction $|\psi_k\rangle = A|\mathbf{k}\rangle |\alpha\rangle$. This results in the coupled equations

$$(E_\alpha - U_\alpha)\langle E_\alpha|\mathbf{k}\rangle + (E_\alpha - U_\alpha)\frac{c_{E_\alpha}}{A} + \mathscr{C}^* \sum_{E_\beta} \frac{c_{E_\beta}}{A}\langle E_\alpha|E_\beta\rangle = \frac{c_{E_\alpha}}{A}(E_k - U_\alpha) \tag{2.41}$$

$$(E_\beta - U_\beta)\frac{c_{E_\beta}}{A} + \mathscr{C}\langle E_\beta|\mathbf{k}\rangle + \mathscr{C}\sum_{E_\alpha} \frac{c_{E_\alpha}}{A}\langle E_\beta|E_\alpha\rangle = \frac{c_{E_\beta}}{A}(E_k - U_\alpha) \tag{2.42}$$

where all coefficients are initially zero. Note that if $\mathscr{C} = 0$, we recover Eq. 2.28 for the $|\alpha\rangle$ channel with the shifted energy. We consider a single (bound) eigenstate in the $|\beta\rangle$ channel, $|E_\beta\rangle$. Then,

$$\frac{c_{E_\beta}}{A} = \frac{\mathscr{C}}{\Delta}\left[\langle E_\beta|\mathbf{k}\rangle + \sum_{E_\alpha} \frac{E_\alpha - U_\alpha}{E_k - E_\alpha}\langle E_\alpha|\mathbf{k}\rangle\langle E_\alpha|E_\beta\rangle\right] \tag{2.43}$$

$$\frac{c_{E_\alpha}}{A} = \frac{E_\alpha - U_\alpha}{E_k - E_\alpha}\langle E_\alpha|\mathbf{k}\rangle + \frac{\mathscr{C}^*}{E_k - E_\alpha}\langle E_\alpha|E_\beta\rangle\frac{c_{E_\beta}}{A} \tag{2.44}$$

where

$$\Delta = E_k - U_\alpha - E_\beta + U_\beta - |\mathscr{C}|^2 \sum_{E_\alpha} \frac{|\langle E_\alpha|E_\beta\rangle|^2}{E_k - E_\alpha}. \tag{2.45}$$

We see that a single-channel resonance occurs for $E_k \to E_\alpha$, and another resonance occurs for $\Delta \to 0$. If $U_\alpha - U_\beta$ can be made positive enough, this can occur when $|E_\beta\rangle$ is a bound state ($E_\beta < 0$). While the bound state wavefunctions $|E_\beta\rangle$ go to zero for $r \to 0$, the free-particle solutions $|E_\alpha\rangle$ "carry a piece" of the amplitude to be in this state, as seen in Eq. 2.44. Taking $(E_k - U_\alpha) < (E_\beta - U_\beta)$, the $|\beta\rangle$ channel is closed, and the scattering is *elastic* (i.e., the atoms exit in the collision in the same state in which they entered). We call this type of resonance a "Feshbach Resonance."

The significance of the Feshbach resonance for ultracold gases is that the amplitude of the scattered wave can be tuned by changing Δ in Eq. 2.45. Whereas, in a scattering

experiment, E_k is usually varied; in a gas, the distribution of E_k is set by the temperature. One can, however, reach $\Delta \to 0$ by varying $U_\alpha - U_\beta$. This is typically done via magnetic tuning.

2.2.1 Magnetic Tuning

Here we will show how a Feshbach resonance may be realized in a gas of (ultracold) alkali atoms by applying a magnetic field $\mathbf{B}$. The states $|\alpha\rangle$ and $|\beta\rangle$ used above will here refer to singlet (antisymmetric) and triplet (symmetric) states of the two-*electron* spin state, formed by the valence electron from each atom. The energy offsets $-U_\alpha$ and $-U_\beta$ are introduced by the Zeeman tuning of these states in $\mathbf{B}$, which differ due to the different magnetic moments of each state. The symmetric and antisymmetric states are associated with different effective interaction potentials. As we will see, the hyperfine interaction plays the role of $\mathscr{C}$.

Consider a single alkali atom j in a magnetic field $\mathbf{B}$. To describe the spin interactions, we consider only the nucleus, with a spin operator $\hat{\boldsymbol{I}}_{\boldsymbol{j}}$ (which may be bosonic or fermionic) and the single valence electron, with an intrinsic spin operator $\hat{\boldsymbol{S}}_{\boldsymbol{j}}$. We include contributions from the hyperfine interaction, the interaction of the intrinsic electron spin with the field, and the interaction of the intrinsic nuclear spin with the field to obtain the Hamiltonian

$$\hat{H}_{in}^{j} = A_{HF}\, \hat{\boldsymbol{I}}_{\boldsymbol{j}} \cdot \hat{\boldsymbol{S}}_{\boldsymbol{j}} + C_e\, \hat{\boldsymbol{S}}_{\boldsymbol{j}} \cdot \mathbf{B} - C_n\, \hat{\boldsymbol{I}}_{\boldsymbol{j}} \cdot \mathbf{B}. \tag{2.46}$$

where $C_e > 0$ and $C_n > 0$. Note that we have neglected spin-orbit coupling, since, for the alkali atoms, the valence electron has $\ell = 0$. Due to the much larger mass of the nucleus compared to the electron, $C_e >> C_n$, so the magnetic tuning is dominated by the two *electron* spin state. Now consider a pair of interacting atoms 1 and 2. The total Hamiltonian describing the dynamics of the internal spins is

$$\hat{H}_{in}^{1} + \hat{H}_{in}^{2} = A_{HF}\, \hat{\boldsymbol{I}}_{\mathbf{2}} \cdot \hat{\boldsymbol{S}}_{\mathbf{2}} + A_{HF}\, \hat{\boldsymbol{I}}_{\mathbf{1}} \cdot \hat{\boldsymbol{S}}_{\mathbf{1}} + C_e\, \hat{\boldsymbol{S}}_{\boldsymbol{T}} \cdot \mathbf{B} - C_n\, \hat{\boldsymbol{I}}_{\boldsymbol{T}} \cdot \mathbf{B} \tag{2.47}$$

where $\hat{\boldsymbol{S}}_{\boldsymbol{T}} = \hat{\boldsymbol{S}}_{\mathbf{1}} + \hat{\boldsymbol{S}}_{\mathbf{2}}$ and $\hat{\boldsymbol{I}}_{\boldsymbol{T}} = \hat{\boldsymbol{I}}_{\mathbf{1}} + \hat{\boldsymbol{I}}_{\mathbf{2}}$. Note that the terms $\hat{\boldsymbol{I}}_{\mathbf{1}} \cdot \hat{\boldsymbol{S}}_{\mathbf{2}}$ and $\hat{\boldsymbol{I}}_{\mathbf{2}} \cdot \hat{\boldsymbol{S}}_{\mathbf{1}}$ do not appear, which can be shown rigorously. Due to the hyperfine coupling this Hamiltonian, cannot be expressed in terms of the total electron spin or nuclear spin. In other words, the *single-atom* spin evolution results in a coupling of the two-atom spin state:

$$\hat{\boldsymbol{I}}_{\mathbf{2}} \cdot \hat{\boldsymbol{S}}_{\mathbf{2}} + \hat{\boldsymbol{I}}_{\mathbf{1}} \cdot \hat{\boldsymbol{S}}_{\mathbf{1}} = \sum_{S,M_s,I,M_I} \mathscr{C}_{S,M_s;I,M_I} |S\, M_s\rangle |I\, M_I\rangle \langle I\, M_I| \langle S\, M_s| \tag{2.48}$$

where S is the total electronic spin quantum number and I is the total nuclear spin quantum number of the two-atom system. During the interaction, then, a given input channel in the $|S\,M_s\rangle\,|I\,M_I\rangle$ basis is coupled to the other two-electron spin and two-nuclear spin states. Expressing the above coupling term with raising and lowering operators, it can be shown that only states that share the same the total magnetic quantum number $M = M_s + M_I$ are coupled.

The magnetic moment of $|S\,M_s\rangle$ is proportional to M_s, and the magnetic moment of the $|I, M_I\rangle$ is proportional to M_I. Since $C_e >> C_n$ in Eq. 2.47, the total Zeeman energy of the two-atom spin state is approximately $\propto M_s B$. This allows the energy difference between channels with differing values of M_s to be tuned.

Now, the interaction between atoms in the symmetric two-electron spin states $|S=1\,M_s\rangle$ is described by a *different effective potential* than the interaction between atoms in anti-symmetric two-electron spin state $|S=0\,M_s=0\rangle$. This is a consequence of the symmetry requirements of the total state upon exchange of the electrons. In the Born-Oppenheimer approximation, the total two-atom wavefunction $|\Psi\rangle$ for the spin state $|S\,M_s\rangle\,|I\,M_I\rangle$ in the center-of-mass frame may be written as

$$|\Psi\rangle = \psi(\mathbf{r_1^e}, \mathbf{r_2^e}, \mathbf{R})\,\chi(\mathbf{R})|S\,M_s\rangle\,|I\,M_I\rangle \tag{2.49}$$

where $\mathbf{r_j^e}$ is the position of electron j, $\mathbf{R}$ is the relative position between the two nuclei, and $\psi(\mathbf{r_1^e}, \mathbf{r_2^e}, \mathbf{R})$ is the molecular electronic state. The exchange of the electrons must result in $|\Psi\rangle \rightarrow -|\Psi\rangle$. The $|S=1\,M_s\rangle$ state must then be associated with an antisymmetric $\psi(\mathbf{r_1^e}, \mathbf{r_2^e}, \mathbf{R})$, and the $|S=0\,M_s=0\rangle$ state must be associated with a symmetric $\psi(\mathbf{r_1^e}, \mathbf{r_2^e}, \mathbf{R})$ upon exchange of $\mathbf{r_1^e}$ and $\mathbf{r_2^e}$. Since an antisymmetric spatial wavefunction vanishes as a pair of particles approach one another, the effective potential associated with the symmetric spatial state (the singlet spin state) $V_s(\mathbf{r})$ will be much deeper than the effective potential associated with the antisymmetric spatial state (the triplet state) $V_T(\mathbf{r})$. Note that we have neglected the nuclei in this discussion, whose wavefunction does not affect the overall interaction potential as much as the two-electron wavefunction. For bosonic (fermionic) nuclei, the exchange of the nuclei must result in $|\Psi\rangle \rightarrow (-)|\Psi\rangle$. The exchange of the nuclei positions results in $\mathbf{R} \rightarrow -\mathbf{R}$. If $\psi(\mathbf{r_1^e}, \mathbf{r_2^e}, \mathbf{R})$ can be approximated by

$$\psi(\mathbf{r_1^e}, \mathbf{r_2^e}, \mathbf{R}) \propto \phi(\mathbf{r_1^e} - \mathbf{R/2})\phi(\mathbf{r_2^e} + \mathbf{R/2}) \pm \phi(\mathbf{r_1^e} + \mathbf{R/2})\phi(\mathbf{r_2^e} - \mathbf{R/2}) \tag{2.50}$$

then the exchange of nuclei position gives the same result as the exchange of electron

positions. Since $\chi(\mathbf{R})$ is symmetric for s-wave scattering, the spatial wavefunction of the two-atom state $\psi(\mathbf{r_1^e}, \mathbf{r_2^e}, \mathbf{R})\,\chi(\mathbf{R})$ is always *symmetric* upon exchange of the two atoms (nuclei and electrons). Bosonic (fermionic) atoms must then be symmetric (antisymmetric) in the total spin $|S\,M_s\rangle\,|I\,M_I\rangle$.

If a bound state exists in $V_s(\mathbf{r})$, we have the ingredients for a Feshbach resonance: the energy of an incoming free atom state with $|S=1\,M_s=-1\rangle$ may be tuned into resonance with a bound state in the $V_s(\mathbf{r})$ potential with $|S=0\,M_s=0\rangle$ via an applied magnetic field. The hyperfine coupling Eq. 2.48 allows the interacting atoms to couple to the bound state. This is how the s-wave scattering length is controlled in ultracold alkali gases.

2.2.2 Application to Ultracold ^{6}Li Atoms

Our experiments employ ultracold ^{6}Li atoms. These atoms are fermionic, with a bosonic nucleus of $I_1 = 1$. The two-atom state $|\Psi\rangle$ is then symmetric upon exchange of the two nuclei. Since $|\Psi\rangle$ is antisymmetric upon exchange of the two electrons, $|\Psi\rangle$ is antisymmetric upon exchange of the two atoms (electrons and nuclei).

In ^{6}Li, the triplet potential $V_T(\mathbf{r})$ has a near-zero-energy s-wave resonance, resulting in a *huge* s-wave scattering length of $a_s = -2160a_0 \approx -0.1\ \mu$m when the atoms are ultracold (i.e., near zero energy), the largest known for any atomic system [Abraham et al. (1997)]. The singlet potential $V_s(\mathbf{r})$ supports multiple bound states, much deeper than the zero-energy resonance in $V_T(\mathbf{r})$. To reach these energies by tuning the $|S=1\,M_s=-1\rangle$ two-electron spin state, magnetic fields on the orders of hundreds of Gauss are required.

A single ^{6}Li atom has $(2\times1+1)\times(2\times\frac{1}{2}+1)=6$ total spin states via Eq. 2.46, which are well-separated in energy at these high magnetic fields (see Fig. 2.2 and § A). We label these states $|1\rangle-|6\rangle$ in order of increasing energy. The energies of states $|1\rangle-|3\rangle$ become more negative in an applied magnetic field, and the energies of states $|4\rangle-|6\rangle$ become more positive in an applied magnetic field. Due to their fermionic nature, atoms in identical internal states cannot undergo s-wave scattering. Pairs of atoms in different states have different scattering properties. This is partially due to the differing amplitudes of the two-atom states associated with singlet and triplet configurations, and partially due to the coupling to other channels (i.e., $|5\rangle$ and $|4\rangle \rightarrow |3\rangle$ and $|2\rangle$). Scattering channels are coupled together via Eq. 2.48, and an incoming combinations of states can leave in a different combination of lower-net-energy states. This releases energy, which can be large enough to jettison atoms from the trap when then incomin states include states $|4\rangle-|6\rangle$ and the outgoing states include $|1\rangle-|3\rangle$. Limiting ourselves to states $|1\rangle-|3\rangle$, we close off the $|4\rangle-|6\rangle$ channels to the

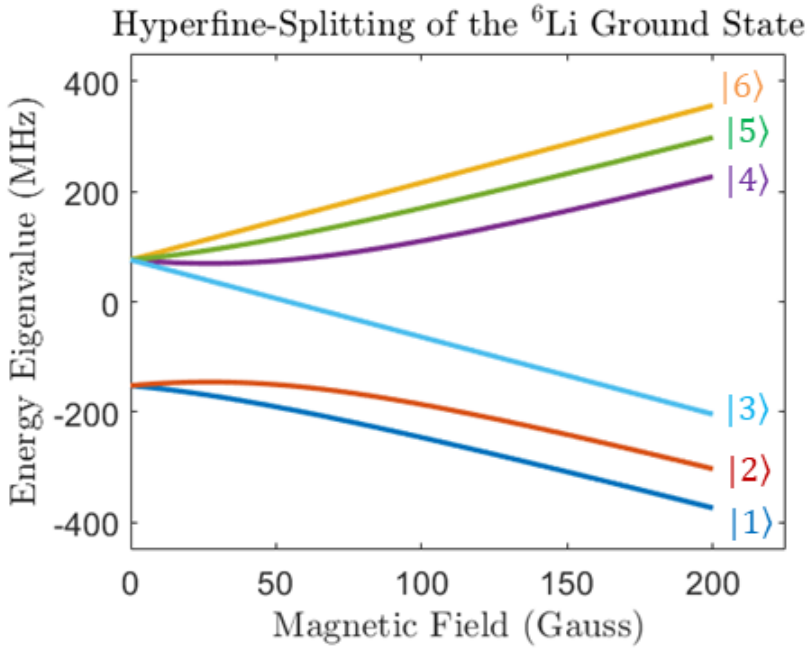

Figure 2.2: Magnetic field-dependence of the six eigenstates of ^{6}Li, with the valence electron in the ground state. Explicit formulae for the energies are given in § A.

other states and avoid these sorts of inelastic collisions. To work with a completely stable system (i.e., where the open input and output channels are the same for all collisions), we work with a mixture of atoms in the $|1\rangle$ and $|2\rangle$ states. These states have a net magnetic quantum number $M = M_s + M_I = 0$, the hyperfine coupling Eq. 2.48 can only couple to channels with total $M = 0$. Since the state which is tuned near the Feshbach resonance has $M_s = -1$, the nuclear spin must have $M_I = 1$. The bound state, with $M_s = 0$, must also have $M_I = 0$.

There are two possible $M_I = 0$ states with the appropriate symmetry: $|I = 0\, M_I = 0\rangle$ and $|I = 2\, M_I = 0\rangle$. Two orthonormal linear combinations of these states results in two Feshbach resonances in the $|1\rangle - |2\rangle$ mixture. The "broad" resonance is at $B = 832.2$ with a width of 300 G, and the "narrow" resonance is at $B = 543$ G with a width of 0.1 G. As can be inferred from Eqs. 2.43 and 2.44, these widths are connected to the coupling constant. Indeed, the hyperfine coupling for the bound responsible for the broad resonance is 131.6 MHz, and the hyperfine coupling for the bound responsible for the narrow resonance is 5.9 MHz. Near the narrow resonance, there is a non-neglibable probability of inelastic three-body collisions. In this work, we avoid the narrow resonance.

2.2.3 Formation of Feshbach Molecules

Tuning the magnetic field near the Feshbach resonance, the atoms are in a superposition of the elastically-scattered states (in the triplet channel) and molecular states (in the singlet channel). By sweeping the the magnetic field closer to zero ("downwards"), the energy difference between the states changes in time, and it is possible to "dump" atoms into the molecular state— that is, the probability can be made much higher for the atoms to be in the bound state than in the free state.

This is a well-known phenomenon (the Landau-Zener effect; [Zener (1932)]) in coupled two-level systems, which we will here use as a model for the Feshbach resonance. Consider a coupled, two-level system

$$H = E_1 |1\rangle \langle 1| + E_2 |2\rangle \langle 2| + \mathscr{C} |1\rangle \langle 2| + \mathscr{C}^* |2\rangle \langle 1| . \tag{2.51}$$

Now, let $E_2 \to E_2(t)$. Writing the state as

$$|\psi\rangle = b_1(t) e^{-iE_1 t/\hbar} |1\rangle + b_2(t) e^{-iE_1 t/\hbar} |2\rangle , \tag{2.52}$$

the Schroedinger equation gives

$$\lambda b_2(t) = i \dot{b}_1(t) \tag{2.53}$$

$$\omega(t) b_2(t) + \lambda^* b_1(t) = i \dot{b}_2(t) \tag{2.54}$$

where $\lambda \equiv \mathscr{C}/\hbar$ and

$$\omega(t) = \frac{E_2(t) - E_1}{\hbar}. \tag{2.55}$$

The equations can be decoupled to give

$$\ddot{b}_1(t) + i\omega(t)\dot{b}_1(t) + |\lambda|^2 b_1(t) = 0 \tag{2.56}$$

$$\ddot{b}_2(t) + i\omega(t)\dot{b}_2(t) + |\lambda|^2 b_2(t) + i\,\dot{\omega}(t) b_2(t) = 0. \tag{2.57}$$

With $\dot{\omega} = 0$, the system undergoes normal Rabi oscillations. Now, we turn on a linear sweep $\omega(t) = \omega(0) + \gamma t$. What happens?

In the figure, we show a numerical simulation of the probabilities for the above equations. Note that $b_1(t)$ and $b_2(t)$ have been renormalized at every time step, i.e., $|b_1(t)|^2 + |b_2(t)|^2 = 1$ is enforced at every time step. The timescale is chosen to be the initial Rabi period, $T_{R_0} = 2\pi/\Omega_{R_0}$, where $\Omega_{R_0} = \frac{1}{2}\sqrt{\omega(0)^2 + 4|\lambda|^2}$. Initially, the probability to be each state oscillates

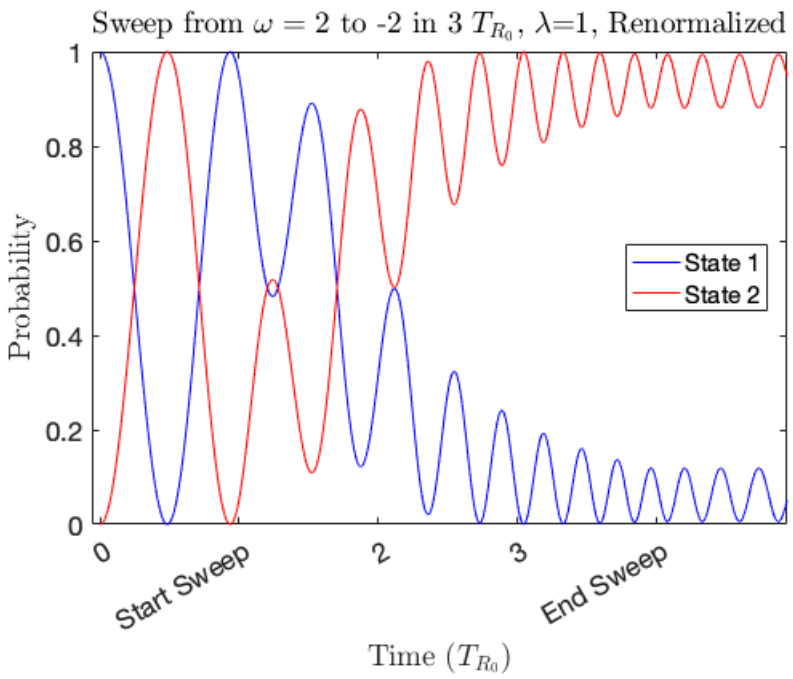

Figure 2.3: Probability of a two-level system to be found in each state, when the energy of state 2 changes linearly in time. The time scale is chosen to be the initial Rabi period T_{R_0}. Before the sweep begins, $(E_2(0)-E_1)/\hbar = \omega(0) = 2\lambda$. The linear sweep begins at $t_{on} = T_{R_0}$ and ends at $t_{off} = 4\,T_{R_0}$. The final value of the energy difference is $\omega(T_{off}) = -2\lambda$. Here, $\lambda = 1$ and the probability amplitudes are renormalized at every time step.

between 0 and 1, with $\omega(0) = 2\lambda$. At $t = T_{R_0}$, the sweep begins, with $\gamma = -4\lambda/(3\,T_{R_0})$. While the ramp is on, it becomes more and more likely that the system is in state 2. At $t = 4\,T_{R_0}$, the sweep is terminated. The system is now most likely to be found in state 2 throughout the evolution for $t > 4\,T_{R_0}$.

Sweeping the magnetic field across the Feshbach resonance has the same effect. Starting above resonance in the open channel, sweep the magnetic field downward causes the continuum states to turn into bound states adiabatically. We refer to these occupied states as "Feshbach molecules."

2.3 Optical Control of the Magnetic Feshbach Resonance

The scattering amplitude is a function of the differences between the incoming energy and the energy of the eigenstates. In the magnetic Feshbach resonance, the energy of the incoming state is tuned to the energy of a bound state $|g\rangle$. The interactions may also

be controlled by tuning the energy of the bound state. This can be done with a "light-shift," where a near-resonant laser changes the energy of the states it drives transitions between [Townes (1955)]. In the rotating wave approximation, the effect of the laser can be incorporated into the scattering Hamiltonian as

$$H_{sc} \rightarrow H_{sc} + \frac{1}{2}\Omega_1 e^{i\Delta_1 t} |e\rangle |s\rangle \langle s| \langle g| + h.c. \tag{2.58}$$

where Ω_1 is the Rabi frequency of the beam, $|e\rangle$ is an electronically-excited molecular state, Δ_1 is the detuning of the beam from the $|g\rangle \rightarrow |e\rangle$ resonance, $|s\rangle$ denotes the anti-symmetric (singlet) two-electron state, and $h.c.$ denotes the Hermitian conjugate. The states $|g\rangle$ and $|e\rangle$ are no longer eigenstates of the singlet-channel; the states are now "dressed" by the field. The light shift is computed from the eigenstates of these "dressed states." To second order, the shift is approximately $\Omega_1^2/(4\Delta_1)$.

The scattering length may then be controlled by changing Δ_1 or Ω_1. The introduction of the optical field results in an extra trapping potential to the gas (see § 4.1.4). This is undesirable if the only purpose of the laser is to change the scattering length, but it can be made to be small compared to the trapping potential. To control the interactions without having to be concerned with changing optical forces, Δ_1 can be tuned exclusively.

The drawback to this method is that spontaneous emission from $|e\rangle$ deposits energy into the interacting atoms, enough that they are jettisoned out of the trap. The rate of spontaneous emission is approximately proportional to Ω_1^2/Δ_1^2. This limits the tunability of the scattering length and the timescale over which experiments may be run. By working far away from resonance, the loss rate can be lowered, but at the cost of a decrease in the light shift. Furthermore, the region of maximum tunability in the scattering length ($\Delta_1 \rightarrow 0$) overlaps with the region of maximum loss. The magnetic field may be used to bring the scattering length close to the desired value, and the laser may be used to change the scattering length around this value. In Ref. [Bauer et al. (2009)], this technique was used to shift the magnetic field at which the Feshbach resonance occurs.

2.3.1 Two-Field Method

To what degree can the light shift be preserved while reducing the loss? The loss mechanism is spontaneous emission from the excited state. However, we cannot arbitrarily reduce the excited state population, since the effect of the laser on the interactions is a result of the transitions it drives between $|g\rangle$ and $|e\rangle$. So we must ask: how can we drive electronic

transitions in the molecular state, while reducing the probability to be in the $|e\rangle$?

We do this by tuning a second laser to drive transitions between $|e\rangle$ and a second ground state $|g_2\rangle$ in the potential $V_s(\mathbf{r})$, as shown in Fig. 2.4. This is incorporated into the total Hamiltonian Eq. 2.58 by adding on another coupling term

$$H_{sc} \rightarrow H_{sc} + \Omega_2 e^{i\Delta_2 t} |e\rangle |s\rangle \langle s| \langle g_2| + h.c. \tag{2.59}$$

where Ω_2 is the Rabi frequency of the second beam and Δ_2 is the detuning of the second beam from the $|g_2\rangle \rightarrow |e\rangle$ resonance. The amplitude transferred to $|e\rangle$ from the first ground state $|g_1\rangle = |g\rangle$ can then be transferred to $|g_2\rangle$. The two-beam configuration effectively introduces two "paths" to $|e\rangle$: one directly from the first ground state $|g_1\rangle \rightarrow |e\rangle$ from the first laser, and another from $|g_1\rangle \rightarrow |e\rangle \rightarrow |g_2\rangle \rightarrow |e\rangle$ by both lasers combined. These paths can interfere, affecting the amplitude to be in the excited state $|e\rangle$. When the two beams are equally detuned from their resonances ($\Delta_1 = \Delta_2$), the relative phase is π for the state $|e\rangle$, so that the probability to be in the excited state is *zero*. Without any scattering of the laser from spontaneous emission, the atoms have become transparent to it. This phenomenon is called "Electromagnetically-Induced Transparency" (EIT). At this zero-loss point, there is no light shift and therefore no effect on the atomic interactions. Deviations in one of the laser frequencies re-introduce electronic transitions in the molecule, which introduce both loss and a change in the interactions. In contrast with the single-field method, however, the zero-loss point sits in a region of maximum tunability (Fig. 1.1).

To control the interactions, then, the magnetic field can be tuned to bring the scattering length close to the desired value, and then the beams may be introduced with $\delta = \Delta_2 - \Delta_1 \neq 0$. The scattering length is tuned with δ, which must be stabilized at a faster rate than the rate of spontaneous emission from $|e\rangle$. Using this technique, the shift in the magnetic field at which the Feshbach resonance occurs has been demonstrated [Jagannathan et al. (2016b)], as well as the spatial control of interactions [Arunkumar et al. (2019)].

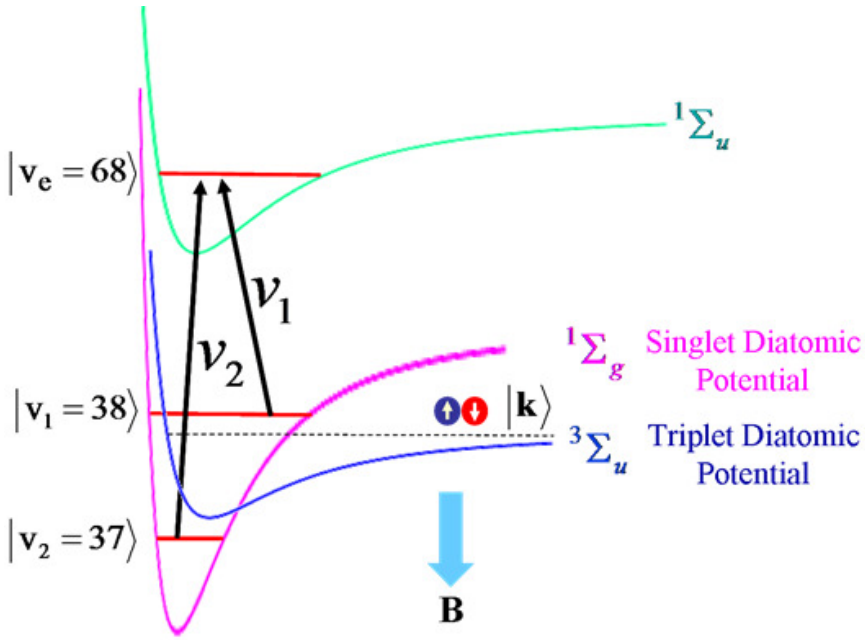

Figure 2.4: Depiction of two-field optical control of interactions in ^{6}Li. A magnetic field B tunes the s-wave scattering length a_s near a desired value via the magnetic Feshbach resonance, where $|g\rangle = |g_1\rangle = |v_1 = 38\rangle$ (the 38$^{\text{th}}$ vibrational state) is the bound state the incoming free atoms in the state $|\mathbf{k}\rangle$ are tuned into resonance with. A laser of frequency ν_1 drives transitions between $|g_1\rangle$ an excited molecular state $|e\rangle = |v_e = 68\rangle$, light-shifting the energy of the state $|g_1\rangle$. This changes a_s, but introduces loss via spontaneous emission from $|e\rangle$. A second laser at frequency ν_2 drives transitions between $|e\rangle$ and a second ground state $|g_2\rangle = |v_2 = 37\rangle$, reducing the probability to be in the state $|e\rangle$, as well as the light shift.

CHAPTER 3

INCORPORATING LOSS INTO THE ENERGY-SPACE SPIN-LATTICE MODEL

As described in § 2.2, the magnetic Feshbach resonance allows the s-wave scattering length to be continuously tuned from $a_s \to -\infty$ to $a_s \to +\infty$ by varying an applied magnetic field. It is possible to tune a_s to be small enough that the rate of energy-changing collisions is negligible during an experiment; a range of a_s which we refer to as the "weakly interacting regime" (note that this range depends on the density of the gas). The energy of *individual atoms* is, then, conserved in this regime. Forward s-wave scattering still occurs, which affects the two-atom spin state. When fermionic atoms in the weakly interacting regime are (1) trapped in a spin-dependent potential and (2) prepared in a coherent, 50-50 superposition of two spin states, the evolution of the system may be described with a spin-lattice model, with energy states replacing physical sites in a crystal.

The site-to-site couplings in the lattice may be tailored by exploiting the spatio-temporal resolution of a_s enabled by the optical control method described in § 2.3. While the two-beam method dramatically reduces the optically induced loss, finite loss remains, affecting the evolution of the system. In order to apply optical control to this system, we must understand this loss. While loss due to two body inelastic collisions was discussed in § 2.1.2, it is not directly applicable to this system, as atoms are in a continuum of evolving spin states and the cross section is dependent on the two-atom spin state.

This chapter is devoted to the theory of the energy-space spin-lattice, with and without loss. We first discuss the nature of the interactions between two fermionic atoms in the

weakly interacting regime with a spin-independent potential. Then we investigate the effect of spin-dependent potentials on a single atom. These two phenomena allow us to then obtain the evolution equations for the energy-space spin lattice. Next we describe our model for optically-induced loss in this system. Finally, we show how to predict the evolution of the spin-lattice when loss is present.

3.1 Two-Body Fermionic Interactions in the Weakly Interacting Regime

Consider two trapped, non-interacting fermionic atoms. Let the Hamiltonian describing the single-atom kinetic energy and interaction with the trap be H_T^j for atom j. We introduce a constant magnetic field **B** which distinguishes the spin states $|\uparrow\rangle$ and $|\downarrow\rangle$ and defines the quantization axis $\hat{\mathbf{z}}$. We write the Zeeman interaction as

$$H_B^j = -\hbar\omega_{HF}\hat{s}_{j_z} \tag{3.1}$$

where $\hat{s}_{j_z}$ is the z-component of the *dimensionless* spin operator on particle j (i.e., without the factor of $\hbar$). The hyperfine transition frequency between states $|\uparrow\rangle$ and $|\downarrow\rangle$, ω_{HF}, is magnetic-field dependent. The fractional change in ω_{HF} is negligible compared to the fractional change in the scattering length as the magnetic field is tuned in the weakly interacting regime, so we will neglect changes in ω_{HF} as a_s is varied. Since the total Hamiltonian $H_T^j + H_B^j$ is the sum of terms which operate separately on the total spin and energy states, the total two-atom state $|\psi_1\psi_2\rangle$ may be written as the product of a spin state $|s_1\, s_2\rangle$ and a motional state $|\phi_1\rangle_1 |\phi_2\rangle_2$

$$|\psi_1\psi_2\rangle = |\phi_1\rangle_1 |\phi_2\rangle_2 |s_1\, s_2\rangle \tag{3.2}$$

where

$$H_T^j |\phi_j\rangle_j = i\hbar\frac{\partial}{\partial t}|\phi_j\rangle_j \tag{3.3}$$

and we have allowed the spin states to be entangled, but assumed that the motional states are factorizable. Each atom, then, precesses in the magnetic field as they occupy the steady-state solutions to H_T^j.

Now, let the two ferimions interact via s-wave scattering, approximated with the psue-

dopotential Eq. 2.23, where the reduced mass $\mu = m/2$

$$H_{int}^{12} = \frac{8\pi a_s \hbar^2}{m} \delta(\mathbf{r}_2 - \mathbf{r}_1) \hat{P}_s^{12}. \tag{3.4}$$

Here, $\mathbf{r}_j$ is the spatial coordinate corresponding to atom j and $\hat{P}_s^{12}$ projects the incoming total two-atom spin state into the anti-symmetric, or "singlet," state. This spin-dependence of the interaction is due to fermionic nature of atoms— for s-wave scattering, the scattered two-atom spatial state is by definition spatially symmetric and therefore also symmetric upon exchange of the two atoms. This means that only the *anti-symmetric* projection of the spin state will scatter, so that the total two-atom wavefuntion is anti-symmetric upon particle exchange. The Hamiltonian for a pair of atoms now takes the form

$$H = H_T^1 + H_T^2 + H_B^1 + H_B^2 + H_{int}^{12} \tag{3.5}$$

where H_T^j is describes the interaction between atom j and the trap and H_B^j describes the interaction between the spin of atom j and the applied magnetic field. Treating H_{int}^{12} as a perturbation, we can continue to work in the same basis $|\phi_1\rangle_1 |\phi_2\rangle_2$.

We consider a_s to be small enough that we are in the"weakly interacting regime," for which the rate of energy-changing collisions is negligible on the timescale of the experiment. H_{int}^{12}, then, does not couple together different modes of the trap. It does, however, have an effect on the spin state(s). As will be discussed in § 3.3, it is possible for the rate at which the spins are affected to outweigh the collision rate: they differ, in part, due to the relative velocity dependence in the collision rate. Since H_{int}^{12} has no effect on the time dependence of $|\phi_1\rangle_1 |\phi_2\rangle_2$, with Eq. 3.3 we may write

$$(H_B^1 + H_B^2 + H_{int}^{12}) |\psi_1\, \psi_2\rangle = |\phi_1\rangle_1 |\phi_2\rangle_2\, i\hbar \frac{\partial}{\partial t} |s_1\, s_2\rangle\,. \tag{3.6}$$

This means that we may describe the system with a pure spin Hamiltonian H_s such that

$$H_s |s_1\, s_2\rangle = i \frac{\partial}{\partial t} |s_1\, s_2\rangle \tag{3.7}$$

(note that H_s is expressed in units of $\hbar$) where

$$H_s \equiv (1/\hbar) \langle \phi_2|_2 \langle \phi_1|_1 (H_B^1 + H_B^2 + H_{int}^{12}) |\phi_1\rangle_1 |\phi_2\rangle_2\,. \tag{3.8}$$

The Zeeman terms act only on the spin state, so, with Eqs. 3.1 and 3.4, we have

$$H_s = -\omega_{HF}\hat{s}_{1z} - \omega_{HF}\hat{s}_{2z} + \frac{8\pi a_s \hbar}{m}\hat{P}_s^{12}\langle\phi_2|_2\langle\phi_1|_1\,\delta(\mathbf{r}_2-\mathbf{r}_1)|\phi_1\rangle_1|\phi_2\rangle_2\,. \tag{3.9}$$

Projecting the motional states $|\phi_1\rangle_1$ and $|\phi_2\rangle_2$ onto configuration space and writing out $\hat{P}_s^{12}$ in terms of the single-atom spin vector operators $\hat{\mathbf{s}}_j$

$$\hat{P}_s^{12} = \frac{1}{4} - \hat{\mathbf{s}}_1\cdot\hat{\mathbf{s}}_2 \tag{3.10}$$

we obtain

$$H_s = -\omega_{HF}\hat{s}_{1z} - \omega_{HF}\hat{s}_{2z} + g\left[\frac{1}{4} - \hat{\mathbf{s}}_1\cdot\hat{\mathbf{s}}_2\right] \tag{3.11}$$

where we have defined g as

$$g \equiv \frac{8\pi a_s\hbar}{m}\int d^3\mathbf{r}\,|\phi_1(\mathbf{r})|^2|\phi_2(\mathbf{r})|^2 \tag{3.12}$$

where $\phi_j(\mathbf{r}) = \langle\mathbf{r}|\phi_j\rangle$.

Eq. 3.11 is the building block of the Ising Model, describing spins fixed at different sites in a crystal lattice and mutually affect each other's spin states. Here, instead of sites in a crystal, the atoms are fixed in their states $|\phi_1\rangle$ and $|\phi_2\rangle$. Working in the $|S\,M_s\rangle$ basis, it is simple to show that $[H,(\hat{\mathbf{s}}_1+\hat{\mathbf{s}}_2)^2] = \mathbf{0}$, so the spin dynamics will conserve the total spin quantum numbers s and m_s (i.e., states $|S\,M_s\rangle$ and $|S'\,M_{s'}\rangle$ are not coupled for $S\neq S'$, $M_s \neq M_{s'}$).

To further understand the spin dynamics, we work in the Heisenberg picture and compute the equations of motion for the spin operators

$$\dot{\hat{\mathbf{s}}}_j = i[H_s, \hat{\mathbf{s}}_j] \tag{3.13}$$

which results in

$$\dot{\hat{\mathbf{s}}}_1 = -\omega_{HF}\,\hat{\mathbf{z}}\times\hat{\mathbf{s}}_1 + g\,\hat{\mathbf{s}}_2\times\hat{\mathbf{s}}_1. \tag{3.14}$$

As expected, $\frac{d}{dt}|(\hat{\mathbf{s}}_1+\hat{\mathbf{s}}_2)| = 0$ Defining the (dimensionless) classical vector $\mathbf{S}_j \equiv \langle\dot{\hat{\mathbf{s}}}_j\rangle$, we find that, if we neglect entangled states so that $|s_1\,s_2\rangle = |s_1\rangle\,|s_2\rangle$,

$$\dot{\mathbf{S}}_1 = -\omega_{HF}\,\hat{\mathbf{z}}\times\mathbf{S}_1 + g\,\mathbf{S}_2\times\mathbf{S}_1 \tag{3.15}$$

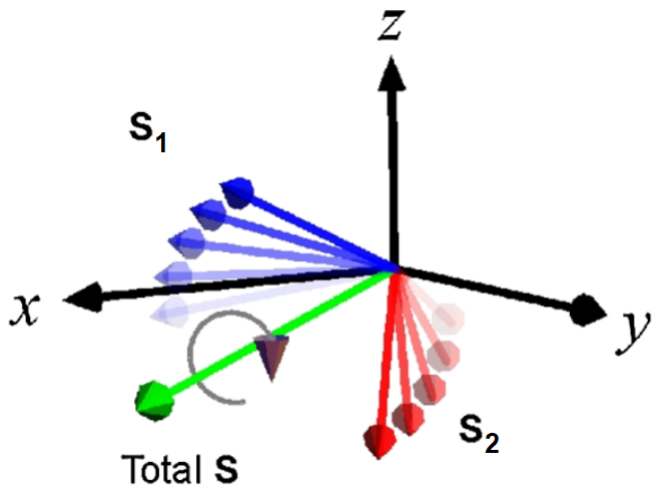

Figure 3.1: Depiction of the effect of s-wave interactions in the weakly interacting regime, in the classical limit for which each atom is assigned a classical spin vector. The interaction rotates each spin vector about the total spin vector. This figure was taken from [Du et al. (2008)].

and similarly for $\dot{\mathbf{S}}_2$. We see that, in this classical picture, two-body interactions simply rotate each individual spin vector about the total spin vector, as is depicted in Fig. 3.1.

While we have predicted this spin rotation effect to exist, we have no way of observing it in a gas of fermionic atoms when the spin state of the gas is incoherent. Nor would any effects appear if all atoms were in either the $|\uparrow\rangle$ state or the $|\downarrow\rangle$ state. We would require *groups* of atoms to have a similar spin states, with different groups at differing orientations. If each group had a distinctive spatial state $\phi(\mathbf{r})$, the effect of the spin rotation would be that the different spin states would be correlated with different spatial distributions. But how could the spin states of such groups of atoms be coherently prepared?

3.2 Effect of Spin-Dependent Potentials

Taking a detour from the effect of interactions between atoms, we consider single-atom motion in a trap which is spin-dependent. We again place the atoms in a magnetic field $\mathbf{B}$ which distinguishes the states $|\uparrow\rangle$ and $|\downarrow\rangle$. With the Zeeman interaction Eq. 3.1, the potential takes the form

$$V(\mathbf{r}) = V_{\uparrow}(\mathbf{r})|\uparrow\rangle\langle\uparrow| + V_{\downarrow}(\mathbf{r})|\downarrow\rangle\langle\downarrow| + H_B \tag{3.16}$$

we define $V_0(\mathbf{r})$ and $\Delta V(\mathbf{r})$ so that

$$V(\mathbf{r}) = V_0(\mathbf{r}) + \frac{1}{2}\Delta V(\mathbf{r})|\uparrow\rangle\langle\uparrow| - \frac{1}{2}\Delta V(\mathbf{r})|\downarrow\rangle\langle\downarrow| + H_B. \tag{3.17}$$

All of the spin dependence is then proportional to $\hat{s}_z$

$$V(\mathbf{r}) = V_0(\mathbf{r}) + \left(\Delta V(\mathbf{r}) - \hbar\omega_{HF}\right)\hat{s}_z. \tag{3.18}$$

The term, $\Delta H \equiv \Delta V(\mathbf{r})\hat{s}_z$, couples the motion to the spin. We can define an unperturbed Hamiltonion H_0 with an associated potential $V_0(\mathbf{r})$, which has solutions

$$H_0|E\rangle = E|E\rangle. \tag{3.19}$$

and is perturbed by ΔH.

With the spin-motion coupling perturbation, spin and energy become correlated— we cannot write single-atom state as $|\phi\rangle|s\rangle$. The state instead takes the form

$$|\psi\rangle = \sum_{E_\uparrow} c_\uparrow(E_\uparrow)|E_\uparrow\rangle|\uparrow\rangle + \sum_{E_\downarrow} c_\downarrow(E_\downarrow)|E_\downarrow\rangle|\downarrow\rangle. \tag{3.20}$$

with the Hamiltonian

$$H = \sum_{E_\uparrow} E_\uparrow|E_\uparrow\rangle|\uparrow\rangle\langle\uparrow|\langle E_\uparrow| + \sum_{E_\downarrow} E_\downarrow|E_\downarrow\rangle|\downarrow\rangle\langle\downarrow|\langle E_\downarrow| \tag{3.21}$$

Treating ΔH as a perturbation, first order perturbation theory results in

$$E_\uparrow = E - \frac{1}{2}\hbar\omega_{HF} + \frac{1}{2}\hbar\Omega_B(E) \tag{3.22}$$

$$E_\downarrow = E + \frac{1}{2}\hbar\omega_{HF} - \frac{1}{2}\hbar\Omega_B(E) \tag{3.23}$$

where $\Omega_B(E) \equiv (2/\hbar)\langle\uparrow|\langle E|\Delta H|E\rangle|\uparrow\rangle$. Eq. 3.21 becomes

$$H = \sum_E E\,\hat{I}(E) + \hbar\left[\Omega_B(E) - \omega_{HF}\right]\hat{\mathscr{S}}_z(E) \tag{3.24}$$

where we have defined $\hat{\mathscr{S}}_z(E) \equiv \frac{1}{2}|E_\uparrow\rangle|\uparrow\rangle\langle\uparrow|\langle E_\uparrow| - \frac{1}{2}|E_\downarrow\rangle|\downarrow\rangle\langle\downarrow|\langle E_\downarrow|$ and $I(E) \equiv |E_\uparrow\rangle|\uparrow\rangle\langle\uparrow|\langle E_\uparrow| + |E_\downarrow\rangle|\downarrow\rangle\langle\downarrow|\langle E_\downarrow|$. The spin-dependent perturbed states $|E_\uparrow\rangle$ and $|E_\downarrow\rangle$ may also be approximated

with first-order perturbation theory. If, however, we work in the approximation that $|E_\uparrow\rangle \approx |E_\downarrow\rangle \approx |E\rangle$,

$$H = \sum_E E\,|E\rangle\langle E| + \hbar\Big[\Omega_B(E) - \omega_{HF}\Big]\hat{s}_z(E) \tag{3.25}$$

where we have defined $\hat{s}_z(E) \equiv |E\rangle\langle E|\,\hat{s}_z$.

The dynamics described by Eq. 3.25 can be readily understood: the precession about the magnetic field, which occurs at a rate ω_{HF} in a spin-independent trap, now occurs at the *energy-dependent* rate $\Omega_B(E) - \omega_{HF}$. This is seen in the Heisenberg equations of motion Eq. 3.13 for $\hat{\mathbf{s}}(E)$, which leads to

$$\dot{\mathbf{S}}(E) = \Big[\boldsymbol{\Omega_B}(E) - \omega_{HF}\,\hat{\mathbf{z}}\Big] \times \mathbf{S}(E) \tag{3.26}$$

where we have defined the classical spin vector $\mathbf{S}(E) = \langle\hat{\mathbf{s}}(E)\rangle$. Working in a frame rotating about $-\hat{\mathbf{z}}$ (counter to about the dominant magnetic field direction) at ω_{HF},

$$\dot{\mathbf{S}}(E) = \boldsymbol{\Omega_B}(E) \times \mathbf{S}(E) \tag{3.27}$$

We note that working in this frame is equivalent to leaving out the H_B term in the Hamiltonian.

Eq. 3.27 shows that, if vectors begin aligned together orthogonal to the magnetic field, they will spread out in the transverse plane according to their energy. To realize this in an ultracold gas, one may apply a so-called "$\pi/2$ pulse" to a gas of atoms polarized in either the $|\uparrow\rangle$ or $|\downarrow\rangle$ state. The pulse consists of electromagnetic radiation at a frequency ω_{HF} (typically in the radio-frequency range of the spectrum) for a time such that the atoms are placed in an equal superposition of $|\uparrow\rangle$ and $|\downarrow\rangle$ (which corresponds to a $\pi/2$ rotation on the Bloch sphere). In the classical picture, this corresponds to a spin vector pointing in the plane transverse to the magnetic field. As the $\mathbf{S}(E)$ vectors spread out, we obtain groups of atoms with different spin orientations, each with a distinctive spatial profile.

3.2.1 Application to a Harmonic Trap

We apply the above analysis to one dimension of a spin-dependent trapping potential with a gas of many atoms in it. We work in the rotating frame which, as mentioned above, is equivalent to leaving out the H_B term. Then,

$$V_{1D}(x) = \frac{1}{2} m\omega_{x\uparrow}^2 x^2 |\uparrow\rangle\langle\uparrow| + \frac{1}{2} m\omega_{x\downarrow}^2 x^2 |\downarrow\rangle\langle\downarrow| \tag{3.28}$$

is the potential associated with motion in the x direction. Defining $\bar{\omega}_x \equiv \frac{1}{2}(\omega_{x\uparrow} + \omega_{x\downarrow})$ and $\delta\omega_x \equiv \omega_{x\uparrow} - \omega_{x\downarrow}$, we can re-write Eq. 3.28 as we did in Eq 3.17,

$$V_{1D}(x) = \frac{1}{2} m\bar{\omega}_x^2 x^2 + m\bar{\omega}_x \delta\omega_x x^2 \hat{s}_z. \tag{3.29}$$

We assume that $\bar{\omega}_x >> \delta\omega_x$ and treat the second term like a perturbation $\Delta H = m\bar{\omega}_x \delta\omega_x x^2 \hat{s}_z$, resulting in solutions $|n_x\rangle$ to the harmonic oscillator potential

$$(\mathscr{T}_x + \frac{1}{2} m\bar{\omega}_x^2 x^2)|n_x\rangle = E_{n_x}|n_x\rangle \tag{3.30}$$

where $\mathscr{T}_x$ is the kinetic energy operator for motion in the x direction.

Now, working with a gas of many ($10^4 - 10^5$) atoms at the ultracold temperatures described in § 5.1, atoms will occupy the $|n_x\rangle$ states up to $n_x \approx 650$. Working in the large-n_x limit, the first-order perturbed states are

$$|n_x,\uparrow\rangle \approx |n_x\rangle|\uparrow\rangle + \epsilon(|n_x+2\rangle - |n_x-2\rangle)|\uparrow\rangle, \tag{3.31}$$

$$|n_x,\downarrow\rangle \approx |n_x\rangle|\downarrow\rangle - \epsilon(|n_x+2\rangle - |n_x-2\rangle)|\downarrow\rangle. \tag{3.32}$$

This means that $\langle n_x,\uparrow|n_x,\uparrow\rangle = \langle n_x,\downarrow|n_x,\downarrow\rangle \approx \langle n_x,\downarrow|n_x,\uparrow\rangle \approx \langle n_x|n_x\rangle$. As these are the values that appear in the calculations, we are justified in working in the approximation that

$$|n_x, s\rangle \approx |n_x\rangle|s(n_x)\rangle \tag{3.33}$$

where s refers to the spin state. Note that spin and energy are still correlated.

From Eqs. 3.22 and 3.23, the perturbed energies are, to first order, are found with

$$\hbar\Omega_B(E) = \frac{\delta\omega_x}{\bar{\omega}_x} E \tag{3.34}$$

since $\langle n_x|x^2|n_x\rangle = E/(m\bar{\omega}_x^2)$ where $E = E_{n_x} = (n_x + \frac{1}{2})\hbar\bar{\omega}_x$. The precession rate is then linear in the energy associated with motion in the x direction.

3.3 The Weakly Interacting Gas as an Energy-Space Spin-Lattice

We now investigate the dynamics of a gas of fermionic atoms in a spin-dependent trap undergoing s-wave scattering in the weakly interacting regime. For our cigar-shaped optical trap, the atoms are taken to be in a cylindrically symmetric 3-D harmonic trap, with a radial trap frequency ω_ρ that is much larger than the axial trap frequency $\bar{\omega}_x$. The trapping force in the axial x-direction is spin-dependent. In our experiments, this is due to the curvature of the applied bias magnetic field $\partial_x^2 B_z$ and the difference in the magnetic moments for the two hyperfine states, which produces an axial trapping force comparable to the optical force in this direction. The dominant magnetic field direction $\hat{\mathbf{z}}$ defines the quantization axis for the spins. Starting from a $\hat{\mathbf{z}}$-polarized sample, the total spin state is coherently prepared in the XY plane by a $\pi/2$ pulse in the in order to separate the vectors with the energy-dependent precession rate (Eq. 3.27). Working in the rotating frame, we neglect H_B and the single-particle potential is

$$V_{sp}(\mathbf{r}) = \frac{1}{2}m\omega_\rho^2 y^2 + \frac{1}{2}m\omega_\rho^2 z^2 + \frac{1}{2}m\omega_{x\uparrow}^2 x^2 |\uparrow\rangle\langle\uparrow| + \frac{1}{2}m\omega_{x\downarrow}^2 x^2 |\downarrow\rangle\langle\downarrow|. \tag{3.35}$$

For N interacting fermions, the Hamiltonian H may then be written as

$$H = \sum_{j=1}^{N} H_{sp}^j + \frac{1}{2}\sum_{j=1}^{N}\sum_{k=1}^{N} H_{int}^{jk} \tag{3.36}$$

where H_{int}^{jk} is defined as in Eq. 3.4 and the single-particle Hamiltonian H_{sp}^j, containing the kinetic energy and the trapping potential, may be written as

$$H_{sp}^j = H_y^j + H_z^j + H_{x\uparrow}^j + H_{x\downarrow}^j. \tag{3.37}$$

We write the many-body state as

$$|\Psi\rangle = |\Psi_y\rangle |\Psi_z\rangle \prod_{j=1}^{N} |\psi_{x_j}, s_j\rangle_j \tag{3.38}$$

where we have allowed the spins to be correlated with the motion in the x direction and have factorized the atom states in y direction

$$|\Psi_y\rangle \equiv \prod_{j=1}^{N} |\psi_{y_j}\rangle_j \tag{3.39}$$

and likewise for $|\Psi_z\rangle$.

As in § 3.1, we will assume that single-atom energies are conserved on the timescales of the experiment. That is, the interaction term

$$H_{int}^{jk} = \frac{8\pi a_s \hbar^2}{m} \delta(\mathbf{r}_k - \mathbf{r}_j) \hat{P}_s^{jk} \tag{3.40}$$

has no effect on the time dependence of the trap modes. To justify this, recall from § 2.1.4, the rate of collisions $\dot{N}_c$ may be written by performing a volume intergral over Eq. 2.36,

$$\dot{N}_c = 4\pi a_s^2 \langle v_{rel} \rangle \int d^3\mathbf{r}\, n(\mathbf{r})^2 \tag{3.41}$$

where we have taken the cross-section to be $4\pi a_s^2$, assuming $k_{rel} a_s = \mu v_{rel} a_s/\hbar \to 0$, which is appropriate for the temperatures and scattering lengths used in our experiments ($\langle k_{rel} a_s \rangle \approx 10^{-5}$, where the brackets denote the average over k_{rel}). Taking $n(\mathbf{r})$ to be constant, the total number of collisions after a time T is $\dot{N}_c T$. For the typical density used (see § 5), at $a_s = 5\,a_0$ the fraction of atoms that have undergone collisions $\dot{N}_c T/N$ after our maximum evolution time $T = 400$ ms is ≈ 0.004. For $a_s = 24\,a_0$, this fraction is ≈ 0.1.

Since H_{int}^{jk} does not affect $|\psi_{y_j}\rangle_j$, the time dependence of the modes are determined only by the general solution to the harmonic oscillator Hamiltonian H_y^j

$$H_y^j |\psi_{y_j}\rangle = i\hbar \frac{\partial}{\partial t} |\psi_{y_j}\rangle \tag{3.42}$$

and the same goes for $|\psi_{z_j}\rangle$. This means that we may write

$$H_{1D} \prod_{j=1}^{N} |\psi_{x_j}, s_j\rangle_j = i\hbar \frac{\partial}{\partial t} \prod_{j=1}^{N} |\psi_{x_j}, s_j\rangle_j \tag{3.43}$$

where

$$H_{1D} = \sum_{j=1}^{N} H_{sp,1D}^j + \frac{1}{2} \sum_{j=1}^{N} \sum_{k=1}^{N} H_{int,1D}^{jk} \tag{3.44}$$

with

$$H_{int,1D}^{jk} = \langle\Psi_y|\langle\Psi_z|H_{int}^{jk}|\Psi_y\rangle|\Psi_z\rangle \tag{3.45}$$

and

$$H_{sp,1D}^{j} = H_{x\uparrow}^{j} + H_{x\downarrow}^{j} \tag{3.46}$$

Now, following § 3.2, we may write Eq. 3.46 as $H_{sp,1D}^{j} = H_0^j + \Delta V(\mathbf{r})\hat{s}_z^j$ and obtain, from Eq. 3.25,

$$H_{sp,1D}^{j} = \sum_E \left(E + \Omega_B(E) s_z^j\right) |\phi_E\rangle_j \langle\phi_E|_j . \tag{3.47}$$

Here, $|\phi_E\rangle_j \equiv e^{-iEt/\hbar}|E\rangle_j$, where $H_0^j|E\rangle_j = E|E\rangle_j$, and $\Omega_B(E)$ is the energy-dependent precession rate from Eq. 3.34, $\Omega_B(E) = \frac{\delta\omega_x}{\bar{\omega}_x}E$. Since $\delta(\mathbf{r}_j - \mathbf{r}_k) = \delta(x_j - x_k)\delta(y_j - y_k)\delta(z_j - z_k)$,

$$H_{int,1D}^{jk} = \frac{8\pi a_s \hbar^2}{m} \bar{n}_\perp^{jk} \delta(x_j - x_k) P_s^{jk} \tag{3.48}$$

where

$$\bar{n}_\perp^{jk} \equiv \int dy\, |\psi_{y_k}(y)|^2 |\psi_{y_j}(y)|^2 \int dz\, |\psi_{z_k}(z)|^2 |\psi_{z_j}(z)|^2 \tag{3.49}$$

is the averaged probability density in the YZ plane ($\perp$ to x).

We work in the approximation that each particle is in a single axial trap mode ,

$$|\psi_{x_j}, s_j\rangle_j = |\phi_{E_j}\rangle_j |s_j\rangle_j = e^{-iE_j t/\hbar}|E_j\rangle_j |s_j\rangle_j , \tag{3.50}$$

where E_j is the axial energy of particle j. Groups of atoms can have identical axial energies, since the state is also defined by $|\psi_{y_j}\rangle$ and $|\psi_{z_j}\rangle$. From our assumption of energy conservation, $H_0^j|\phi_{E_j}\rangle_j = i\hbar\frac{\partial}{\partial t}|\phi_{E_j}\rangle_j$, and we are able to write a pure spin Hamiltonian H_s which acts on the total spin state, as we did in § 3.1. We have already assumed a product state, so

$$H_s \prod_{j=1}^{N} |s_j\rangle_j = i\frac{\partial}{\partial t} \prod_{j=1}^{N} |s_j\rangle_j \tag{3.51}$$

(note that we have again expressed H_s in units of $\hbar$) where

$$H_s \equiv \frac{1}{\hbar}\left(\prod_{j=1}^{N} \langle\phi_{E_j}|_j\right) H_{1D} \left(\prod_{j=1}^{N} |\phi_{E_j}\rangle_j\right). \tag{3.52}$$

This yields

$$H_s = \sum_{j=1}^{N} \Omega_B(E) s_{j_z} + \frac{1}{2} \sum_{j=1}^{N} \sum_{k=1}^{N} \frac{8\pi a_s \hbar}{m} \bar{n}_{\perp}^{jk} \int d\,x |\phi_{E_j}(x)|^2 |\phi_{E_k}(x)|^2 P_s^{jk}. \tag{3.53}$$

For each axial energy E, there are $N_E = NP(E)$ atoms for which $|\psi_{x_j}, s_j\rangle_j = |\phi_{E_j}\rangle_j |s_j\rangle_j$, where $P(E)$ is found with either the Thomas-Fermi or Maxwell-Boltzmann distributions.

The sum over particles may be grouped by particles with the same axial energy:

$$\sum_{j=1}^{N} = \sum_{\substack{\text{atoms } \mu \text{ with} \\ \text{axial energy E}}}^{N_E} + \sum_{\substack{\text{atoms } \nu \text{ with} \\ \text{axial energy E'}}}^{N_{E'}} \ldots \tag{3.54}$$

We work in the approximation that $\bar{n}_{\perp}^{jk} \approx \langle \bar{n}_{\perp}^{jk} \rangle_{jk} = \bar{n}_{\perp}$. It follows that the evolution of the spins from H_s is only determined by its axial energy E. Since each initial spin state is taken to be equal (reflecting the coherent preparation of the total spin state), it is appropriate to define the collective spin vector operators

$$\hat{\boldsymbol{s}}(E) \equiv \sum_{\substack{\text{atoms } \mu \text{ with} \\ \text{axial energy E}}}^{N_E} \hat{\boldsymbol{s}}_{\mu} \tag{3.55}$$

which operate on the collective spin vector states

$$|s(E)\rangle \equiv \prod_{\substack{\text{atoms } \mu \text{ with} \\ \text{axial energy E}}}^{N_E} |s_{\mu}\rangle_{\mu}. \tag{3.56}$$

Since each atom that has an axial energy E evolves identically from the same initial state,

$$\hat{s}_z(E)|s(E)\rangle = \frac{N_E}{2}|s(E)\rangle \tag{3.57}$$

(recall from 3.1 that $\hat{\mathbf{s}}_{\mu}$ is equal to the spin vector operator defined up to a factor of $\hbar$). When writing the double sum in Eq. 3.53 in terms of groups of atoms with the same energy, we may neglect interactions between atoms j and k of the same energy, since $P_s^{jk}|s_j\rangle_j |s_k\rangle_k = 0$ (as $|s_j\rangle_j = |s_k\rangle_k$). We then have

$$H_s = \sum_{E} \Omega_B(E)\hat{s}_z(E) + \frac{1}{2}\sum_{E}\sum_{E'} g(E,E')\left[\frac{1}{4}N_E N_{E'} - \hat{\mathbf{s}}(E)\cdot\hat{\mathbf{s}}(E')\right] \tag{3.58}$$

where

$$g(E,E') = \frac{8\pi a_s \hbar}{m} \bar{n}_\perp \int dx\, |\phi_E(x)|^2 |\phi_{E'}(x)|^2. \tag{3.59}$$

Eq. 3.58 is effectively equivalent to the Ising model describing a spin-lattice, with the axial energy states of the trapping potential replacing the physical sites in a crystal. From Eqs. 3.59 and Eq. 3.41, we may calculate the ratio of the collision rate and the spin rotation rate that was discussed in § 3.1. We see that

$$\frac{\dot{N}_c/N}{g(E,E')} \propto \langle v_{rel} a_s \rangle / (\hbar/\mu) = \langle k_{rel} a_s \rangle \tag{3.60}$$

(where the brackets represent the average over the relative velocities v_{rel} and μ is the average mass), which is made small enough in the weakly interacting regime at low temperatures that the interactions can affect the spins without resulting in energy-changing collisions. As mentioned above, for the temperatures and scattering lengths used in our experiments, $\langle k_{rel} a_s \rangle \approx 10^{-5}$.

Eq. 3.59 gives the site-to-site couplings between atoms of energy E and atoms of energy E'. As written, it is fixed for a given potential. To tailor $g(E,E')$ in a given trap, one could make a_s spatially-dependent— then, it would appear in the argument of the integral, and change the value in an (E,E')-dependent way. The optical control method allows $a_s = a_s(x)$. If, for instance, interactions only occurred for atoms on the edge of the trap, only the collective spin vectors with higher energy would couple to one another. Further, fast temporal control of $g(E,E')$ is made possible with optical control, as it allows $a_s \to a_s(t)$.

Computing the Heisenberg equations of motion with Eq. 3.58 as was done in § 3.1 and with the factorized collective spin states that we have assumed, we have

$$\dot{\mathbf{S}}(E) = \mathbf{\Omega_B}(E) \times \mathbf{S}(E) + \sum_E g(E,E') \mathbf{S}(E') \times \mathbf{S}(E) \tag{3.61}$$

where $\mathbf{S}(E) \equiv \langle \hat{\mathbf{s}}(E) \rangle$. In our experiments, $g(E,E')$ and $\Omega_B(E)$ are on the order of 1 Hz. From Eq. 3.57, we take

$$|\mathbf{S}(E)| = N_E/2. \tag{3.62}$$

We recall that we are working the rotating frame. As the total spin state of the gas is prepared orthogonal to the magnetic field,

$$\hat{\mathbf{S}}(E, t=0) = \hat{\mathbf{x}}' \tag{3.63}$$

where $\hat{\mathbf{x}}' \perp \hat{\mathbf{z}}$ is defined in the rotating frame.

To connect the evolution in energy space Eq. 3.61 to the observations of the spatial density, we recall our approximation that each particle is in a single axial trap mode (Eq. 3.50) and write

$$S_z(x) = \sum_E |\phi_E(x)|^2 S_z(E) \tag{3.64}$$

where $S_z(x) = \frac{1}{2}[n_\uparrow(x) - n_\downarrow(x)]$ ($n_{\uparrow,\downarrow}(x)$ is the 1-D density associated with atoms in the spin state $\uparrow, \downarrow$). This allows the observations made in Ref. [Pegahan et al. (2019)] to be reproduced.

In order to implement Eq. 3.61, we group energies together, working with ≈ 100 different energies as opposed to ≈ 650 different axial trap modes that are occupied. The overlap integral in Eq. 3.59 is evaluated using a WKB approximation. For a harmonic trap,

$$\int dx\, |\phi_E(x)|^2 |\phi_{E'}(x)|^2 = \frac{2}{\pi^2} \sqrt{\frac{m\bar{\omega}_x^2}{2|E-E'|}}\, \text{EllipticK}\left[-\frac{\min(E,E')}{|E-E'|}\right]. \tag{3.65}$$

In our calculation, the assumption that $\bar{n}_\perp^{jk} \approx \langle \bar{n}_\perp^{jk} \rangle_{jk} = \bar{n}_\perp$ means that we have assumed that the single-particle probability density takes the form $\mathscr{R}(\rho)|\phi_E(x)|^2$, where ρ is the transverse radial coordinate, $\mathscr{R}(\rho)$ is the transverse probability density, and $\int d\rho\, 2\pi\rho\, \mathscr{R}(\rho) = 1$. $\bar{n}_\perp$ is the average transverse probability density,

$$\bar{n}_\perp \equiv \int d\rho\, 2\pi\rho\, \mathscr{R}^2(\rho). \tag{3.66}$$

For lossless evolution, $\mathscr{R}(\rho)$ is time-independent. Assuming a zero-temperature Thomas-Fermi distribution,

$$\mathscr{R}(\rho) = \frac{3}{\pi\sigma_\rho^2}\left(1 - \frac{\rho^2}{\sigma_\rho^2}\right)^2 \tag{3.67}$$

we obtain $\bar{n}_\perp = 9/(5\pi\sigma_\rho^2)$. For the Maxwell-Boltzmann distribution,

$$\mathscr{R}(\rho) = \frac{1}{\pi\sigma_\rho^2}\, e^{-\rho^2/\sigma_\rho^2}, \tag{3.68}$$

we find $\bar{n}_\perp = 1/(\pi\sigma_\rho^2)$.

3.3.1 Understanding Spin-Lattice Dynamics

Eq 3.61 shows that each collective spin vector $\mathbf{S}(E,t)$ rotates about an effective magnetic field vector, comprising an applied magnetic field component along $\hat{\mathbf{z}}$ and a net mean field

component arising from forward s-wave scattering interactions with all other $\mathbf{S}(E', t)$. For small a_s, where the energy-dependent precession rate about the magnetic field dominates, the spin vectors fan out in the transverse plane, reducing the effect of the mean-field. This is reflected in a low magnitude of the total spin vector $S(t) = |\sum_E \mathbf{S}(E, t)|$, as shown in Fig. 3.2. For sufficiently large a_s, the mean-field becomes significant, suppressing the energy-dependent spreading of the collective spin vectors, which effectively orbit the mean-field. However, the effect of the mean field degrades as the spin vectors align, as there is no longer any rotation about the mean field axis. This again allows the spread in the Zeeman precession rates to separate the spin vectors, which allows the rotation about the mean field to dominate again, leading to an oscillation of the magnitude of the total spin vector, as shown in Fig. 3.2. We see that for larger a_s, where the mean-field dominates and most spin vectors align, the amplitude of the oscillation is smallest, corresponding to a transition to a magnetized state [Smale et al. (2019b); Huang and Thomas (2023)]. This transition depends not only on a_s, but also the density and the spread in the energy-dependent precession rates $\Omega'\sigma_E$. The larger $\Omega'\sigma_E$ is, the stronger the couplings must be in order to transition into the magnetized state. The transition is more generally parameterized by the "interaction strength" $\zeta \equiv \bar{g}/(\Omega'\sigma_E\sqrt{2})$ (where $\bar{g}$ is the averaged value of $g(E, E')$), which is ≈ 1 at the transition point. Note that in our experiments, since a z-polarized sample is coherently excited by a $\pi/2$ RF pulse resulting in Eq. 3.63, which means that $S_z(t) \equiv \sum_E S_z(E, t) = 0$ and therefore $S(t) = \sqrt{S_\perp(t)^2 + S_z(t)^2} = S_\perp(t)$.

While the model captures the data while the spin states initially segregate in space, it does not agree with observations for longer times, as is observed in Ref. [Pegahan et al. (2019)]. The continuous oscillation described above is not observed— the oscillation is effectively damped. This will be discussed in § 6.3.

3.4 Modeling Two-Body Loss in the Lattice

Inelastic interactions are induced in the energy-space spin lattice by illuminating the coherently prepared clouds with an optical field. In this section, we describe our model for the loss in this system due to these interactions.

We begin by describing the interaction process (§ 2.2.1 and § 2.2.2) with the optical field: For the magnetic fields of interest, a collision between a pair of ^{6}Li atoms, one in each of the two lowest hyperfine spin states $|1\rangle$ and $|2\rangle$, occurs nominally in the triplet electronic potential (where "triplet" refers to the two-electron spin state). For s-wave scattering, where

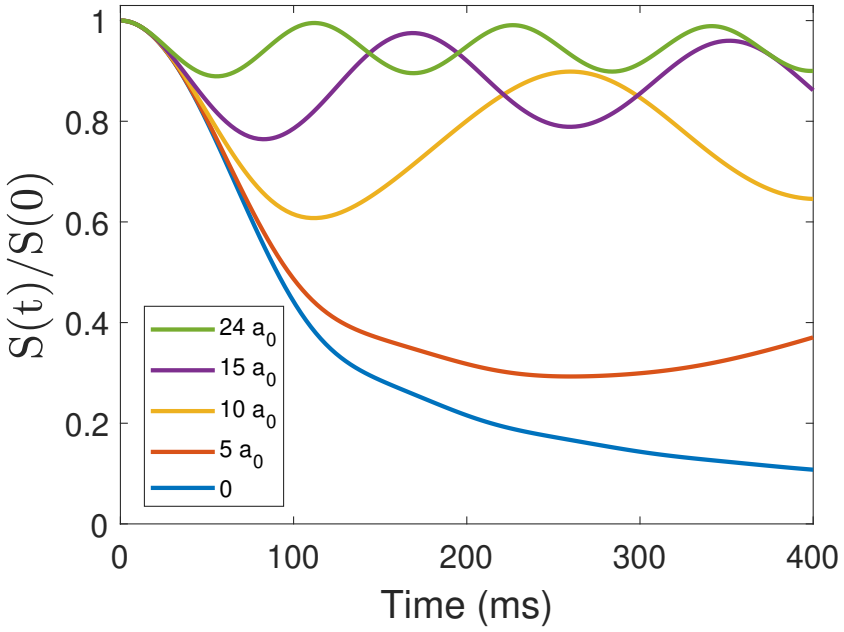

Figure 3.2: Predicted magnitude the total spin vector versus time for loss-free evolution with different s-wave scattering lengths. $N = 6.0 \times 10^4$ atoms and the zero-temperature Thomas-Fermi widths for the axial and radial directions are 330.0 μm and 12.0 μm, respectively, resulting in $\zeta \approx 1$ at $a_s = 5\,a_0$. Since $S_z(t) = 0$ when the spins are prepared orthogonal to the applied magnetic field, $S(t) = S_\perp(t)$, the length of the transverse (XY plane) projection of the total spin vector.

the relative motion state is symmetric in the interchange of the two atoms, the two-*atom* hyperfine state is the antisymmetric state,

$$|\Psi_a(1,2)\rangle = \frac{1}{\sqrt{2}}\left(|\uparrow_z\rangle_1\,|\downarrow_z\rangle_2 - |\downarrow_z\rangle_1\,|\uparrow_z\rangle_2\right) \simeq |S=1\,m_S=1\rangle\,|I=1\,m_I=-1\rangle\,. \tag{3.69}$$

At high magnetic fields, as used in the experiments, $|1,-1;1,1\rangle$ is the dominant triplet state in the interior basis, i.e., the total electronic spin state is $|S=1\,M_S=-1\rangle$, the total nuclear spin state is $I=1, M_I=1$. This triplet state has a large hyperfine coupling to the dominant singlet electronic state $|S=0\,M_S=0\rangle$ [Wu and Thomas (2012b)], denoted $|g\rangle$, which is in the 38^{th} vibrational state of the singlet ground molecular potential, producing a broad Feshbach resonance at 832.2 G [Zürn et al. (2013)]. The difference between the magnetic moments of the singlet and triplet states enables magnetic tuning of the s-wave scattering length near the resonance. The applied optical field drives transitions from $|g\rangle$ to the 64^{th} electronically-excited vibrational state in the electronic singlet molecular potential, denoted $|e\rangle$ [Wu and

Thomas (2012a); Jagannathan et al. (2016a)]. Spontaneous emission from $|e\rangle$ causes the interaction to be inelastic, and we assume that the emission results in loss of both atoms without transfer of atoms between energy states, so that the energy-space spin lattice model remains appropriate.

As was introduced in § 2.1.4, loss due to two-body inelastic collisions between a particle of species A and a particle of species B is generally modeled as

$$\dot{n}_A(\mathbf{r},t) = \dot{n}_B(\mathbf{r},t) = -K_2^{AB} n_A(\mathbf{r},t) n_B(\mathbf{r},t) \tag{3.70}$$

where $n_A(\mathbf{r},t)$ is the 3D density of species A and $n_B(\mathbf{r},t)$ is the 3D density of species B. It is assumed that only A and B interact, and that each inelastic collisions causes both atoms to be lost. Eq. 3.70 follows from the definition of the inelastic cross-section of the AB interaction σ_{inel}^{AB} where $K_2^{AB} \equiv \langle v_{rel} \sigma_{inel}^{AB} \rangle$ (the brackets denote the average over the relative speeds v_{rel}). This will be our basis for constructing our loss model.

To treat loss in the energy-space spin lattice, we consider the atoms at each axial energy site E to be a "species" in the context of Eq. 3.70. We associate a 3D density $n_E(\mathbf{r},t)$ to the group of atoms with energy E and a collective spin vector $\mathbf{S}(E,t)$, and sum the inelastic collision rates for atoms of energy with E with atoms of energies E' over all $E' \neq E$ to obtain

$$\dot{n}_E(\mathbf{r},t) = -\sum_{E'} K(E,E',t)\, n_{E'}(\mathbf{r},t)\, n_E(\mathbf{r},t). \tag{3.71}$$

Here the total density is $n(\mathbf{r},t) = \sum_E n_E(\mathbf{r},t)$ and $K(E,E',t)$ is the effective energy-dependent two-body loss rate coefficient.

We obtain $K(E,E',t)$ by computing the probability that the pair of atoms in energy groups E and E' are in the antisymmetric spin state $|\Psi_a(1,2)\rangle$. We assume that the spin of each atom of energy E is polarized along $\mathbf{S}(E,t)$, corresponding to the spin state $|\hat{\mathbf{S}}(E,t)\rangle$. In this case, atoms of energies E and E' are in states with definite spin polarizations, so that we can assume the incoming spin state for a colliding pair of atoms with energies E and E' is $|\hat{\mathbf{S}}(E,t)\rangle_1 |\hat{\mathbf{S}}(E',t)\rangle_2$. The probability amplitude to be in the singlet state is then found by the inner product of this state with $|\Psi_a(1,2)\rangle$, so that

$$K(E,E',t) = K_2^a \, |\langle \Psi_a(1,2)| \hat{\mathbf{S}}(E,t)\rangle_1 \, |\hat{\mathbf{S}}(E',t)\rangle_2|^2. \tag{3.72}$$

where K_2^a is the loss constant associated with the antisymmetric two-atom spin state, given in Eq. 3.69. Suppressing the time dependence, the energy-dependent spin states take the

form,

$$\begin{aligned} |\hat{\mathbf{S}}(E)\rangle_1 &= e^{-i\phi_E/2}\cos(\theta_E/2)\,|\uparrow_z\rangle_1 + e^{i\phi_E/2}\sin(\theta_E/2)\,|\downarrow_z\rangle_1 \\ |\hat{\mathbf{S}}(E')\rangle_2 &= e^{-i\phi'_E/2}\cos(\theta'_E/2)\,|\uparrow_z\rangle_2 + e^{i\phi'_E/2}\sin(\theta'_E/2)\,|\downarrow_z\rangle_2 . \end{aligned} \tag{3.73}$$

A straightforward calculation gives

$$|\,\langle\Psi_a(1,2)|\,\hat{\mathbf{S}}(E,t)\rangle_1\,|\hat{\mathbf{S}}(E',t)\rangle_2\,|^2 = \frac{1}{4}\left[1-\cos\theta_E\cos\theta_{E'}-\sin\theta_E\sin\theta_{E'}\cos(\phi_E-\phi_{E'})\right], \tag{3.74}$$

or, in terms of the unit vectors and restoring the time dependence,

$$K(E,E',t)\equiv\frac{K_2^a}{4}\left[1-\hat{\mathbf{S}}(E,t)\cdot\hat{\mathbf{S}}(E',t)\right]. \tag{3.75}$$

As expected, when the collective spin vectors for energy groups E and E' vectors are parallel, the corresponding unit vectors $\hat{\mathbf{S}}(E,t)$ and $\hat{\mathbf{S}}(E',t)$ are parallel and there is no loss. In contrast, maximum loss occurs when the unit vectors are anti-parallel, $K(E,E',t)\to K_2^a/2$. The unit vectors $\hat{\mathbf{S}}(E,t)$ are found from Eq. 3.61, with $S(E,t)=N_E(t)/2$, where the atom number $N_E(t)$ is self-consistently determined from Eqs. 3.71 and 3.75, as we now show.

We assume that the spin-energy correlated 3D densities $n_E(\mathbf{r},t)$ can be factored as

$$n_E(\mathbf{r},t)=n_E(x,\rho,t)=N_E(t)\mathscr{R}(\rho,t)|\phi_E(x)|^2, \tag{3.76}$$

where x is the axial coordinate and ρ the transverse coordinate. As observed in the experiments and shown in § 5.4, for nonzero K_2^a, the increase in the loss rate with increasing 3D density reshapes the spatial profile. For this reason, we assume that both the atom number $N_E(t)$ in each energy group and the transverse probability density $\mathscr{R}(\rho,t)$ are functions of time. Further, we assume that $\mathscr{R}(\rho,t)$ is independent of E, and take $\int d\rho\,2\pi\rho\,\mathscr{R}(\rho,t)=1$ for all t. Using Eq. 3.76, the spatial integral of the total density, $n(\mathbf{r},t)=\sum_E n_E(\mathbf{r},t)$ yields total atom number,

$$N(t)=\sum_E N_E(t). \tag{3.77}$$

Using Eq. 3.76 in Eq. 3.71 and integrating over x, we obtain

$$\frac{d}{dt}\left[N_E(t)\mathscr{R}(\rho,t)\right]=-\sum_{E'}\eta(E,E',t)\left[N_{E'}(t)\mathscr{R}(\rho,t)\right]\left[N_E(t)\mathscr{R}(\rho,t)\right], \tag{3.78}$$

where

$$\eta(E,E',t)\equiv K(E,E',t)\int dx\,|\phi_E(x)|^2|\phi_{E'}(x)|^2. \tag{3.79}$$

Integrating Eq. 3.78 over ρ and using Eq. 3.81, we find

$$\dot{N}_E(t)\int d\rho\,2\pi\rho\,\mathscr{R}(\rho,t)+N_E(t)\frac{d}{dt}\int d\rho\,2\pi\rho\,\mathscr{R}(\rho,t)=-\bar{n}_\perp(t)\sum_{E'}\eta(E,E',t)N_{E'}(t)N_E(t), \tag{3.80}$$

where $\bar{n}_\perp(t)$ is the time-dependent average transverse probability density

$$\bar{n}_\perp(t)\equiv\int d\rho\,2\pi\rho\,\mathscr{R}^2(\rho,t). \tag{3.81}$$

Since $\int d\rho\,2\pi\rho\,\mathscr{R}(\rho,t)=1$, Eq. 3.80 immediately yields

$$\dot{N}_E(t)=-\bar{n}_\perp(t)\sum_{E'}\eta(E,E',t)N_{E'}(t)N_E(t). \tag{3.82}$$

Next, we sum Eq. 3.78 over E and use Eq. 3.77 to obtain

$$\dot{N}(t)\mathscr{R}(\rho,t)+N(t)\dot{\mathscr{R}}(\rho,t)=-\mathscr{R}^2(\rho,t)\sum_E\sum_{E'}\eta(E,E',t)N_{E'}(t)N_E(t)=\dot{N}(t)\frac{\mathscr{R}^2(\rho,t)}{\bar{n}_\perp(t)}. \tag{3.83}$$

Here, the right-hand side has been simplified by using the sum of Eq. 3.82 over E and Eq. 3.77,

$$\dot{N}(t)=-\bar{n}_\perp(t)\sum_E\sum_{E'}\eta(E,E',t)N_{E'}(t)N_E(t). \tag{3.84}$$

Hence, the radial probability distribution obeys

$$\dot{\mathscr{R}}(\rho,t)=\frac{\dot{N}(t)}{N(t)}\left[\frac{\mathscr{R}^2(\rho,t)}{\bar{n}_\perp(t)}-\mathscr{R}(\rho,t)\right]. \tag{3.85}$$

Using Eq. 3.81, one readily verifies that the integral of Eq. 3.85 over ρ vanishes, so that the total transverse probability remains normalized to 1 for all t. Further, the right hand side is $\propto\dot{N}(t)[\mathscr{R}(\rho,t)-\bar{n}_\perp(t)]$, where $\dot{N}(t)<0$ when $K_2^a\neq 0$. Hence, near the center of the cloud, where $\mathscr{R}(\rho,t)>\bar{n}_\perp(t)$, the probability density decreases in time, while in the wings, where $\mathscr{R}(\rho,t)<\bar{n}_\perp(t)$, the probability density increases in time. The net effect of the loss is to increase the effective width of $\mathscr{R}(\rho,t)$, while preserving the normalization.

3.5 Evolution of the Lattice with Loss

To model the energy-space lattice with optically-induced loss, we employ Eqs. 3.82 and 3.85, together with Eq. 3.61. These equations determine the evolution of the density for each energy group, the transverse profile and therefore the total density and the total number in the presence of loss, which are compared with the measurements.

Including the E-dependent loss, the magnitudes of the collective spin vectors in Eq. 3.61, $S(E,t) = N_E(t)/2$, decrease with time. The evolution of $\mathbf{S}(E,t)$ includes both a rotation of the unit vectors and a time-dependent magnitude,

$$\dot{\mathbf{S}}(E,t) = S(E,t)\dot{\hat{\mathbf{S}}}(E,t) + \dot{S}(E,t)\hat{\mathbf{S}}(E,t). \tag{3.86}$$

The unit vectors $\hat{\mathbf{S}}(E,t)$ evolve according to Eq. 3.61, while the decay of the magnitudes $S(E,t)$ is determined by Eq. 3.82 with $N_E(t) = 2\,S(E,t)$ and Eqs. 3.79 and 3.75,

$$\dot{S}(E,t) = -\sum_{E'} \kappa(E,E',t)\left[S(E,t)S(E',t) - \mathbf{S}(E,t)\cdot\mathbf{S}(E',t)\right]. \tag{3.87}$$

Here, the effective loss rate $\kappa(E,E',t)$ is given by

$$\kappa(E,E',t) \equiv \frac{K_2^a}{2}\,\bar{n}_\perp(t)\int dx\,|\phi_E(x)|^2|\phi_{E'}(x)|^2. \tag{3.88}$$

We discuss the measurement of K_2^a for mixtures in § 5.3.

We rewrite the evolution of the transverse probability density, Eq. 3.85, as

$$\dot{\mathscr{R}}(\rho,t) = \frac{\dot{S}(t)}{S(t)}\left[\frac{\mathscr{R}^2(\rho,t)}{\bar{n}_\perp(t)} - \mathscr{R}(\rho,t)\right]. \tag{3.89}$$

Here we have defined $S(t) \equiv \sum_E S(E,t) = N(t)/2$. As the site-to-site couplings $g(E,E')$ of Eq. 3.59 are proportional to $\bar{n}_\perp$, the time-dependence of $\bar{n}_\perp$ for $K_2^a \neq 0$ results in $g(E,E') \to g(E,E',t)$; while the decay of $S(E,t)$ reduces the rotation rate of the unit vectors by reducing the magnitude of the mean field.

Including loss, the evolution of the energy-dependent collective spin vectors is determined by Eq. 3.86, using Eq. 3.61 to describe the rotation of the unit vectors and Eqs. 3.87, 3.89, and 3.81 to determine the decay of the magnitudes. The collective spin vectors are initialized according to Eqs. 3.62 and 3.63. The initial condition for the transverse probability density, $\mathscr{R}(\rho,0)$, is given by Eq. 3.67 for a Thomas-Fermi distribution and by

Eq. 3.68 for a Maxwell-Boltzmann distribution.

3.6 Method of Obtaining the Loss Constant K_2^a

For the loss model described above, we require the loss constant K_2^a associated with a pair of atoms in the antisymmetric two-atom spin state $|\Psi_a(1,2)\rangle$. To obtain K_2^a, we measure the loss in a 50-50 incoherent mixture of $|\uparrow_z\rangle$ and $|\downarrow_z\rangle$, for which the 50-50 ratio is maintained throughout the evolution, and extract the fraction of the loss constant associated with the state $|\Psi_a(1,2)\rangle$. Considering the mixture to be comprised of atoms in the $|\uparrow_z\rangle$ state and the $|\downarrow_z\rangle$ state, we define the 3D densities associated with each state $n_\uparrow(\mathbf{r},t)$ and $n_\downarrow(\mathbf{r},t)$ and apply Eq. 3.70 to obtain

$$\dot{n}_\uparrow(\mathbf{r},t)=\dot{n}_\downarrow(\mathbf{r},t)=-K_2^{\uparrow\downarrow}n_\uparrow(\mathbf{r},t)n_\downarrow(\mathbf{r},t). \tag{3.90}$$

Since the probability of this incoming two-atom spin state to be in the antisymmetric two-atom spin state is $|\langle\Psi_a(1,2)|\uparrow_z\rangle_1|\downarrow_z\rangle_2|^2=1/2$, we have

$$K_2^{\uparrow\downarrow}=K_2^a\times 1/2. \tag{3.91}$$

With $n_\uparrow(\mathbf{r},t)+n_\downarrow(\mathbf{r},t)=n(\mathbf{r},t)$ the total density and $n_\uparrow(\mathbf{r},t)=n_\downarrow(\mathbf{r},t)=n(\mathbf{r},t)/2$ for a 50-50 mixture, Eq. 3.90 yields

$$\dot{n}(\mathbf{r},t)=-\frac{1}{4}K_2^a\,n^2(\mathbf{r},t). \tag{3.92}$$

Eq. 3.92 may be solved analytically:

$$n(\mathbf{r},t)=\frac{n(\mathbf{r},0)}{1+\frac{1}{4}K_2^a n(\mathbf{r},0)\,t}. \tag{3.93}$$

Integrating Eq. 3.93 over all three spatial dimensions, the total atom number $N(t)$ is predicted as a function of time, given $n(\mathbf{r},0)$:

$$N(t)=\int dx\int 2\pi\rho\,d\rho\,\frac{n(\mathbf{r},0)}{1+\frac{1}{4}K_2^a n(\mathbf{r},0)\,t}. \tag{3.94}$$

To measure K_2^a, then, we fit measurements of the atom number $N(t)$ in the 50-50 mixture to Eq. 3.94. This is further described in § 5.3. In § 6.1, we show that K_2^a is independent of the relative speed near the zero crossing of the broad Feshbach resonance in ^{6}Li. However, as will also be discussed in § 5, we must *halve* the measured K_2^a before inserting it into Eq. 3.74 in order to reach agreement with the loss measurements in the energy-space spin-lattice.

CHAPTER 4

EXPERIMENTAL METHODS

As described in the last chapter, the conditions required to create the energy-space spin-lattice are (1) an ensemble of fermions interacting via pure s-wave scattering, (2) a s-wave scattering length a_s tuned to be in the "weakly interacting regime" (and, if desired, able to access the full range of the phase transition, without introducing energy-changing collisions), (3) a coherently prepared total spin state orthogonal to the magnetic field axis, and (4) a trapping potential that exhibits some spin-dependence. To optically induce inelastic collisions in the lattice, we must illuminate the fermions with an optical beam beam near resonance with the $g \rightarrow e$ transition.

We achieve these conditions in an ultracold Fermi gas of neutral lithium-6 atoms, prepared in the weakly interacting regime in a coherent superposition of the two lowest-energy hyperfine states $|1\rangle$ and $|2\rangle$ (see § 2.2.2 and § A). The atoms are trapped in the focus of a single 10.6 μm CO_2 laser beam. The curvature from the applied magnetic field used to tune a_s provides a spin-dependence to the trapping potential along the direction of the beam (referred to from here on out as the *axial* direction), as depicted in Fig. 4.1. All but s-wave collisions are "frozen-out" at the ultracold temperatures. The ultracold temperatures also allow the spin rotation effect (introduced in the previous chapter) to dominate over the rate of energy-changing collisions, since $(\dot{N}_c/N)/g(E,E') \propto \langle v_{rel} \rangle$, where $\langle v_{rel} \rangle$ is the averaged relative velocity. The beam that induces inelastic collisions is frequency-locked on the transition between the ground molecular state g responsible for the (broad) magnetic Feshbach resonance (the 38$^{\text{th}}$ vibrational state) and an electronically-excited molecular state e (the 68$^{\text{th}}$ vibrational state) . The beam is large enough to provide a nominal uniform

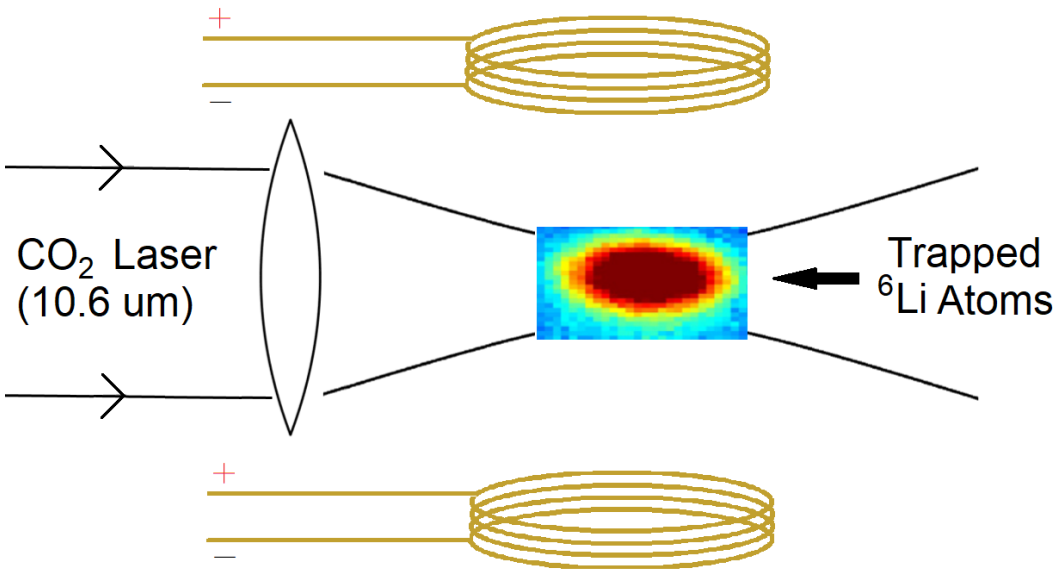

Figure 4.1: Depiction of our system: ultracold Lithium-6 atoms in a vacuum are trapped in the focus of a CO_2 laser with a 10.6 μm wavelength. Electromagnets are used to generate a magnetic field up to 1200 G in order to control the s-wave scattering length. The curvature of the magnetic field results in a spin-dependent trapping potential.

illumination.

In this chapter, we describe how the ultracold gas is created and observed; then, once created, how the loss-inducing beam is stabilized on the $g \rightarrow e$ transition.

4.1 Creation and Observation of an Ultracold Gas

Atoms in the gas state may be isolated in suspended, containerless traps via electromagnetic forces. Given sufficient methods of energy removal from the atoms, the thermal isolation of these traps (when placed in a vacuum) allows for the cooling of atoms to "ultracold" temperatures, which can be low enough to be on the order of trillioniths of a Kelvin [Deppner et al. (2021)]. Atomic speeds at these temperatures can range from millimeters per second to meters per second. As these low temperatures are approached, the deBroglie wavelength increases towards the interparticle distance and quantum-mechanical phenomena may be observed.

When manipulating electrically-neutral atoms with electromagnetic forces, we may exploit the *inherent* magnetic dipole moment $\boldsymbol{\mu}$ of atoms to exert a force $\mathbf{F_B} = (\boldsymbol{\mu}\cdot\boldsymbol{\nabla})\mathbf{B}$ using gradients in applied magnetic field $\mathbf{B}$; or we may *induce* an electric dipole moment $\mathbf{d}$ with an applied electric field $\mathbf{E}$ to exert a force $\mathbf{F_E} = (\mathbf{d}\cdot\boldsymbol{\nabla})\mathbf{E} = \alpha(\mathbf{E}\cdot\boldsymbol{\nabla})\mathbf{E}$ using gradients in $\mathbf{E}$ (assuming a linear response $\mathbf{d} = \alpha\mathbf{E}$). To create a trap, we would like the atoms to be forced back to one point, wherever they move. Since a maximum in $|\mathbf{B}|$ is inconsistent with Maxwell's Equations, $\mathbf{F_B}$ can only result in a trapping force if $\boldsymbol{\mu}$ is counter to $\mathbf{B}$, in which case a trap can be formed about a minimum in $|\mathbf{B}|$ (though, the trap cannot be three-dimensional). A maximum in $|\mathbf{E}|$ is similarly inconsistent with Maxwell's Equations when $\mathbf{E}$ is time-independent and outside of a charge distribution. $\mathbf{F_E}$ will, however, always be attracted towards a maximum in $|\mathbf{E}|$ (taking $\alpha > 0$); which means that $\mathbf{E}$ must be time-dependent to create a trapping force. In this case, three dimensional trapping can be realized.

We consider $\mathbf{F_E}$ for the case that $\mathbf{E}$ is formed by a monochromatic electromagnetic wave,

$$\mathbf{E}(\mathbf{r}) = \text{real}\left[\boldsymbol{\mathscr{E}}(\mathbf{r})e^{i(\mathbf{k}\cdot\mathbf{r}-\omega t)}\right]. \tag{4.1}$$

The field induces a time-dependent electric dipole moment. The charges are then in motion, which results in the full Lorentz force as the charges interact with magnetic field associated with the plane wave. It can be shown that the time-averaged total force over the the time

$T >> 2\pi/\omega$ —electric *and* magnetic— is

$$\left\langle \mathscr{F}_j \right\rangle_T \approx \left\langle d_k \partial_j E_k \right) \right\rangle_T. \tag{4.2}$$

Then, α becomes frequency-dependent and may not be in-phase with **E**. Working in a complex representation,

$$\mathbf{d} = \text{real}\left[\alpha(\omega) \mathscr{E}(\mathbf{R}) e^{i(\mathbf{k}\cdot\mathbf{R}-\omega t)} \right]. \tag{4.3}$$

where R is the atom's center-of-mass and $\alpha(\omega)$, which may be modeled classically or quantum-mechanically, peaks at a resonance frequency of the atom. The real part of $\alpha(\omega)$ corresponds to the in-phase component of the dipole, and the imaginary part corresponds to the part that is 90° out of phase. There are, then, two contributions to the total force. One is from the spatial derivative of the beam profile $\mathscr{E}(\mathbf{r})$, and one from the spatial derivative of the phase of the field— the former is the induced dipole force $\mathscr{F}_{dipole}$, and the latter is the radiation pressure force $\mathscr{F}_{pressure}$.

$$\left\langle \mathscr{F} \right\rangle_T \approx \mathscr{F}_{dipole} + \mathscr{F}_{pressure} \tag{4.4}$$

$\mathscr{F}_{dipole}$ is *conservative* and proportional to the real part of $\alpha(\omega)$,

$$\mathscr{F}_{dipole} = \frac{1}{4} \text{real}\big[\alpha(\omega)\big] \nabla |\mathscr{E}|^2. \tag{4.5}$$

and $\mathscr{F}_{pressure}$ is *non-conservative* and proportional to the imaginary part of $\alpha(\omega)$

$$\mathscr{F}_{pressure} = \frac{1}{2} \text{imag}\big[\alpha(\omega)\big] |\mathscr{E}|^2 \mathbf{k} \tag{4.6}$$

So far we have considered the electromagnetic field classically. $\mathscr{F}_{pressure}$ can also be understood in a simple picture of the absorption and emission of photons. This turns out to be an important distinction, since spontaneous emission events result in a random walk (as first theorized by Einstein), which is not predicted by Eq. 4.6. This will be relevant for our discussion of the Magneto-Optical Trap. When emission is dominated by the spontaneous process, the atoms experience a constant force (averaged over may cycles)

$$\mathscr{F}_{pressure} \rightarrow \left\langle \mathbf{F} \right\rangle_T = \mathscr{R}(\Delta) \left\langle \mathbf{p}^{abs}_{photon} \right\rangle_T \tag{4.7}$$

where $\mathbf{p}^{abs}_{photon}$ is the momentum of the absorbed photon, $\mathscr{R}(\Delta)$ is the rate at which

absorption-spontaneous emission rates occur when the detuning of the photon from resonance is Δ (which may be calculated quantum-mechanically by considering an atom with only two states). Note that we have assumed that the atom returns to its initial state after emission. In this picture, the dissipative effect of the radiation pressure force is the result of the emitted photon which, due to the Doppler effect, leaves at a higher frequency (in the frame of the atom) than it came in. This only occurs, however, when atom slows down upon absorption of the photon. (We note that we have neglected the Doppler shift of the atom: as it experiences the radiation pressure force, the frequency of the wave in its frame of reference changes).

In the following, we discuss how $\mathscr{F}_{pressure}$ and $\mathscr{F}_{dipole}$ may be used to create an ultracold gas, and how this gas may then be observed.

4.1.1 The Zeeman Slower

Neutral atom traps are typically too shallow to load a hot atom source created by sublimation or evaporation— the atoms are too fast to be stopped by the forces of the traps. Before the atoms from the source can be trapped, they must be slowed.

This can be accomplished via the dissipative radiation pressure force: atoms may be slowed by forming them into a beam (by shooting the evaporated/sublimated atoms out of a nozzle) and counterpropagating laser beam along an axis z which is red-detuned from a two-level transition. The Doppler shift of beam in the frame of the atoms makes them resonant with the light. As an atom is slowed, however, the detuning of the laser beam in the frame of the atom becomes Doppler-shifted outside of the bandwidth of the atomic transition, $\Delta \rightarrow \Delta(v) = \Delta_0 - \mathbf{k}\cdot\mathbf{v}$ with $v = v(z)$ (where z is the axis along the beams, $\mathbf{k}$ is the incident laser wavevector, $\mathbf{v}$ is the velocity of the incoming atom) so that the radiation pressure force is no longer exerted. In order to apply the radiation force over the entire trajectory of the atom, the resonance condition must be maintained as the atom decelerates.

To do this, we can use the Zeeman effect to tune the resonance frequency with an applied magnetic field $\mathbf{B}(z)$. The resonance frequency then shifts $\Delta(v) \rightarrow \Delta(v, B) = \Delta_0 - kv + \frac{\mu}{\hbar}B$. Since the atoms and the laser counterpropagate, the Doppler shift is always negative, and the Zeeman shift must always be positive. This means that only the upshifted state (with $\boldsymbol{\mu} \| \mathbf{B}$) can be used. Orienting $\mathbf{B} \| \hat{\mathbf{z}}$, the use of circularly polarized light allows selective absorption of either the upshifted (or the downshifted state) by using the appropriate handedness. We note that if $\mathbf{B} \perp \hat{\mathbf{z}}$, both the upshifted and the downshifted states can be excited with a linear polarization perpendicular to the magnetic field. This is undesirable,

as the atoms may be "optically pumped" from the upshifted state to the downshifted, so that they no longer absorb light resonant with the upshifted state. Further, the fraction of absorbed light by a one state is reduced.

With $\mathbf{B} \parallel \hat{\mathbf{z}}$ and the correct circular polarization used, the problem is to find $B(z)$ so that Δ is constant as v changes, that is, $\Delta(v(z), B(z)) = \Delta(v(z'), B(z'))$. We then need to know the speed as a function of position $v(z)$. If the Doppler shift is completely countered by the Zeeman shift, the rate of photon absorption is constant, and therefore the force is constant too. The constancy of the force allows the speed to be easily computed as a function of position $v(z)^2 = v(0)^2 - \frac{2F}{m}z$. To keep the detuning the same throughout the trajectory, then, we must have $-kv(0) + \frac{\mu}{\hbar}B(0) = -kv(z) + \frac{\mu}{\hbar}B(z)$ which allows the spatial dependence of the magnetic field to be computed

$$B(z) = B(0) + \frac{\hbar k}{\mu}\sqrt{v(0)^2 - \frac{2F}{m}z} - \frac{\hbar k}{\mu}v(0). \tag{4.8}$$

We note that, if the magnetic field is oriented parallel to the direction of the laser, the magnetic field at the beginning of the trajectory $B(0)$ is maintained at a high bias in order to maintain the separation between the states, avoiding the "optical pumping" problem mentioned above. The light intensity and detuning may be chosen in order to optimize Eq. 4.7. Note that the force comes from absorption followed by spontaneous emission, so the laser should not be at a high-enough intensity to drive stimulated emission.

This setup is called a "Zeeman Slower," and can exert huge forces on atoms, even stopping and reversing atoms along one direction when the atoms are initially hundreds of Kelvin above room temperature. Note that the random emission of the spontaneously-emitted photons induces motion into the two directions perpendicular to the incoming beam.

4.1.2 The Magneto-Optical Trap

The radiation pressure force may be used to form a trap when one makes the following observation: if two beams are made to counterpropagate and are tuned slightly below a resonance frequency of an atom, then the atom will always experience a net force that opposes its motion. For if it moves along the direction of one beam, the Doppler shift of the beam in the frame of the atom will move the observed frequency further from resonance, lowering the probability of absorption and therefore lowering the average force exerted along the atom's motion; and if it moves against the direction of a beam, the

Doppler shift of the beam in the frame of the atom moves the observed frequency closer to resonance, increasing the probability of absorption and therefore increasing the average force counter to the atom's motion. The average force will then always oppose the motion of an atom, which both creates a trapping force for and removes energy from the atoms. Three dimensional trapping may be realized by applying pairs of counterpropagating beams in all three dimensions. The Brownian motion induced by the absorption-spontaneous emission cycles will, however, result in atoms leaving the overlapping region of the three overlapped beams, which means that the atoms are no longer exposed to the optical forces. To confine atoms to the region formed by the overlapped beams, the direction of the beam absorbed must be made spatially selective, which is accomplished by employing a spatially-varying Zeeman shift. We describe this setup below.

Using Eq. 4.7, the force on an atom in the crossed beams is

$$\left\langle \mathbf{F} \right\rangle = \mathscr{R}(\Delta_+)\left\langle \mathbf{p}^{abs}_{photon} \right\rangle + \mathscr{R}(\Delta_-)(-\left\langle \mathbf{p}^{abs}_{photon} \right\rangle) \tag{4.9}$$

where $\Delta_\pm = \Delta_0 \pm \mathbf{k}\cdot\mathbf{v}$ are the detunings from resonance for the two beams where $\mathbf{v}$ is the incoming velocity and $\mathbf{k}$ is the incoming wavevector. Take $|\Delta_0| >> |\mathbf{k}\cdot\mathbf{v}|$ and let $v_k \equiv \mathbf{v}\cdot\hat{\mathbf{k}}$. Taylor-expanding the rates about the velocity, we see that we have a viscous damping force $\left\langle \mathbf{F} \right\rangle = -\mathbf{b}v_k$, where $\mathbf{b} \equiv 2k\left\langle \mathbf{p}^{abs}_{photon} \right\rangle \frac{\partial \mathscr{R}}{\partial \Delta}\Big|_{\Delta_0}$.

Now, to make the trapping forces spatially-dependent, the resonance frequency of the atoms may be spatially tuned using the Zeeman effect, as was done for the Zeeman Slower: $\mathscr{R}(\Delta(v)) \rightarrow \mathscr{R}(\Delta(v,B))$, where $B = B(\mathbf{r})$ is the magnetic field that induces the Zeeman effect. An atom which leaves the center of the overlapped beams must be made to preferentially absorb light which will force it back to the center. But how can the effect of one laser beam be different from the counterpropagating laser beam, when they must be maintained at the same frequency? This problem is overcome by using the polarization-dependence of the Zeeman-shifted spectral lines. When the magnetic field is oriented along the direction of the beams, counter-clockwise circularly polarized light is associated with the upshifted spectral line, and clockwise circularly polarized light is associated with the downshifted spectral line. Then, by making one beam circularly polarized with a given handedness and the other circularly polarized with the opposite handedness, the two counterpropagating beams can be made to act on two different states of the atom

$$\left\langle \mathbf{F} \right\rangle = \mathscr{R}(\Delta^{\circlearrowleft}_+)\left\langle \mathbf{p}^{abs}_{photon} \right\rangle + \mathscr{R}(\Delta^{\circlearrowright}_-)(-\left\langle \mathbf{p}^{abs}_{photon} \right\rangle). \tag{4.10}$$

Now that the two counterpropagating beams can be made to have different effects on the atom in space, what magnetic field results in a trapping force? Recall that the only asymmetry in the Zeeman effect comes from which circularly-polarized beam is upshifted and which is downshifted. If the magnetic field direction is reversed, the circular polarization associated with each state switches. This means that, when the counterpropagating beams are at a frequency near resonance with the one of the shifted states, the atom can switch from absorbing the beam with one circular polarization to absorbing the beam with the opposite circular polarization at a point where the direction of the magnetic field flips. This, in turn, means that the direction of the average radiation pressure force will change direction at this point. By choosing the appropriate circular polarization with the given magnetic field direction, then, the atoms can experience an average force that directs them towards the zero-point in the magnetic field (oriented along the axis of the beams). Let the magnetic field vary linearly in the vicinity of the zero-point. Keeping the field the same in two directions (with $\boldsymbol{\rho}$ being the radial vector in this plane), $\boldsymbol{\nabla}\cdot\mathbf{B}=0$ implies that we must then have

$$\mathbf{B} = C\boldsymbol{\rho} - 2\,C\mathbf{z}. \tag{4.11}$$

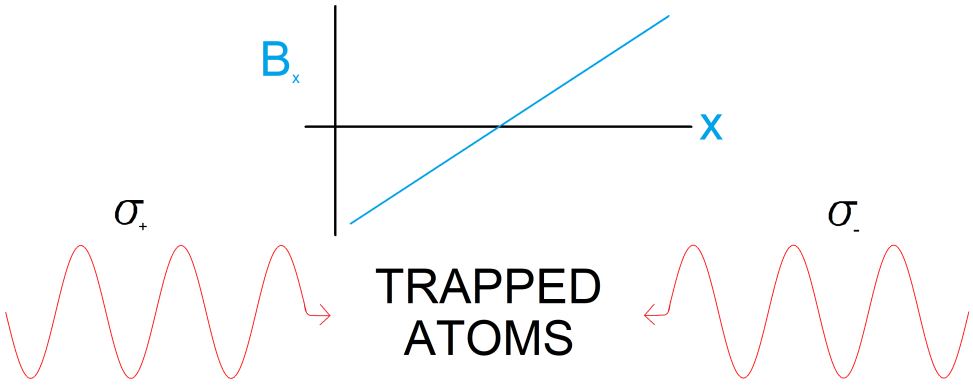

Figure 4.2: A depiction of the Magneto-Optical Trap (in one dimension x). Atoms experience a viscous force due two counter-propagating red-detuned beams, the motion towards either of which results in preferential absorption from the beam counter to the atom's motion. Spatial confinement is established by employing the Zeeman effect: a magnetic field oriented along the direction of the beams B_x varies linearly through a zero-point, so that when the counter-propagating beams are made to have opposite circular polarizations (oriented appropriately relative to the magnetic field), absorption occurs preferentially from a beam which will force the atom back to the $B_x = 0$ point.

Using the expression for $\Delta(v,B)$ in the last section, and taking the Zeeman shift to be much less than the detuning of the beams $|\frac{\mu}{\hbar}B| << |\Delta_0|$, we may Taylor-expand $\mathscr{R}$ in both v and $\mathbf{r}$ to obtain

$$\left\langle \mathbf{F} \right\rangle = -\mathbf{b}v - 2\boldsymbol{\kappa}_{\boldsymbol{B}}\rho - \boldsymbol{\kappa}_{\boldsymbol{B}}z. \tag{4.12}$$

where $\boldsymbol{\kappa}_{\boldsymbol{B}} \equiv C\frac{\mu}{\hbar}\left\langle \mathbf{p}^{abs}_{photon} \right\rangle \frac{\partial \mathscr{R}}{\partial \Delta}\Big|_{\Delta_0}$. The average force now acts to damp the motion of the atom *and* confine it near the zero-point in the magnetic field, forming a "Magneto-Optical Trap" (MOT). Note that the forces are half as strong in the $\hat{\boldsymbol{\rho}}$ plane compared the $\hat{\mathbf{z}}$ direction, so that the distribution of the trapped atoms will be ellipsoidal. We further note that we have assumed that the atom returns to its initial state after emission. If this is not the case, it is possible to use a "repumper" beam to transfer the atom back into the initial state.

The damping component of the force causes the atoms to lose their energy at a rate $P = \mathbf{F}\cdot\mathbf{v} \approx -v\mathbf{b}\cdot\mathbf{v}$ until the energy input from the spontaneously-emitted photons balances the energy output from the lower frequency of the emitted photon compared to the absorbed photon. The removed energy may be optimized with an appropriate choices of the beam power and frequency. This translates into optimizing $\mathbf{b}$, which happens when $\partial\mathscr{R}/\partial\Delta|_{\Delta=\Delta_0}$ is optimized. For a two-level atom, the detuning which optimizes $\partial\mathscr{R}/\partial\Delta|_{\Delta=\Delta_0}$ is $\Delta = -\Gamma/2$, where Γ is the natural linewidth of the spontaneously-emitted photon. The equilibrium kinetic energy reached with this detuning is the lowest possible, and the associated temperature is called the "Doppler limit" $k_B T_{Doppler} = \hbar\Gamma/2$. We note that we have neglected the re-absorption of scattered light throughout this analysis.

4.1.3 Evaporative Cooling

While $T_{Doppler}$ is on the order of milliKelvin for ^{6}Li, we must further lower the temperature in order to meet the requirements listed at the beginning of this chapter. To reach colder temperatures, we turn to evaporative cooling.

In Evaporative Cooling, energy is removed from the sample by allowing particles that acquire high energy through collisions to escape. The temperature may be continuously lowered for a thermally isolated sample by forcing the hottest particles to leave at a pace which allows enough time for the high-energy end of the thermal distribution to be re-populated through collisions. There is no mechanism in this method which imposes a fundamental limit on the achievable temperatures, but there is a trade-off between the number of atoms lost and the amount of energy removed. The ability to tune the interactions to be strongly interacting via the magnetic Feshbach resonance increases the efficiency

of this process. With evaporative cooling, temperatures in the nanoKelvin range may be approached. Even at these low temperatures and higher densities, however, the sample does not "freeze," as it remains dilute enough that two-body collisions dominate.

To avoid the heating due to spontaneous emission, the atoms must be transferred to a trap formed by conservative forces.

4.1.4 The Optical Dipole Trap

To form a trap with conservative forces, we may use a magnetic trap or an optical trap based on the dipole force $\mathscr{F}_{dipole}$. The magnetic traps are limited to trapping spin states oriented oppositely to the magnetic field, but $\mathscr{F}_{dipole}$ is almost completely spin-independent. Evaporative cooling may be performed in the optical trap by lowering the power of the trapping beam.

To create a trap with the dipole force, a local maximum or minimum in the light intensity is required. The frequency of the beam ω must be detuned far from the atom's resonant frequency ω_0 in order to avoid the radiation pressure force. Either $\omega < \omega_0$ and $\alpha(\omega) > 0$, in which case the atoms will be attracted to points of maximum intensity, or $\omega > \omega_0$ and $\alpha(\omega) < 0$, in which case the atoms will be repelled from points of maximum intensity. The time-dependence of the electric field in a wave allows for a local maximum in the field strength to be realized. One way to achieve a local extreme in light intensity is to create a standing wave, which forms both local maxima and local minima. Another is to simply focus a beam, forming a local maximum . Here we consider the latter approach, considering a trap formed by a focused monochromatic gaussian beam with a frequency far below the resonance frequency of the atom.

The "gaussian beam" is the azmuthally-symmetric (or elliptically-symmetric) beam profile $\mathscr{E}(\mathbf{r})$ that is consistent with Maxwell's equations. After passing a polarized beam through a lens, the (azmuthally-symmetric) beam profile satisfies

$$|\mathscr{E}_z|^2 \approx |\mathscr{E}_0|^2 \left(\frac{w_0}{w(x)}\right)^2 e^{-2\rho^2/w^2(x)} \tag{4.13}$$

where x is the axial distance from the focus, ρ is the radial distance from the center of the beam, k is the wavenumber, the "spot size" $w(x) = w_0\sqrt{1+(x/x_0)^2}$ is the field $1/e$ radius, and $x_0 = \frac{1}{2}k\,w_0^2$ is the "Rayleigh length." The above equation is obtained in paraxial approximation, where it is assumed that the beam retains polarization as it is focused. In reality, though, the polarization remains orthogonal to the local wavevector. The field

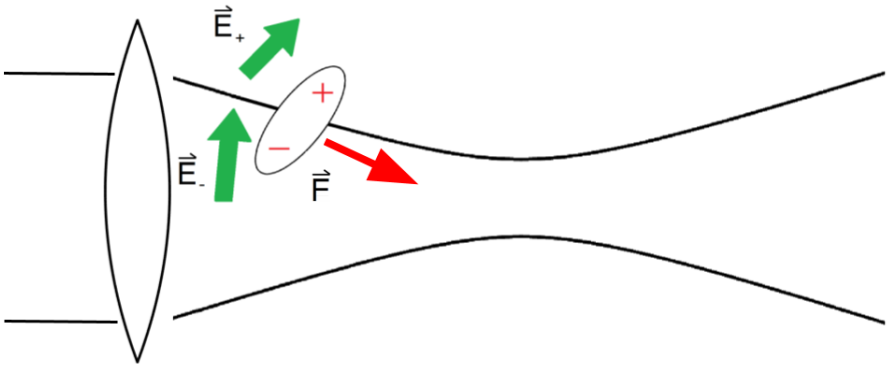

Figure 4.3: A depiction of the action of an optical dipole trap formed by focusing a far-red-detuned Gaussian laser beam. The atom polarizes along the direction of the electric field, then feels a net force when the fields at each pole are different (as occurs near the focus).

vector then has some component directed toward the focus, which allows the dipole to feel a trapping force in all three dimensions (see Fig 4.3). Now, from Eq. 4.5, the potential associated with the dipole force is

$$U(\mathbf{r}) = -\frac{1}{4}\text{real}\big[\alpha(\omega)\big]|\mathscr{E}(\mathbf{r})|^2. \tag{4.14}$$

If atoms are cold enough relative to the trap depth to remain around the focus ($x << x_0, \rho << w_0$), the trap may be well-approximated as harmonic

$$U \approx U_0 + \frac{1}{2}m\omega_\rho^2\rho^2 + \frac{1}{2}m\omega_x^2 x^2 \tag{4.15}$$

where U is the potential energy, m is the mass of an atom, and $U_0 \equiv U(\mathbf{0})$ is the trap depth. Note that the necessary minimum beam intensity can be calculated by setting $U_0 = k_B T_{Dopple r}$ (to get high intensities, though, one cannot focus the beam to an arbitrarily small size, as trapping volume must be close to the volume of the MOT for efficient transfer). Performing the multi-variable Taylor expansion of $|\mathscr{E}_z|^2$, we have

$$\omega_x = \sqrt{\frac{2U_0}{m x_0^2}}, \qquad \omega_\rho = \sqrt{\frac{4U_0}{m w_0^2}}. \tag{4.16}$$

$|\mathscr{E}_0|^2$ may be related to the beam intensity in order to relate the above terms to the measurable quantities of beam power and size. As the Rayleigh length x_0 differs from field waist w_0 by a factor $k w_0$, $x_0 >> w_0$ at optical wavelengths, the axial trapping force is much weaker

than the radial trapping force. To get strong trapping forces axially, one may cross two focused beams perpendicularly. This can also increase the Evaporative Cooling efficiency, as the sample becomes more dense.

The radial trap frequency ω_ρ may be measured by modulating the laser power until heating due to parametric resonance occurs at $2\omega_\rho$. While this can be done to measure the axial trap frequency ω_x as well, we find a more accurate measurement by using another focused optical dipole trap to move the atoms to the edge of the trap, turning off this second beam, and measuring the oscillation of the cloud in the original trap. We note that any periodic noise in the laser power at $2\omega_x$ or $2\omega_\rho$ results in heating by parametric resonance [Savard et al. (1997)].

While the optical dipole trap is spin-independent on its own, in our system, the curvature in the magnetic field used to tune the interactions introduces spin-dependence into the overall potential. Evidence of the spin-dependence is given in the RF spectra shown § 5.1.1. Along the axis of the trapping beam, the magnetic force is directs atoms toward the focus. Radially, the magnetic force repels atoms from the axis of the beam. This applies for the Li^6 hyperfine spin states $|1\rangle$ and $|2\rangle$ ($|\uparrow\rangle$ and $|\downarrow\rangle$) used in our experiments. In the axial direction, the magnetic and optical forces are comparable. In the radial direction, however, the optical force dominates over the magnetic force. To avoid any offset in the two potentials (which is especially problematic for evaporative cooling), the focus of the optical dipole trap is aligned where the magnetic forces vanish.

4.1.5 Absorption Imaging

We observe the ultracold gas by shining a laser pulse on the sample and measuring the change in the beam properties, from which we may extract the density of the atoms. These properties could include the intensity, phase, or polarization. Our observation method is to measure the change in intensity due to absorption, which we refer to as "absorption imaging": the atoms are illuminated with a resonant laser pulse and the transmitted light is detected with a spatial-resolution on the order of $10\,\mu$m. This blasts the atoms out of the trap, accelerating them with the radiation pressure force. Afterwards the same pulse is detected without the atoms, which we use to measure the intensity that was incident on the atoms. By measuring the spatially-resolved change in intensity due to the atoms, and with knowledge of the optical properties of ^{6}Li, we can extract the 2-D density of atoms. Since the resonant frequency is spin-dependent in the high magnetic field (due to the Zeeman effect and hyperfine structure; see § A), we measure the density associated with each spin

state.

The relationship between the attenuation of the intensity and the atom density can be found with Maxwell's equations: the known (dissipative) polariziblilty of a single ^{6}Li atom to an optical beam, which is related to $\alpha(\omega)$, allows the change in the electric field of the beam to be found for an arbitrary density. Inverting the result, the density may be found. The calculation may also be performed from a two-body scattering perspective—in this case, between atoms and photons. Let the cross section between an atom and a photon be $\sigma_{ap}(\Delta)$, where Δ is the detuning of the incident photons from the atomic resonance. Then, by definition, the probability of a collision between an atom and a photon at a position $\mathbf{r}$ due an incoming flux $\mathscr{F}_p$ of photons during a short time increment Δt is $P_{ap}(\mathbf{r}) = \sigma_{ap}(\Delta)\mathscr{F}_p(\mathbf{r})\Delta t$. We consider a small volume element located at $\mathbf{r}$ with a cross sectional area of ΔA and length Δz along the direction of the incoming photons. The number of collisions in this volume during Δt is $N_c = \sigma_{ap}(\Delta)\mathscr{F}_p(\mathbf{r})\Delta t\, N_a(\mathbf{r})$, where $N_a(\mathbf{r})$ is the number of atoms in the volume element. With one photon lost from the incident beam per collision (neglecting stimulated emission), the change in the number of photons N_p is $\Delta N_p = -N_c$. Dividing by the volume of the element $\Delta A\Delta z$ and by the time increment Δt, we have $\Delta\mathscr{F}_p(\mathbf{r})/\Delta z = -\sigma_{ap}(\Delta)n_a(\mathbf{r})\mathscr{F}_p(\mathbf{r})$, where $n_a(\mathbf{r})$ is the density of atoms at position $\mathbf{r}$. Since the flux of photons is proportional to the intensity of the beam, we have, in the continuum limit,

$$\frac{dI(\mathbf{r})}{dz} = -\sigma_{ap}(\Delta)\, n_a(\mathbf{r})\, I(\mathbf{r}). \tag{4.17}$$

We note that $\sigma_{ap}(\Delta)$ can be a function of the intensity I due to saturation effects. We make the beam large enough to illuminate the atoms uniformly, so $I(\mathbf{r}) = I(z)$. Solving the differential equation and isolating $n_a(\mathbf{r})$, we integrate over the line-of-sight z to calculate the 2-D density using the observed changes in intensity, obtaining an image like that shown in Fig. 4.1.

The result is, in general, a function of the intensity of the beam. If the intensity is too low, all of the light is absorbed and some of the atoms are not detected. If the intensity is too high, the force on the atoms can be so high that they are Doppler-shifted out of resonance during the pulse. We choose the intensity between these two regions, where the measured atom number is not sensitive to local changes in the intensity.

The profile of the beam must be magnified in order to detect it with a camera with spatial resolution. To determine the magnification, we can take a picture of atoms trapped in a standing wave of the CO_2 laser, for which we know the spacing between the maxima in the laser intensity ($10.6/2 = 5.3\,\mu$m), where atoms are trapped.

To lower the density of the atoms (which avoids complete absorption) and increase the imaged radial size, we generally release the gas from the optical dipole trap for a short time before imaging. The timescale for doing so is small compared to the axial trap frequency, such that the axial profile is effectively unchanged, while the radial profile has expanded. We loss access to what the radial profile was before expansion, but are able to back out the radial width before expansion by assuming that the pressure is isotropic (as it should be). For a harmonic trap, this assumption results in $\frac{1}{2}m\omega_\rho^2\langle\rho^2\rangle = \frac{1}{2}m\omega_x^2\langle x^2\rangle$, where the brackets denote spatial averaging.

4.2 Frequency-Stabilization of the Optical Control Beams

In the experiments, we illuminate the ultracold gas with an optical beam resonant with the $g \rightarrow e$ transition (see § 2.3). Spontaneous emission from e results in the loss of both of the interacting atoms from the trap. The apparatus for generating this beam is the optical control system discussed in § 2.3, which generates two beams [Jagannathan (2016); Arunkumar (2018)]: the "control" beam which light-shifts the energy of the g state, and the "EIT" beam which suppresses the accompanying loss via Electromagnetically-Induced Transparency. The function of the optical control system is to produce these beams with (1) stable absolute frequencies, (2) a stable frequency difference, and (3) the ability to tune both frequencies. The stability of the frequency difference is much more important than the absolute frequencies, as this is the relevant parameter for EIT. Only the control beam is used in the loss experiments, but the entire apparatus must be understood in order to stabilize its frequency with a tunable locking point.

Near the weakly interacting regime between hyperfine states $|1\rangle$ and $|2\rangle$, the corresponding $g \rightarrow e$ frequency is $\approx$ 444.1398 THz and the corresponding $g_2 \rightarrow e$ frequency is $\approx$ 444.1965 THz. In order to stabilize the frequency difference between the two (as well as the absolute frequency) we first use an absolute common frequency reference point. We choose iodine gas to provide this reference, with absorption peaks located $\approx$ 2 GHz from the control laser frequency. We cannot use an Acousto-Optic Modulator (AO) to overcome this frequency difference, so we introduce a "reference" laser to operate at a frequency in the iodine absorption spectrum. The reference and control beam frequencies are close enough to form an electronically-observable beat. The $\approx$ 60 GHz difference between the EIT beam and iodine frequencies is, however, too large to observe electronically. In order to use this reference for the EIT beam as well, an optical cavity is kept resonant with the

reference laser, which can then be used to keep the EIT beam resonant with the cavity at a much higher frequency, “climbing” up the frequency difference along the “ladder” of periodic resonances. The lock created by the reflection off of the cavity allows the laser frequency to be stabilized to one of the cavity’s resonance frequencies quickly, so that rapid changes can be accounted for as well as slow drifts.

At a high level, the design (depicted in Fig. 4.4) is as follows: The reference beam is split into three paths. One path is directed into the cavity, and the reflection is observed with a photodiode. This signal is used to create a Pound-Drever-Hall lock, which provides feedback into the laser so that its frequency is resonant with a cavity resonance frequency. Another path is made incident on the iodine gas, and the transmission signal is recorded with a photodiode. This is used to generate an absolute frequency reference lock, which locks the variable length of the cavity so that it stays resonant with the given iodine transition. When the iodine signal is narrowed using Saturation Absorption Spectroscopy (described below), the reference laser becomes both extremely sensitive to changes in frequency (due to the narrowed iodine signal) and very quick to correct them (due to the rapid response of the cavity). The third path of the reference laser combines with a path of the control laser, and this combination is made incident on a photodiode. The frequency difference between the two is low enough to observe in the electronic signal, which can be used to lock the control laser frequency in a tunable fashion. A path of the EIT beam is directed into the cavity and locked in the same way as the reference laser is (the Pound-Drever-Hall lock), even though the difference in frequency between the two lasers is ≈ 62 GHz. An AOM placed before the cavity allows the locking point of the cavity to be tuned within the range of the AOM.

In the following, we overview the locks used, deriving the error signal observed in each case. An “error signal” is what is used to send the appropriate feedback to the laser in order for it to remain at the desired frequency. It is interesting to note that we use resonant phenomena to drive resonant phenomena.

4.2.1 The Absolute Frequency Reference Lock

A laser beam incident on a sample of atoms is absorbed at discrete frequencies, resulting in “dips" in the transmission spectrum (see Figure 2a). These natural resonances provide absolute frequency reference points (for an atom at rest). However, the dips are usually symmetric about the resonance frequency, so that one cannot use the transmission/absorption signal to determine whether the laser frequency is higher or lower than the resonance frequency. This presents a problem when attempting to use this signal to lock a laser, as a

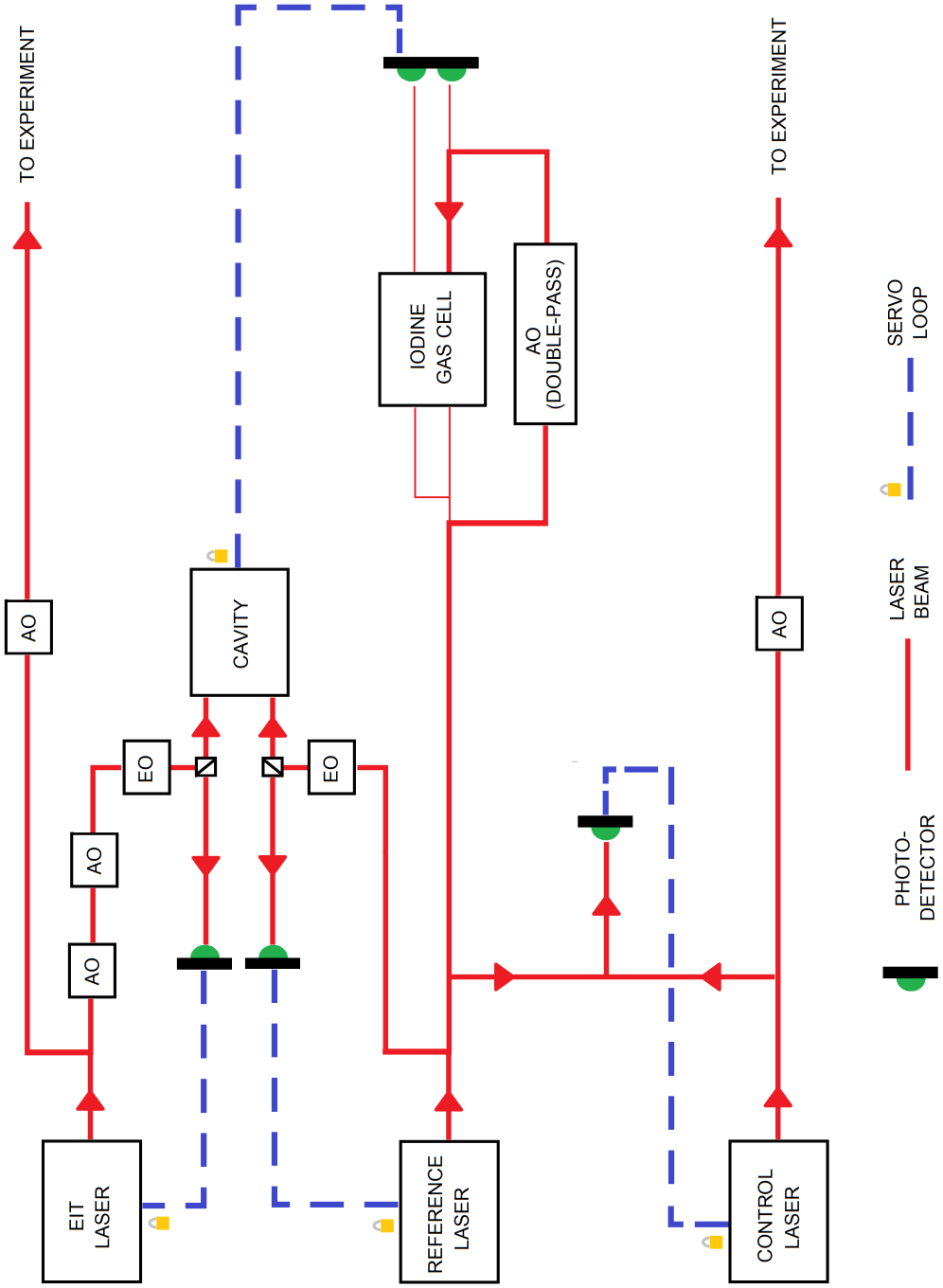

Figure 4.4: High-level diagram of the two-beam optical control system. Here, "AO" refers to an Acousto-optic modulator (which shift the frequency), and "EO" refers to an electro-optic modulator.

servo loop cannot discriminate between an increase and decrease in laser frequency. To lock the laser, we must inject some knowledge about which side of the resonance we are on. We can do this by *intentionally* changing the frequency of the laser incident on the atoms in a controlled way: by scanning around a given point and weighting it with the scan signal, we effectively take the difference between the neighboring points (see Figures 2b and 2c).

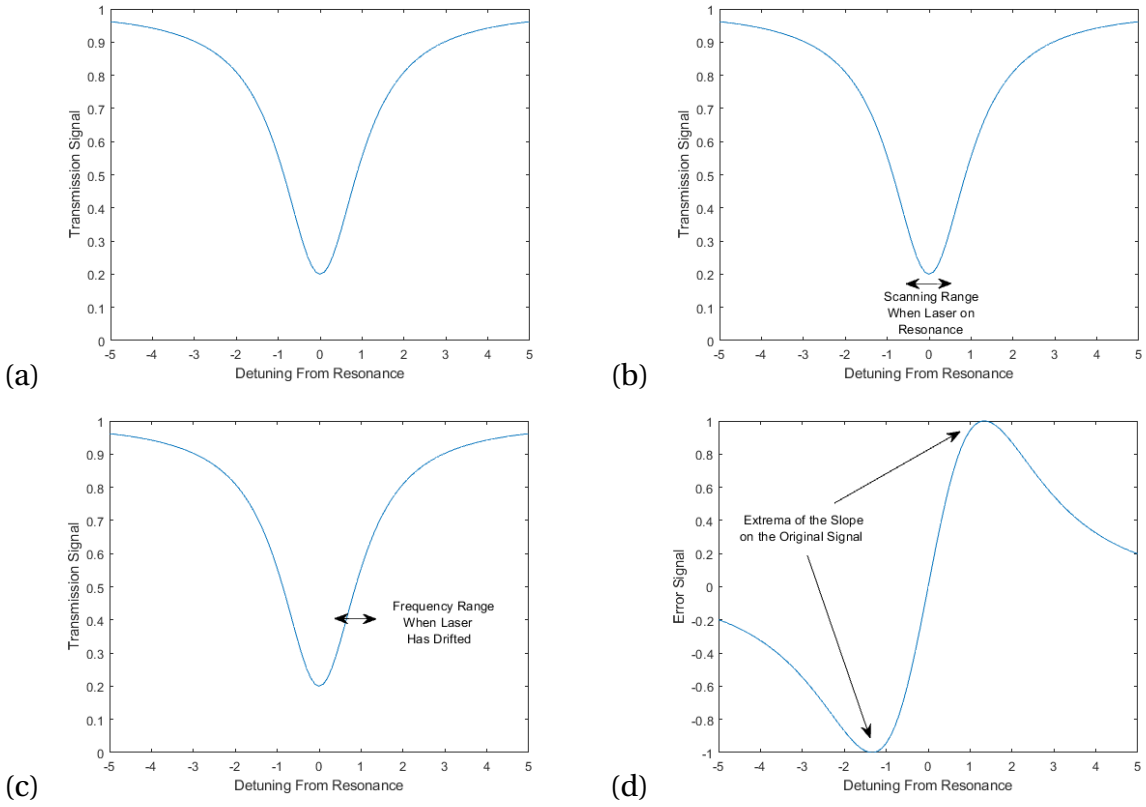

Figure 4.5: Generation of a locking signal from an absorption spectrum. (a) The transmission of laser light near a resonance in the medium through which it is passing. (b) Illustration of the frequency modulation of the laser at the resonance. (c) Illustration of the frequency modulation of the laser when off resonance. (d) Signal generated by weighting the modulated signal with a signal of the same frequency and averaging.

We will show that this method is equivalent to taking the derivative of the dip. Let the transmission spectrum through a sample with a resonance at f_0 be given by $\mathscr{P} = \mathscr{P}(f_S - f_0)$, where f_S is the frequency of the beam exposed to the sample. If we scan over the peak by modulating the laser frequency before it reaches the sample f_L, then $f_S = f_L + \epsilon(t)$. For

$\epsilon << |f_L - f_0|$,

$$\mathscr{P} \approx \mathscr{P}(\epsilon = 0) + \epsilon \left.\frac{\partial \mathscr{P}}{\partial \epsilon}\right|_{\epsilon=0}. \tag{4.18}$$

The derivative can be extracted from this signal by choosing ϵ to be periodic and multipling the signal by the same periodic function. Averaging over an appropriate time T, the non-periodic component vanishes, and the output is dependent on $\partial \mathscr{P}/\partial \epsilon|_{\epsilon=0}$ and the phase ϕ between the two periodic functions. Defining the error signal $\mathscr{E}$,

$$\mathscr{E} = \frac{1}{T}\int_0^T d\,t\, \mathscr{P}\big[\epsilon(t)\big]\sin(\omega t + \phi). \tag{4.19}$$

With Eq. 4.18,

$$\mathscr{E} \approx \mathscr{P}(\epsilon = 0)\frac{1}{T}\int_0^T d\,t\,\sin(\omega t + \phi) + \left.\frac{\partial \mathscr{P}}{\partial \epsilon}\right|_{\epsilon=0}\frac{1}{T}\int_0^T d\,t\,\epsilon(t)\sin(\omega t + \phi) \tag{4.20}$$

We choose $\epsilon(t) = \Delta + \beta\sin(\omega t)$. With $T >> \frac{2\pi}{\omega}$, the integrals over a single periodic function are very small compared to the integral over the product of periodic signals with the same frequency. Then, $\mathscr{E}$ is proportional to the frequency-derivative of the transmission spectrum

$$\mathscr{E} \propto \left.\frac{\partial \mathscr{P}}{\partial \epsilon}\right|_{\epsilon=0} = \left.\frac{\partial \mathscr{P}}{\partial f_S}\frac{\partial f_S}{\partial \epsilon}\right|_{\epsilon=0} = \frac{\partial \mathscr{P}}{\partial f_L}, \tag{4.21}$$

which results in an asymmetric signal about the resonance frequency, allowing the laser frequency to be stabilized to an absolute point.

It is clear that the steepness of the derivative depends on the sharpness of the dip. A more sensitive lock may then be formed by a sharper dip (a more sensitive lock may also be generated by increasing the gain of the error signal, but this increases sensitivity to noise as well). The sharper dip can be formed by the elimination of Doppler broadening. This can be accomplished without cooling of the sample by using Saturation Absorption Spectroscopy: a strong beam (which we refer to as the "pump") pumps the atoms into the excited state, and a weak counter-propagating beam (the "probe") is overlapped with this beam, driving stimulated emission from the atoms which are Doppler-shifted into resonance with both beams. If the probe is at the same frequency as the pump, only the near-stationary atoms are driven by the probe to stimulated emission. If the probe is detuned by Δ_{AO} from the pump frequency, the velocity class of atoms resonant with both beams and which therefore undergo stimulated emission can be determined by setting

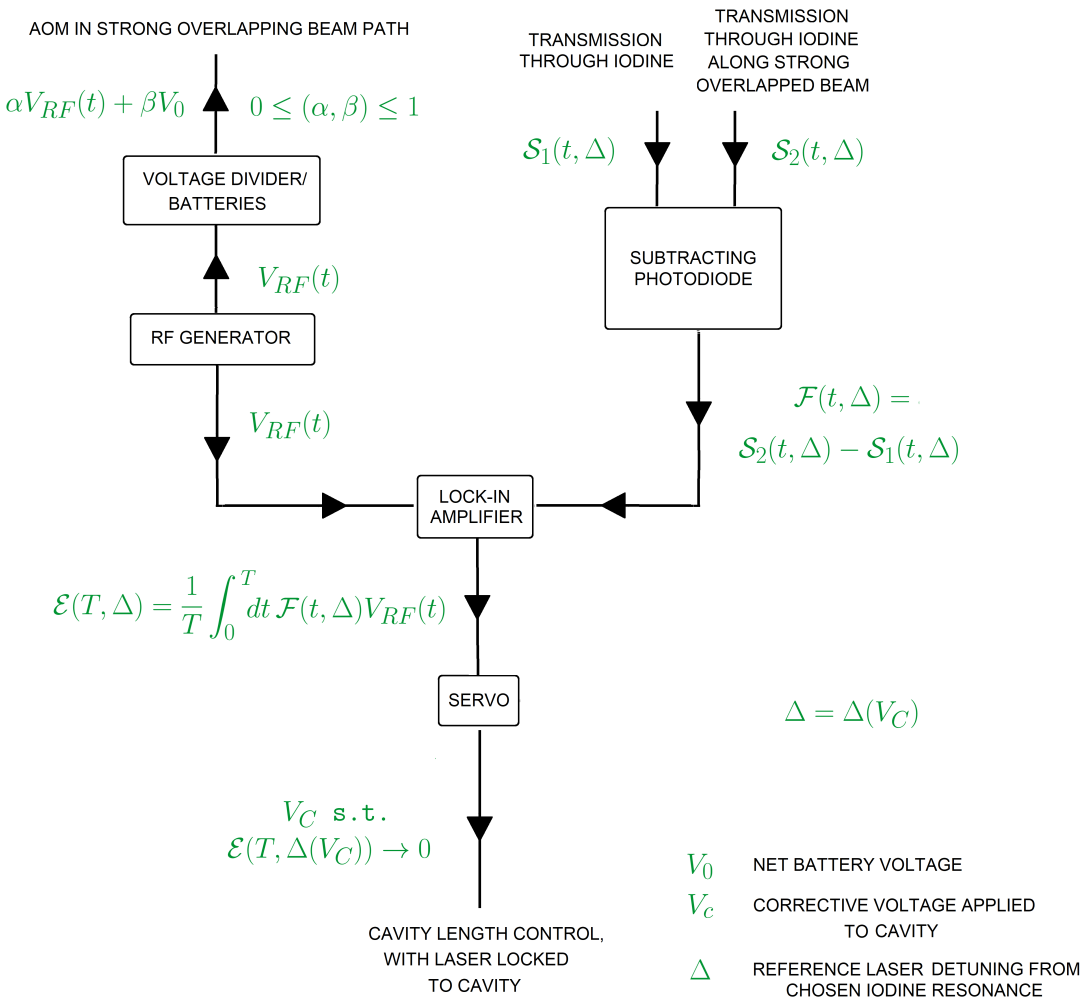

Figure 4.6: Diagram of the absolute frequency reference lock.

$f_{res}^{probe} = f_0 - \frac{v}{\lambda} + \Delta_{AO}$ equal to $f_{res}^{pump} = f_0 + \frac{v}{\lambda}$. The result of this scheme is a narrowed peak in the transmission spectrum over the absorption dip, at a location set by the detuning of the probe. By taking the difference of this signal with that of another weak beam which does not overlap a strong beam, the absorption dip is removed from the signal and the narrowed peak is isolated. This narrowed peak can be turned into an error signal as described above.

A diagram depicting the setup to realize is lock is given in Fig. 4.6.

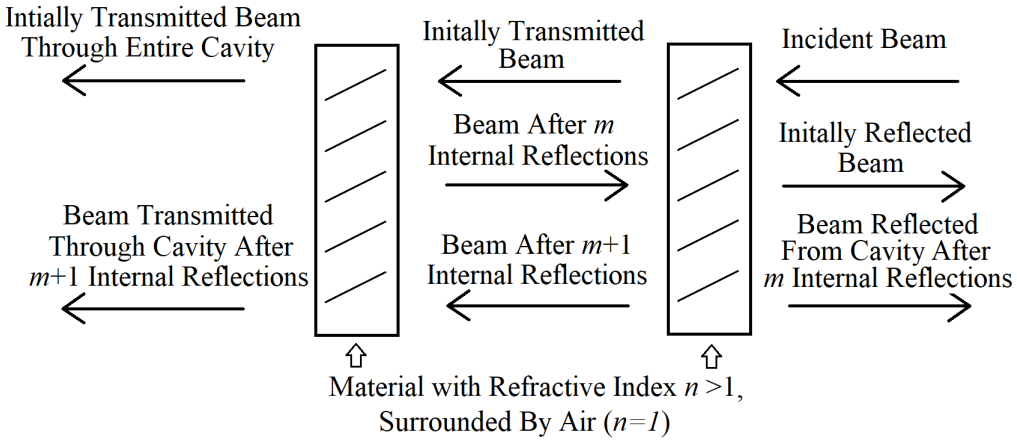

Figure 4.7: The Fabry-Perot Cavity.

4.2.2 The Pound-Drever-Hall Lock

In order to stabilize a laser to a given frequency, the frequency must be able to be observed. Aside from natural resonances, interference phenomena are usually exploited in order to generate an error signal. To do this with a single (coherent) beam, one can interfere the beam with itself by splitting it into two and recombining it after having taken different paths. The frequency-dependent mismatched phases from the different paths can produce an observable frequency-dependent interference signal.

The reflected signal from a one-dimensional optical cavity (a “Fabry-Perot Cavity,") provides a way to generate self-interference which is dramatically sharp in its frequency dependence (see Fig. 4.7). An incident beam is partially transmitted through a surface composed of some highly reflective material, and then can reflect off of a second surface made of the same material. The reflected beam is partially transmitted and partially reflected off of the first. This sets up an infinite series of waves reflected out of the cavity, differing in path length by twice the spacing between the two media.

The infinite combination of waves cancel one another unless they are nearly all in phase. This is the cause of the sharp frequency dependence. We will show this dependence in the intensity of the light reflected from the cavity. Let the incident wave be given by $E_{in} = \Lambda \sin(kx - \omega t)$, where neglect polarization. Let the field at the photodetector positioned to detect the reflected light from the cavity (at $x = 0$) be given by E_{PD}. The total reflection from the cavity is the combination of the initially reflected wave E_{refl} and the infinite series of

waves which have been reflected inside of the cavity $\{E_{O_m}\}$

$$E_{PD} = E_{refl} + \sum_{m=0}^{\infty} E_{O_m}. \tag{4.22}$$

With a reflection coefficient f_R, we have $E_{refl} = -\Lambda f_R \sin(\omega t)$ (note the π phase shift). Now, each time a wave is reflected off of the second surface, it picks up a phase difference $\delta = 2kL$. With the transmission coefficient f_T , a wave reflected $m+1$ times from the second medium is given by

$$E_{O_m} = \Lambda f_T^2 f_R (f_R^2)^m \sin\big[kx + \omega t + (m+1)\delta\big]. \tag{4.23}$$

In the complex representation, the sum of E_{O_m} over m becomes geometric, resulting in

$$\sum_{m=0}^{\infty} E_{O_m} = \Lambda(1-f_R^2) f_R \,\mathrm{imag}\left[e^{i(kx+\omega t)} \frac{e^{i\delta}}{1-f_R^2 e^{i\delta}}\right]. \tag{4.24}$$

Then, with the photodiode positioned at $x = 0$,

$$E_{PD} = \Lambda \,\mathrm{imag}\big[e^{i\omega t} F(\omega)\big] \tag{4.25}$$

where

$$F(\omega) \equiv -f_R + \frac{(1-f_R^2) f_R e^{i\delta}}{1-f_R^2 e^{i\delta}}. \tag{4.26}$$

In order to relate the field observed by the photodetector E_{PD} to the intensity observed by the photodetector, we square it. For $f_R = 0.99$, we obtain a signal as seen in Fig. 4.8a.

We see that the light reflected from the cavity does indeed have a sharp frequency response (set by the reflection coefficient). However, this single-frequency response cannot be used as an error signal, primarily due to its symmetry. In principle, we may overcome this in the same way that an error signal was created from an absorption spectrum. This may be too sensitive though, as the derivative of the curve in the figure approaches infinity at the resonance (furthermore, it turns out that this method is much slower servo loop compared to method we are about to describe). If the frequency is not scanned, we must introduce other frequencies simultaneously in order to have access to neighboring parts of the spectrum. When two frequencies are incident on the cavity, we do not merely get the sum of two single-frequency signals, as the fields interfere. We will show that, by introducing two frequency “sidebands" detuned equally above and below the primary frequency, the beats formed by interference with the primary frequency themselves interfere, and that

this may be used to create an error signal. This method of locking a laser is called the Pound-Drever-Hall lock [Drever et al. (1983)].

The two frequency sidebands with a fraction β of amplitude of E_{in} are introduced at the same polarization and out-of-phase, one detuned by $-\Delta$ from the central (angular) frequency ω, and the other detuned by $+\Delta$. This can be accomplished with an electro-optic modulator. In order to break the symmetry of the signal at ω, one of these sidebands is π phase-shifted. All of this may be accomplished by transmitting the beam through a periodically-modulated electro-optic device before the beam is incident on the cavity. The field at the photodiode is now E'_{PD}

$$E'_{PD} = E_{PD}(\omega) + \beta E_{PD}(\omega-\Delta) - \beta E_{PD}(\omega+\Delta) \tag{4.27}$$

As the light intensity is proportional to the square of the field, the photodiode signal now contains several frequency components.

$$\begin{aligned} E'^2_{PD} =& E^2_{PD}(\omega) + \beta^2 E^2_{PD}(\omega-\Delta) + \beta^2 E^2_{PD}(\omega+\Delta) \\ &+ 2\beta\big[E_{PD}(\omega)E_{PD}(\omega-\Delta) - E_{PD}(\omega)E_{PD}(\omega+\Delta)\big] \\ &- 2\beta^2 E_{PD}(\omega+\Delta)E_{PD}(\omega-\Delta) \end{aligned} \tag{4.28}$$

We wish to extract the component of this signal which is the result of interference terms with the central frequency ω, which we define as E_{int}

$$E_{int} \equiv 2\beta\big[E_{PD}(\omega)E_{PD}(\omega-\Delta) - E_{PD}(\omega)E_{PD}(\omega+\Delta)\big]. \tag{4.29}$$

Expressing E_{int} in terms of F (which is non-trivial),

$$E'_{int}(\Delta) = \Lambda\beta\big[\cos(\Delta t)\text{real}(\eta) + \sin(\Delta t)\text{imag}(\eta)\big] \tag{4.30}$$

where $E'_{int}(\Delta)$ the component of E_{int} with frequency Δ and

$$\eta \equiv F(\omega)F(\omega+\Delta)^* - F(\omega)^*F(\omega-\Delta). \tag{4.31}$$

$E'_{int}(\Delta)$ may be extracted from E'_{PD} by mixing the signal with a local oscillator at frequency Δ, resulting in a signal $\mathscr{S}$,

$$\mathscr{S} \propto E'^2_{PD}\cos(\Delta t + \phi) \tag{4.32}$$

and then sending $\mathscr{S}$ through a low-pass filter. All non-Δ frequency components of E^2_{PD}

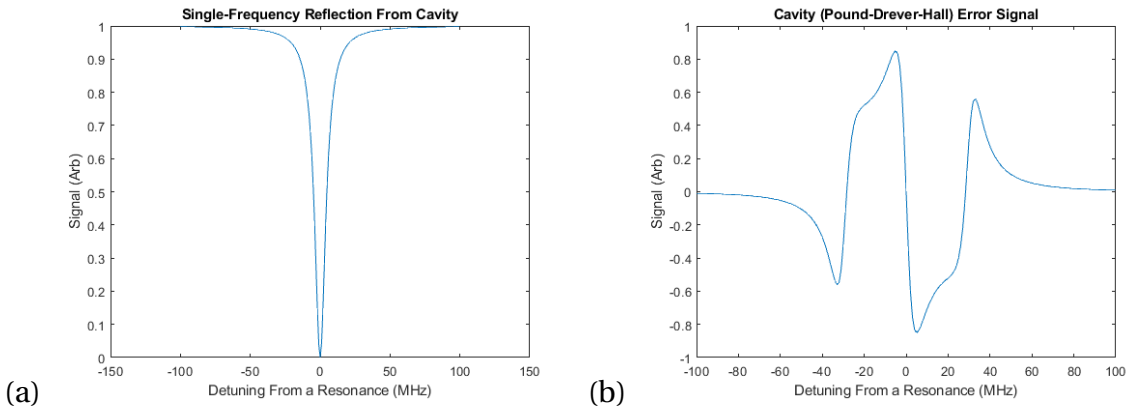

Figure 4.8: Signals obtained from the laser light reflected from the Fabry-Perot cavity with $f_R = 0.99$, $L = 10$ cm as the frequency is scanned. (a) Photodetector readout when the beam is monochromatic. (b) Readout after the photodetector signal is mixed and filtered, for light at the scan frequency superimposed with frequency "sidebands," with the relative local oscillator phase at $\phi = \frac{\pi}{2}$.

vanish, and we are left with a time-independent signal $\mathscr{E}$

$$\mathscr{E} \propto \cos(\phi)\text{real}(\eta) + \sin(\phi)\text{imag}(\eta). \tag{4.33}$$

The purely imaginary component of η ends up resulting in the best error signal, as it is linear for a larger region about the resonance frequency. Tuning the phase of the local oscillator until the purely imaginary component is obtained,

$$\mathscr{E}\left(\phi = \frac{\pi}{2}\right) \propto \text{imag}(\eta). \tag{4.34}$$

The result is shown in Figure 4b. We see that $\mathscr{E}(\phi = \frac{\pi}{2})$ possesses the desired properties of an error signal. Furthermore, as a change in the frequency of the incident beam results in a near-instanteous change of the photodiode signal, and the processing of the photodiode signal is minimal, any deviations from a frequency resonant with the cavity are quickly apparent in $\mathscr{E}$. A diagram depicting the setup to realize is lock is given in Fig. 4.9.

4.2.3 The Tunable Frequency Offset Lock

Let two monochromatic lasers, one comprised of electric field oscillating at f_L which is locked to an absolute frequency reference, and the another of an electric field oscillating at f_{UL} which is unlocked, overlap. The intensity of this linear combination of will have one

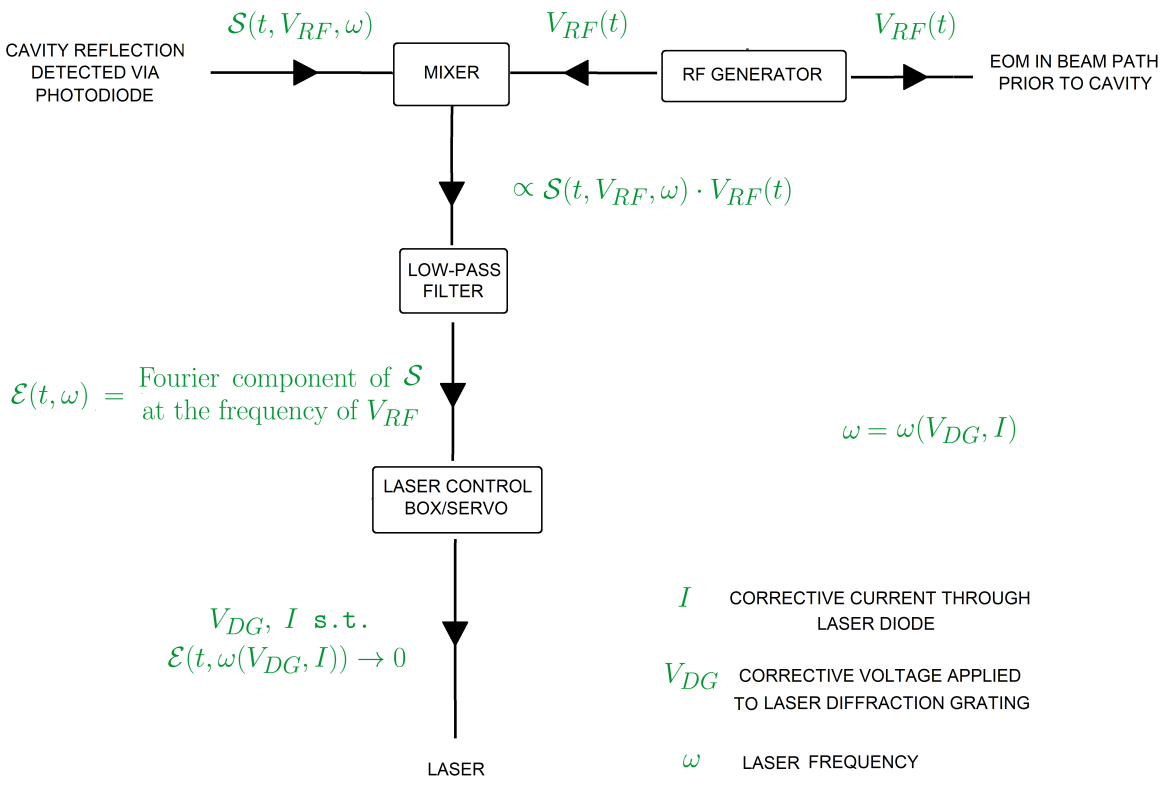

Figure 4.9: Diagram of the Pound-Drever-Hall lock.

frequency component at $f_+ = f_L + f_{UL}$ and another $f_- = f_L - f_{UL}$. If f_- is low enough that it can be observed in an electronic signal formed by shining the combined lasers on, say, a photodiode, then the f_{UL} is now observable electronically, since f_L is fixed. We will show that we can use this electronic signal to build a circuit that generates an error signal that may be used to lock f_{UL} [Schnemann et al. (1999)].

We mix the photodiode signal with a frequency f_- with a local oscillator signal at a frequency f_{RF} and use a low-pass filter, obtaining a signal with a frequency $\Delta f = f_{RF} - f_-$. Since f_{RF} is tunable, Δf is tunable. To create a circuit that can "observe" Δf, we exploit interference phenomena, splitting the signal into two paths with different lengths. In our circuit, the difference in the path lengths is $\Delta L \approx 4$ m. The signals are mixed (that is, multiplied), resulting in one component of the signal oscillating at twice the frequency, and the other which DC. The output is fed into a low-pass filter, so that only the DC signal is left. This is sent to a phase detector (which is a nearly equivalent circuit to the frequency mixer) which in conjunction with a low-pass filter, outputs a signal V_{OUT} proportional to the cosine of the phase difference of the two signals:

$$V_{OUT} \propto \cos\left(2\pi\Delta f \frac{\Delta L}{v}\right) \tag{4.35}$$

where v is the speed of the signal in the cable. When the effect of the low-pass filters are accounted for, we obtain a signal like that in the Fig. 4.10. The signal is asymmetric about several zero points and locally linear around these points, allowing it to function as an error signal. By changing f_{RF} by a given value, the locking point is shifted by the same value. A diagram depicting the setup to realize is lock is given in Fig. 4.11.

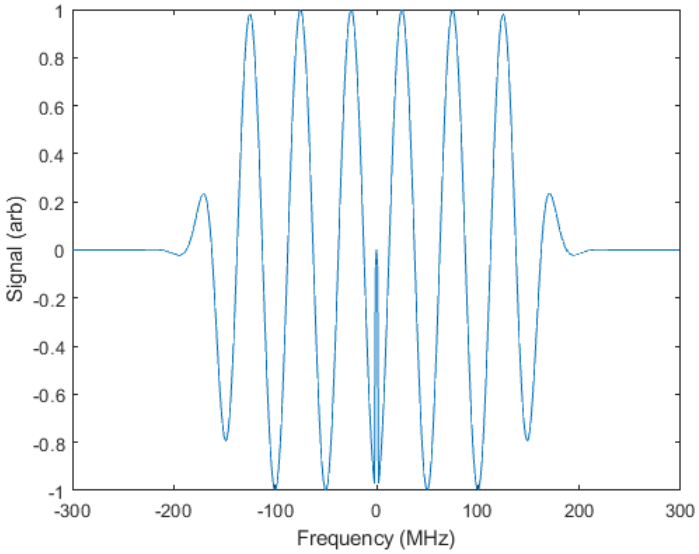

Figure 4.10: Error signal for the tunable probe lock. The periodicity is a result of the changing phase difference between the the two interferometer signals as the probe laser is scanned. The cutoff at ≈ 200 MHz is due to the low-pass filter operating after the photodetector and RF generator signals are mixed. The artefact near the region of equal signal frequencies (the zero-frequency point on the plot) is due to summed frequency component of the mixed interferometer signals passing through the second low-pass filter.

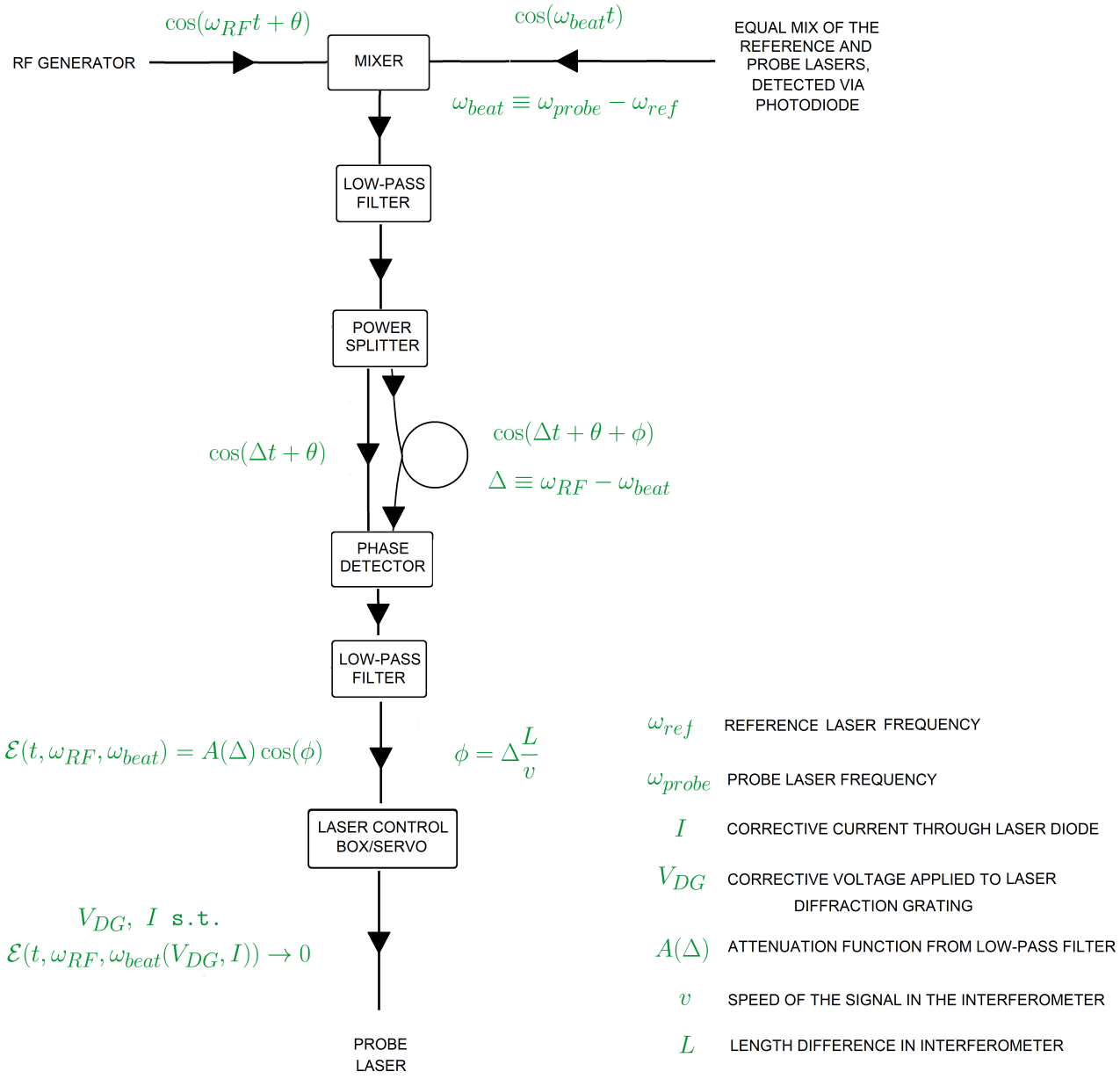

Figure 4.11: Diagram of the frequency offset lock. “S.t.” abbreviates “such that.”

CHAPTER 5

MEASUREMENT OF THE OPTICALLY INDUCED TWO-BODY LOSS RATES

Upon creation of an ultracold gas in which the energy-space spin-lattice may be realized, we test the loss model from § 3 by illuminating the weakly interacting sample with an optical field, frequency-stabilized on the $g \rightarrow e$ transition, and measuring the time-dependent decay of the total atom number $N(t)$. The measurements are obtained for scattering lengths $a_S = 0\,a_0$ to $24\,a_0$ which correspond to interacting strengths of $\zeta = 0$ to 5.4 for the densities used ($N(0) = 6 \times 10^4$, $\sigma^x_{TF} = 330\mu$m, $\sigma^\rho_{TF} = 12\mu$m). As shown in § 3.3 in the absence of loss, there is a phase transition over this range into a magnetized state.

The loss model requires the two-body loss constant K_2^a for a pair of atoms in the anti-symmetric spin state. We extract this value from measurements of $N(t)$ in an incoherent 50-50 mixture of atoms in the $|1\rangle$ and $|2\rangle$ states for each scattering length.

In this chapter, we discuss how the ultracold gas is prepared in the weakly interacting regime in order to realize the lattice, provide the details of the optical field used to induce loss, and reveal the loss measurements and how they compare to the model.

5.1 Preparation of the Gas in the Weakly Interacting Regime

After reaching ultracold temperatures in the optical dipole trap (comprised of a single focused CO_2 laser) via evaporative cooling, the gas is in a 50-50 mixture of ^{6}Li atoms in the

two lowest hyperfine states $|\uparrow\rangle_z \equiv |1\rangle$ and $|\downarrow\rangle_z \equiv |2\rangle$. Evaporative cooling cannot, by definition, occur in the weakly interacting regime, so after evaporation a_s must be magnetically tuned to this regime. Maximum cooling efficiency occurs when a_s is tuned to the broad Feshbach resonance near 832.2 G [Zürn et al. (2013)]. The narrow resonance cannot be used for cooling, as three-body collisions occur, which result in loss. To reach the weakly interacting regime (near 527 G) from the broad Feshbach resonance requires tuning the magnetic field *downward*, which, as we saw in § 2.2.3, results in the formation of Feshbach molecules. This is undesirable, as we lose atoms in the free state. We avoid the formation of Feshbach molecules in a different way for the mixture and the coherently-prepared state, as we discuss below.

5.1.1 Preparation in a Coherent Spin State

To prepare the lattice, the atoms must begin in a coherent spin state in the weakly interacting regime. We first evaporatively cool at the broad Feshbach resonance near 832.2 G [Zürn et al. (2013)] and then raise the trap depth to secure the atoms with a radial trap frequency of $\omega_\rho = 2\pi \times 668.0$ Hz. The magnetic field is then swept *upwards* to 1200 G where the interactions are much weaker, and resonant light is applied to expel one spin state, leaving a $\hat{\mathbf{z}}$-polarized spin sample. The remaining, spin-polarized sample is *non-interacting*, allowing the magnetic field to be swept downward to produce scattering length $a_S(B)$ of interest near 527 G without the formation of Feshbach molecules.

To reach the desired scattering length a_s of interest, we use the known calibration of $a_s(B)$ with the magnetic field B near the weakly interacting regime [Pegahan et al. (2019)].To determine the magnetic field, we perform RF spectroscopy on a $\hat{\mathbf{z}}$-polarized sample for which all atoms are in, say, the $|1\rangle$ state. For a two-level atom subject to an electromagnetic wave that couples the two states together, the probability $P_{1\to2}(t)$ that an atom that starts in a state $|1\rangle$ ends up in a state $|2\rangle$ after a time t is, in the rotating wave approximation,

$$P_{1\to2}(t) = \frac{\Omega_{12}^2}{\Omega_{12}^2 + \Delta^2} \sin^2\left(\frac{t}{2}\sqrt{\Omega_{12}^2 + \Delta^2}\right) \tag{5.1}$$

where Ω_{12} is the Rabi frequency, proportional to the square root of the intensity of the pulse, and Δ is the detuning of the wave frequency ω from the resonance frequency between the two states ω_0 ($\Delta = \omega - \omega_0$). We measure the hyperfine transition frequency ω_0 by fixing $t = \pi/\Omega_{12}$ (which we refer to as a "π-pulse") and varying ω until all atoms are transferred from $|1\rangle$ to $|2\rangle$. This uniquely determines the magnetic field. To coherently prepare the spins

vectors of the atoms orthogonal to the magnetic field, the time of the pulse is cut in half, resulting in a "$\pi/2$-pulse" (then, $P_{1\to 2} = 1/2$). Due to the spin-dependence of the trapping potential, $\Delta = \Delta(E)$. To ensure that atoms of all energies are universally affected by the pulse, we choose $\Omega_{12} = \pi/(2\text{ ms})$, for which $\Omega_{12} >> \Delta(E)$ (since $\max[\Delta(E)] \approx 10$ Hz). The π-pulse is then 1 ms and the $\pi/2$-pulse is then 0.5 ms. The spin-dependence of the trap may be observed by varying ω when Ω_{12} is made comparable to $\Delta(E)$. For $\Omega_{12} \approx \pi/(2 \times 17.3\text{ ms})$, the RF spectrum shows effectively no energy dependence (Fig. 5.1). For $\Omega_{12} \approx \pi/(2 \times 70\text{ ms})$, however, the spin-dependence of the trap becomes apparent in the distorted shape of the spectrum and the inability to fully transfer the atoms into the other state (Fig. 5.2).

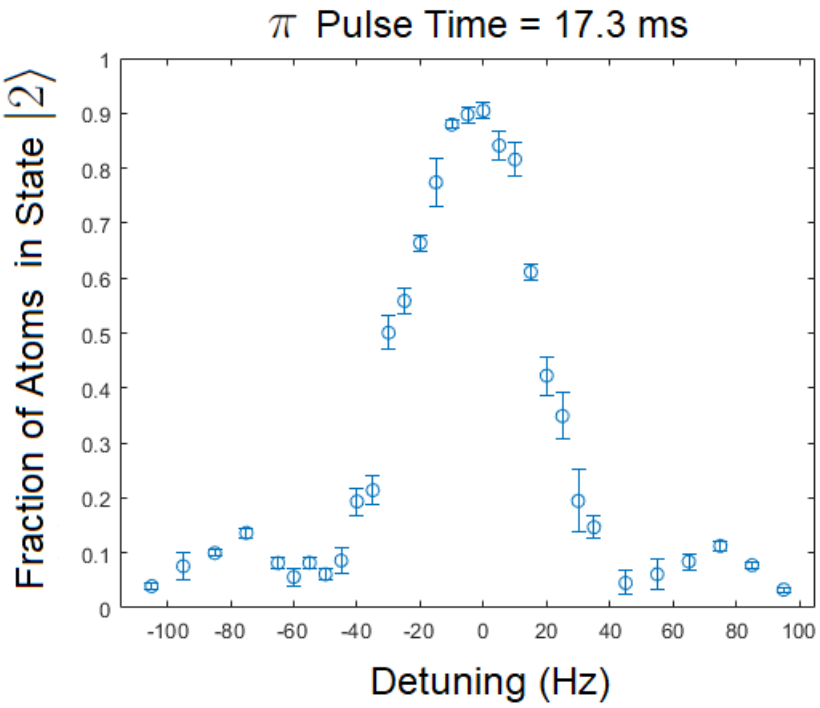

Figure 5.1: RF spectrum for which the time of a π-pulse is ≈ 17.3 ms. The atoms begin in state $|1\rangle$, the pulse is applied, and the number of atoms in state $|2\rangle$ is measured. The axial trap frequency is $\omega_x \approx 2\pi \times 34$ Hz. Each data point is the average of four measurements.

After this preparation, the total number of atoms $N(0) \simeq 6.0 \times 10^4$. A fit of the measured axial profile with a zero-temperature Thomas-Fermi distribution yields an axial width $\sigma^x_{TF} \simeq 331\,\mu$m, Fig. 5.3. The radial width σ^ρ_{TF} is computed from the ratio of trap transverse and axial frequencies, $\omega_\rho \sigma^\rho_{TF} = \omega_x \sigma^x_{TF}$. The curvature in the applied magnetic field results

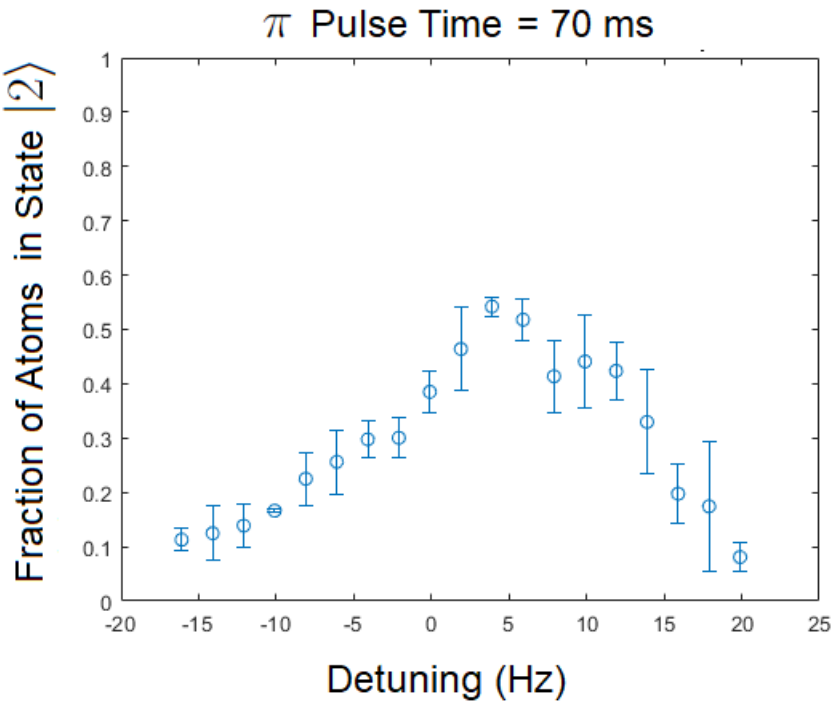

Figure 5.2: RF spectrum under the same conditions described in Fig. 5.1, except that the time for a π-pulse is ≈ 70 ms. The spectrum is noticeably distorted, reflecting the energy-dependence of the resonance frequency.

in an axial trapping force in the axial direction, with a trap frequency $\omega_{mag} = 2\pi \times 16.3$ Hz. For the combined optical and magnetic trapping potentials near 527 G, the net axial trap frequency is measured to be $\omega_x = 2\pi \times 25.0$ Hz. With $\omega_\rho = 2\pi \times 668.0$ Hz, we find $\sigma^\rho_{TF} \simeq 12.0\,\mu$m.

To determine the temperature of this prepared sample, we fit a 1-D finite-temperature Thomas-Fermi distribution to the initial axial profile. The Fermi temperature T_F for our harmonic trap is determined by

$$E_F = k_B T_F = \hbar(6N\omega_\rho^2\omega_x)^{1/3}. \tag{5.2}$$

Note that the 6 in Eq. 5.2 reflects the fact that all N atoms initially begin in an identical spin state. For the initial atom number and trap frequencies given in the last paragraph, we find $T_F \simeq 0.75\,\mu$K. Using the *calculated* Thomas-Fermi radius $\sigma_{TF} = \sqrt{2E_F/(m\omega_x^2)} \simeq 317.0\,\mu$m, a fit to a finite-temperature Thomas-Fermi profiles yields $T \simeq 0.20\,T_F$. Fig. 5.3 shows the averaged initial axial profile for a sample that is coherently prepared at 0 Bohr, along

with the corresponding fitted finite-temperature 1D Thomas-Fermi and zero-temperature 1D Thomas-Fermi profiles. The zero-temperature and finite-temperature Thomas-Fermi profiles are nearly identical, as expected for $T \simeq 0.20\, T_F$, justifying the use of an effective zero-temperature profile with a fitted width in the model.

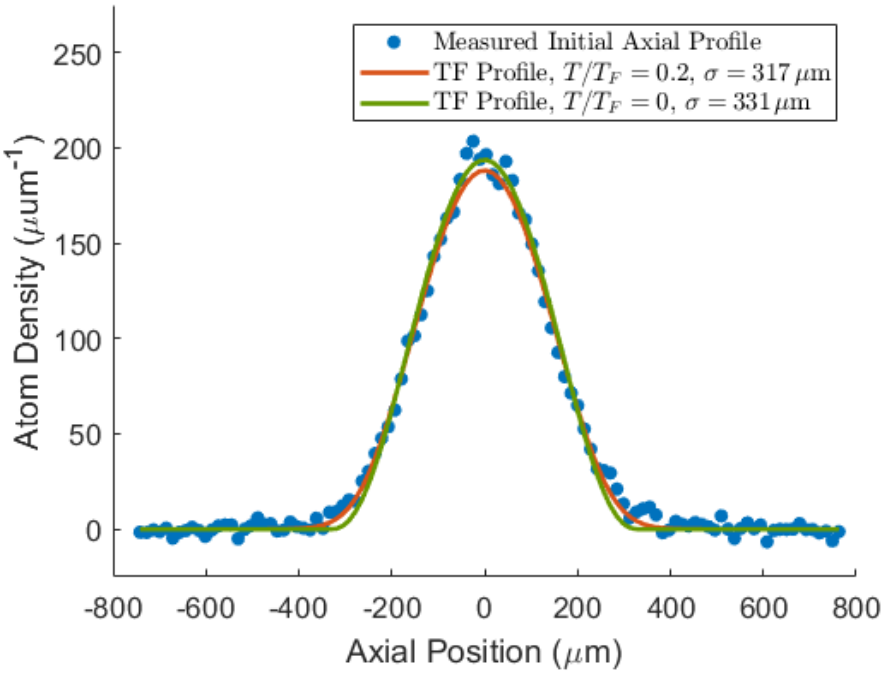

Figure 5.3: Thomas-Fermi fits to the sum of the initial axial profiles of the $|\uparrow_z\rangle$ and $|\downarrow_z\rangle$ states, immediately after the $\pi/2$ pulse, as used for measurement of $N(t)$ at 0 Bohr in the coherently-prepared sample. The fit of a finite-temperature 1D Thomas-Fermi profile yields the reduced temperature $T/T_F = 0.2$. The fit is nearly identical to that of a zero-temperature 1D Thomas Fermi profile, justifying our use to a zero-temperature distribution in the model.

5.1.2 Preparation in an Incoherent 50-50 Mixture

To prepare an ultracold incoherent mixture near the weakly interacting regime, a 50-50 incoherent mixture of atoms in spin states $|\uparrow_z\rangle$ and $|\downarrow_z\rangle$ undergoes evaporative cooling at 300 G. Then the magnetic field is then swept upward, without passing through any resonances, to the magnetic field of interest in the weakly-interacting regime. This method avoids the formation of Feshbach molecules, since the field is never swept though a magnetic field

range where Feshbach molecules form. However, the efficiency of evaporation performed at 300 G, where a_s is small, is reduced compared to that of the unitary gas at 832.2 G. For this reason, the samples used to measure K_2^a are at a higher temperature than for the coherently prepared samples. We assume that K_2^a is temperature independent, as K_2^a is expected to exhibit a weak momentum dependence in the weakly interacting regime. At the magnetic field of interest, the loss-inducing optical field is applied, and the total number of atoms is measured as a function of time. The optical resonance frequency is determined by finding the peak loss point at each magnetic field of interest. Using the measured initial axial width and the initial radial width deduced from the ratio of the trap frequencies, the initial density profile is determined and Eq. 3.92 is used to obtain Eq. 5.5, which is used to determine K_2^a. This procedure is repeated for each scattering length a_S employed in the experiments.

We determine the temperature from a fit of a Maxwell-Boltzmann distribution to the spatial profiles, $k_B T = m\omega_x^2 \sigma_x^2/2$, where σ_x is the fitted Gaussian width. For 15 a_0, this procedure gives $T = 0.56\, T_F$, where $T_F = 0.79\,\mu$K is determined by

$$T_F = \frac{\hbar}{k_B}(3N\omega_\rho^2\omega_x)^{1/3}. \tag{5.3}$$

Note that we have used a factor $3 = 6/2$ in place of the factor 6 in Eq. 5.2, as a 50-50 mixture has half of the total number of atoms N in each spin state. The initial profile with the gaussian fit is shown in Fig. 5.5.

5.2 Illumination of the Gas with the Loss-Inducing Beam

For every scattering length, K_2^a is measured from the loss in a 50-50 mixture, as discussed in § 5.1.2. Loss is induced by an optical beam propagating at an angle of $\simeq 49°$ relative to the trap x-axis (i.e. the direction of the CO_2 beam). The intensity half width at 1/e of the optical beam is $w = 1.1$ mm, so that the projection of the full width of the optical beam at 1/e onto the cloud x-axis, is $2\,w\sin(49°) \simeq 1.5\,w = 1.6$ mm. This can be compared to the full width of the cloud $2\sigma_x \simeq 0.66$ mm. Hence, most of the atoms are illuminated near the peak intensity, $I = P/(\pi w^2)$. The servo-stabilized beam power is 7.6 mW, so that $I = 2.0$ mW/mm^2. The Rabi frequency for the singlet electronic transition from the ground 38$^{\text{th}}$ vibrational state $|g\rangle$ to the excited 64$^{\text{th}}$ vibrational state has been measured [Arunkumar et al. (2019)] to be $\Omega_1/2\pi = 4.4$ MHz $\sqrt{I[\text{mW/mm}^2]}$. The Rabi frequency for the loss inducing beam is then $\Omega_1 = 0.53 \times \gamma_e$, where $\gamma_e = 2\pi \times 11.8$ MHz is the rate of spontaneous emission from the

excited molecular state [Jagannathan et al. (2016a); Wu and Thomas (2012a)].

The optical field is frequency-stabilized on the $g \rightarrow e$ transition using the system described in § 4.2. The tunable frequency offset lock allows the frequency to be adjusted by changing the frequency of a local oscillator (an RF generator). The resonance frequency for each magnetic field value is found by finding the peak loss in the incoherent mixture as a function of frequency, which is prepared as described in § 5.1.2. Since the optical field is locked on resonance, there is no optical shift in the scattering length.

In the coherently-prepared case, illumination occurs after the $\pi/2$ pulse. In the mixture, it occurs whenever the magnetic field has stabilized at the desired value.

5.3 Measurement of Loss in a 50-50 Mixture

To measure the two-body loss constant K_2^a, we measure the decay of the total number of atoms in an incoherent mixture of the $|\uparrow_z\rangle$ and $|\downarrow_z\rangle$ states. We employ a 50-50 mixture for which Eq. 3.92 is valid, with Eq. 3.94 allowing K_2^a to be determined from measurements of $N(t)$. We model $n(\mathbf{r},0)$ as the Maxwell-Boltzmann distribution, which is appropriate for the higher temperature samples used in the mixture measurements,

$$n(\mathbf{r},0) = \frac{N(0)}{\pi\sigma_\rho^2\sigma_x\sqrt{\pi}} e^{-(\rho/\sigma_\rho)^2-(x/\sigma_x)^2}. \tag{5.4}$$

With the axial size σ_x determined from the measured spatial profiles, the radial size σ_ρ is found from the ratio of the trap frequencies. Using the initial density $n(\mathbf{r},0)$ in Eq. 3.94, the measured decay of the total number $N(t)$ determines K_2^a, which is used as a fit parameter. From Eq. 3.94

$$N(t) = \int dx \int 2\pi\rho\, d\rho\, \frac{n(\mathbf{r},0)}{1+\frac{1}{4}K_2^a n(\mathbf{r},0)\, t}. \tag{5.5}$$

Here we expect that K_2^a is independent of temperature, as will be discussed in § 6.1 (see Eq. 6.1).

Measurements of $N(t)$ in 50-50 mixtures are shown in Fig. 5.4 for all of the scattering lengths of interest, using Eq. 3.94 to determine K_2^a. The values extracted from the fit are displayed in Table 5.1, where the uncertainty $\sigma_{K_2^a}$ is determined from the square root of the covariance matrix of the fit (note that this neglects the uncertainty in the initial density). The measured value of K_2^a changes by $\simeq 10\%$ as the scattering length is varied, most likely due to changes in the optical detuning and alignment from run-to-run. We do not expect

K_2^a to be a function of the magnetic field near the zero crossing. Note that the axial widths are smaller for the measurements at 0 and 10 a_0 than for 5, 15, and 24 a_0 (as shown in Table 5.1). The difference arises from the difference between the trap depths used for 0 and 10 a_0, where the trap frequencies were $\omega_\rho = 2\pi \times 1075$ Hz and $\omega_x = 2\pi \times 34$ Hz. The 5, 15, and 24 a_0 data employed the smaller trap frequencies given in § 5.1.1. The faster timescales of loss for the 0 and 10 a_0 measurements reflect the higher density of the sample in the deeper trap.

Eq. 3.93 also predicts the time-dependent axial profiles $n_{1D}(x,t)$, which can be compared to measurements. For the Maxwell-Boltzmann distribution of Eq. 5.4,

$$n_{1D}(x,t) = \int d\rho\, 2\pi\rho\, n(\mathbf{r},\mathbf{t}) = \frac{4\pi\sigma_\rho^2}{K_2^a t} \ln\left[1 + \frac{K_2^a t}{4\pi\sigma_\rho^2} \frac{N(0)}{\sigma_x\sqrt{\pi}} e^{-(x/\sigma_x)^2}\right]. \tag{5.6}$$

In the limit $K_2^a t \to 0$, $n_{1D}(x,t)$ approaches a 1D gaussian distribution normalized to the initial total atom number $N(0)$, as it should. Using the K_2^a determined from the fit to $N(t)$, we find that the predicted axial profiles are in quantitative agreement with the measured profiles, as shown for $a_S = 15\,a_0$ in Fig. 5.5.

Table 5.1: Two-body loss coefficients.

a_S (a_0)	K_2^a (μm^3/s)	$\sigma_{K_2^a}$ (μm^3/s)
0	115	5
5	120	11.6
10	110	6.8
15	138	10
24	136	10

As we discuss below, if the measurements in Table 5.1 are used in the energy-dependent loss rate coefficient $K(E,E',t)$ of Eq. 3.74, however, the loss model does not agree with the measurements in the energy lattice given in § 5.4. To obtain quantitative agreement between predictions and data for coherently prepared samples, we must divide the values of K_2^a measured in the mixture by two. It is possible that we have incorrectly extracted K_2^a by using Eqs. 3.91, 3.92, and 5.5.

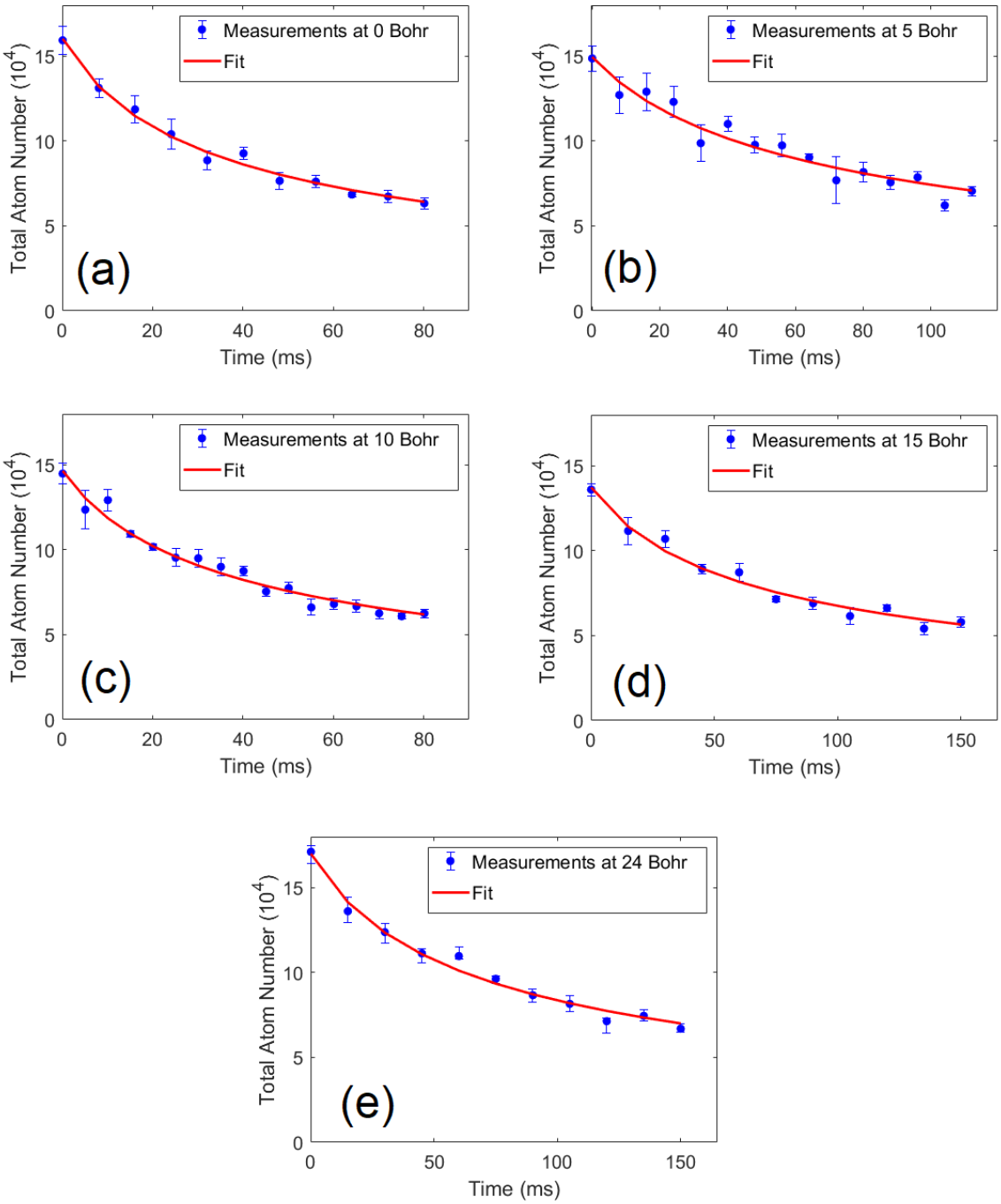

Figure 5.4: Measurements and predictions of loss in the 50-50 mixture at each scattering length. Different trap depths were used for 0 and 10 Bohr ($\omega_\rho = 2\pi \times 1075$ Hz, $\omega_x = 2\pi \times 34$ Hz) than for 5, 15, and 24 Bohr ($\omega_\rho = 2\pi \times 675$ Hz, $\omega_x = 2\pi \times 23$ Hz). (a) Loss at 0 Bohr, with an initial gaussian width 213 μm; (b) loss at 5 Bohr, with an initial gaussian width 241 μm; (c) loss at 10 Bohr, with an initial gaussian width 211 μm; (d) loss at 15 Bohr, with an initial gaussian width 243 μm; (e) loss at 24 Bohr, with an initial gaussian width 260 μm.

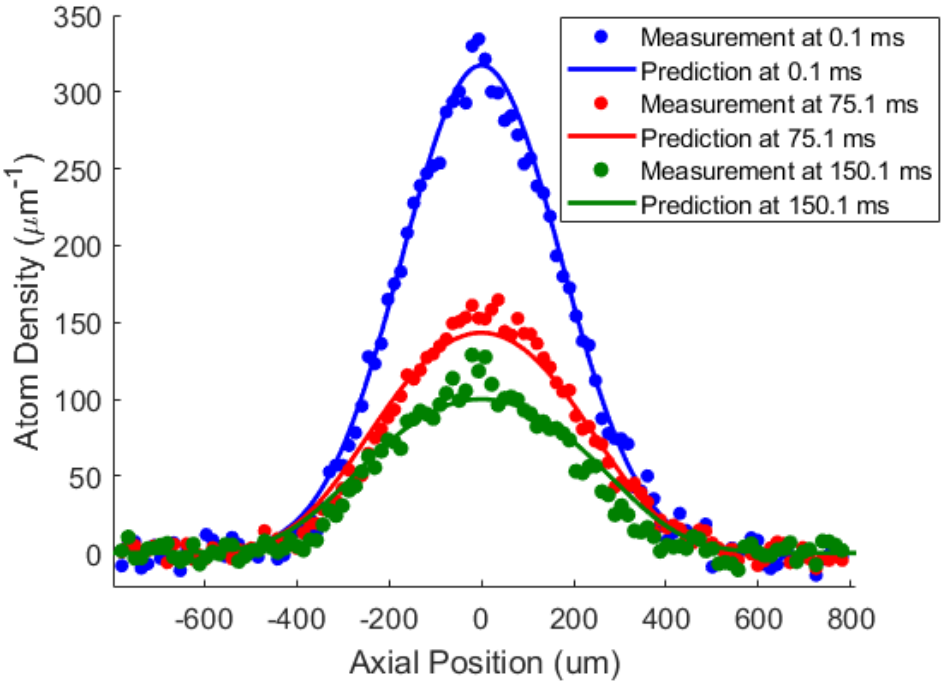

Figure 5.5: Measurements and predictions (Eq. 5.6) for the evolution of the axial profiles in a mixture. The magnetic field is tuned so that $a_S = 15\,a_0$. The two-body loss rate constant $K_2^a = 2 \times 69.0\,\mu\text{m}^3/s$ is determined from the fit of $N(t)$, Eq. 3.94 to the data.

5.4 Measurement of Loss in a Coherently Prepared Sample

To measure loss in the lattice, atoms are illuminated with the loss-inducing beam after the $\pi/2$ pulse is applied to the spin-polarized sample. Measurements are obtained for the scattering lengths $a_s = 0$, 5, 10, 15, and 24 a_0, corresponding to interaction strengths $\zeta = 0$, 1.03, 2.32, 3.59, and 5.39 for our given densities. The fraction of atoms remaining after $\tau = 370$ ms of illumination, $N(\tau)/N(0)$, is shown in Fig. 5.6 for the different scattering lengths. The data demonstrate the phase transition to a magnetized state, and the Fermi suppression more than doubles the number of atoms remaining between the $a_S = 0$ and 24 a_0 cases. Error bars represent the standard deviation of the mean for six shots. The prediction generated by the loss model (red curve) agrees well with the data. For the prediction, we use the averaged atom number, axial widths, and values of K_2^a from the measurements.

Measurements of the fraction of atoms remaining throughout the evolution $N(t)/N(0)$ for coherently prepared samples are shown in Fig. 5.7, along with the corresponding predictions using no free parameters. Predictions and measurements for $a_S = 0\,a_0 (\zeta = 0)$,

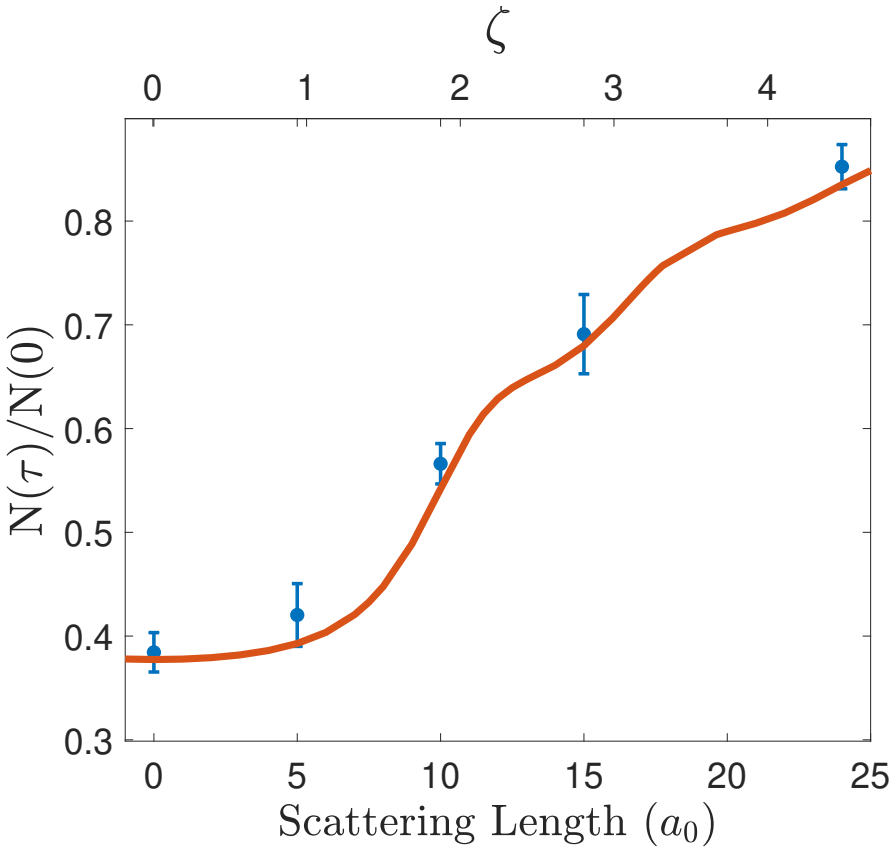

Figure 5.6: Measurements of the atom fraction remaining after τ =370 ms of illumination as the scattering length is increased (blue points), compared to the theoretical prediction (red curve). The densities and values of K_2^a vary slightly for each measurement (see mixture measurements. For the prediction, the averaged values of $N(0) = 6.1 \times 10^4$ atoms, $\sigma_{TF} = 332\,\mu$m, and half of the average measured value of K_2^a, $62\,\mu\text{m}^3/\text{s}$ are used. The data are also plotted with the interaction strength ζ.

where interactions are absent, are shown as a reference, and agree very well. With scattering lengths a_S of 0, 5 ($\zeta = 1.03$), and 10 a_0 ($\zeta = 2.32$), for which the system never becomes strongly magnetized, the atom number is nearly stagnant for the first $\approx$80 ms, corresponding to the time needed for the energy-dependent Zeeman precession rates to separate the collective spin vectors. Once the spin vectors are sufficiently separated, the effective loss rate coefficient $K(E, E', t)$ becomes non-negligible and the atom number begins to decay. At $a_S = 5\,a_0$, the data are almost indistinguishable from the $a_S = 0\,a_0$ case, Fig. 5.7a. This is consistent with Fig. 3.2, where, for $a_S = 5\,a_0$ at our experimental densities, the system is still in the energy-dependent precession-dominated regime. The data show that a phase transi-

tion out of this regime occurs between $a_S = 5\,a_0$ and $a_S = 10\,a_0$, where the measurements at $a_S = 10\,a_0$ exhibit the onset of loss suppression, Fig. 5.7b. The loss is further suppressed for the $a_S = 15\,a_0\,(\zeta = 3.59)$ data, Fig. 5.7c, and even more for the $a_S = 24\,a_0\,(\zeta = 5.39)$ data, Fig. 5.7d, reflecting the increasing collective alignment of the spins, as depicted for the lossless case of Fig. 3.2.

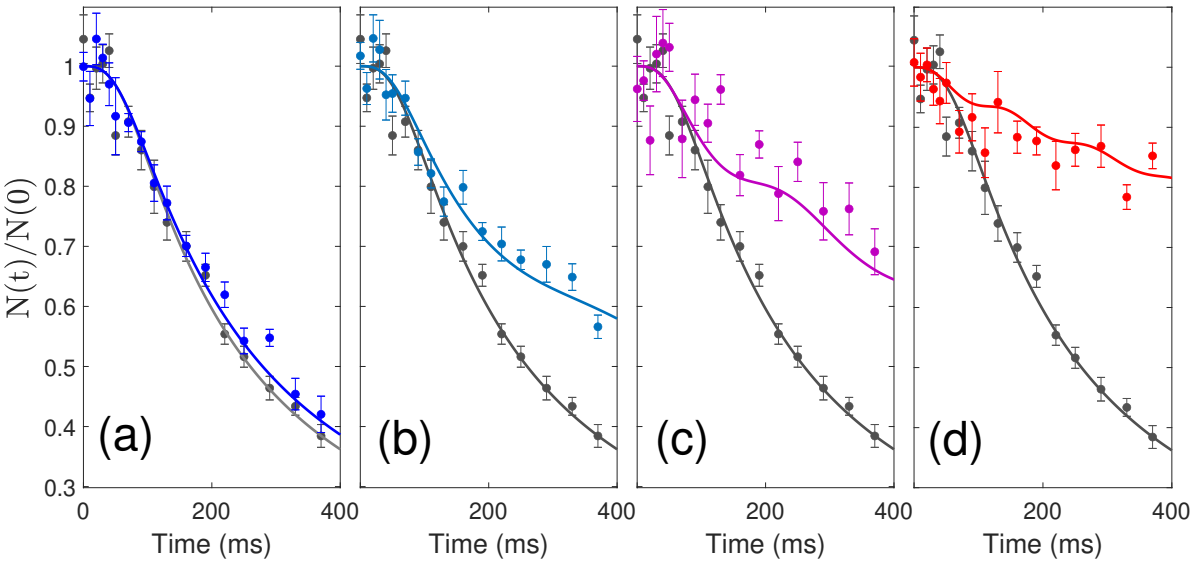

Figure 5.7: Suppression of optically-induced loss versus illumination time as the scattering length is increased. $N(t)/N(0)$ is the atom fraction remaining after a time t. As a reference, the data and model for the non-interacting gas $a_S = 0\,a_0$ ($\zeta = 0$) are shown in black on each plot. Each point represents the average of six shots, and the error bar is the standard deviation of the mean. (a) $a_S = 5\,a_0$ ($\zeta = 1.03$), (b) $a_S = 10\,a_0$ ($\zeta = 2.32$), (c) $a_S = 15\,a_0$ ($\zeta = 3.59$), (d) $a_S = 24\,a_0$ ($\zeta = 5.39$). Note that the interaction strength ζ does not change exactly linearly in the scattering length due to slight variations in the atom number and width. The measured values of K_2^a and exact densities for each scattering length are given in 5.3.

The importance of including the time dependence of the normalized radial density $\mathscr{R}(\rho, t)$ in the model can be seen in the difference between the predictions for $\bar{n}_\perp = \bar{n}_\perp(0)$ and $\bar{n}_\perp = \bar{n}_\perp(t)$ at $a_S = 0\,a_0$, as shown in Fig. 5.8. If $\bar{n}_\perp$ is taken to be constant, the model disagrees with the data for longer times. Accounting for the decrease in $\bar{n}_\perp(t)$ reduces the energy-dependent loss rate $\kappa(E, E', t)$ of Eq. 3.88, causing the tail of the loss curve to rise to

match the data.

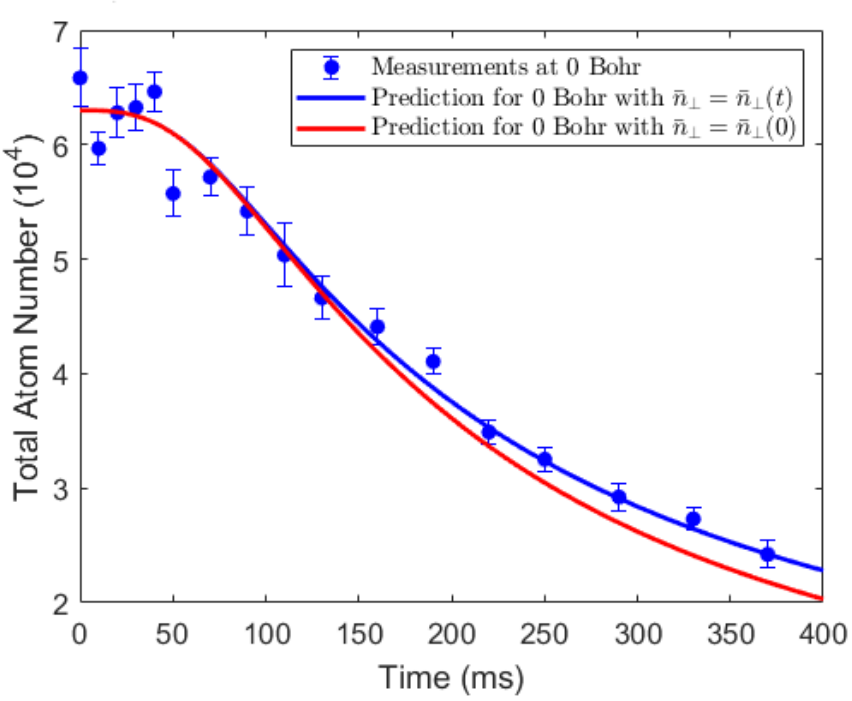

Figure 5.8: Predictions of loss in a coherently-prepared sample, with (blue) and without (red) the time dependence of the average transverse probability density $\bar{n}_\perp$. The time-dependence of $\bar{n}_\perp(t)$ arises from loss. Measurements for 0 Bohr in the coherently-prepared cloud are in agreement with the model when $\bar{n}_\perp = \bar{n}_\perp(t)$ (blue). When $\bar{n}_\perp$ is taken to be constant (red), the tail of the loss curve does not agree with the measurements. For the 0 Bohr data, the inputs into the loss model are $K_2^a = 58.0\,\mu m^3/s$, the initial atom number $N = 6.3\times10^4$ and the width $\sigma_{TF} = 331.0\,\mu$m.

Our collective spin vector model of loss for the energy-space lattice is in good quantitative agreement with measurements. The average of the values of K_2^a used to generate the curves in Fig. 5.7, $62 \pm 6.2\,\mu\text{m}^3/s$, is in good agreement with the predicted value of $69.4\,\mu\text{m}^3/s$. However, we find that the values of K_2^a used in the model need to be *half* of that extracted from measurements in a 50-50 mixture. For the 50-50 mixture, we assume that given pair of atoms collides in a product state, with a probability of 1/2 to be in the antisymmetric spin state , making the extracted K_2^a twice as large. This origin of this discrepancy his not yet clear. Further, we have assumed that the simple two-body loss model used for the mixture measurement may be trivially applied to the weakly interacting regime.

We discuss this factor of two in in § 6.1

CHAPTER 6

CONCLUSION AND OUTLOOK

In summary, we have observed dynamical collective suppression of optically-induced inelastic scattering in a coherently-prepared, weakly-interacting Fermi gas. As the scattering length is increased at fixed initial density, we observe a transition from high to low loss. We understand this suppression via the Pauli principle, where the system makes a transition into a magnetized state with parallel collective spin vectors, Fig. 3.2, causing suppression of s-wave scattering. In this way, loss suppression serves as a new probe of the magnetization of the system. We have developed a loss model that quantitatively agrees with observations and incorporates the many-body evolution of the collective spin vectors. This model explains the loss accompanying the optical tailoring of Hamiltonians in weakly interacting Fermi gases.

6.1 Did we use the Correct K_2^a?

While the loss model agrees very well with the data, we found that we must divide the value of K_2^a that we extract from the measurements in the 50-50 mixture by two. To gather evidence as to whether or not the factor of 1/2 is correct, we can compare the values of K_2^a used to fit the coherently prepared sample in Fig. 5.7 to predictions for the optically-induced loss rate constant in ^{6}Li. We take $K_2^{\text{calc}} = -2 \times \frac{8\pi\hbar}{m} a''$, where $a'' < 0$ is the imaginary part of the scattering length, determined from the complex light-induced phase shift ϕ using $\tan\phi = -ik\,a''$ at the optical resonance. Here, $\hbar k$ is the relative momentum, and we assume $|k\,a''| << 1$ as is the case for our experiments. Note that a factor of two is included

to be consistent with the antisymmetrized hyperfine state of Eq. 3.69 that defines K_2^a, which in turn requires a symmetric spatial state with a total cross section [Bratten and Hammer (2006)] $\sigma_{\rm tot} = 8\pi/k\, Im\{f(0)\}$ and an elastic cross section $\sigma_{\rm el} = 8\pi|f|^2$, with f the s-wave scattering amplitude. The corresponding inelastic cross section $\sigma_{\rm inel} = \sigma_{\rm tot} - \sigma_{\rm el} = 2 \times \frac{\pi}{k^2}(1 - |e^{2i\phi}|^2)$ is *twice* that of Ref. [Jagannathan et al. (2016a)], where the scattering atoms were treated as distinguishable and a factor 4π was used in the cross sections. The supplementary material of Ref. [Jagannathan et al. (2016a)] determines a'' using $x = k|a_{bg}|$ and $\tilde{\Delta}_0 = (B - B_\infty)/\Delta B = -1$ in Eq. S5, which gives $L(\tilde{\Delta}_0, x) \simeq 1$ in Eq. S8 of Ref. [Jagannathan et al. (2016a)], yielding

$$K_2^{\rm calc} = 2 \times \frac{8\pi\hbar|a_{bg}|}{m} \frac{\hbar\gamma_e}{4\mu_B \Delta B}\, \tilde{\Omega}_1^2, \tag{6.1}$$

where $\tilde{\Omega}_1 \equiv \Omega_1/\gamma_e$. With the parameters of Ref. [Bartenstein et al. (2005)], $a_{bg} = -1405\, a_0$, $\Delta B = 300$ G, and $\mu_B/\hbar = 2\pi \times 1.4$ MHz/G, $\gamma_e = 2\pi \times 11.8$ MHz we find $K_2^{\rm calc} = 277.4\, \mu{\rm m}^3/s\, \tilde{\Omega}_1^2$, which gives $K_2^{\rm calc} = 69.4\, \mu{\rm m}^3/s$ at $\tilde{\Omega}_1 = 0.5$ as used in the measurements. This result is in good agreement with the value $K_2^a = 69\, \mu{\rm m}^3/s$ that fits the decay of the coherently prepared sample at $15\, a_0$, but is, however, *half* the value $K_2^a = 138\, \mu{\rm m}^3/s$ extracted from measurements in the 50-50 mixture using Eq. 3.92 as noted above. At present, we are unable to resolve this discrepancy, which may arise from applying Eq. 3.92 to a very weakly interacting mixture or from an incorrect choice of the incoming two-atom state in deriving Eq. 3.92.

6.2 Prospects for Control of the Lattice

With the effect of the loss on the evolution successfully modeled, optical control can be applied to the lattice. In the absence of optical control, the site-to-site couplings $g(E, E')$ (see Eq. 3.59) can only be adjusted (beyond a simple scale factor) by putting the atoms in a different trap. With the spatial resolution offered by optical control, the couplings can be tailored as $a_s \to a_s(x)$, yielding

$$g(E, E') = \frac{8\pi\hbar}{m} \bar{n}_\perp \int dx\, |\phi_E(x)|^2 |\phi_{E'}(x)|^2\, a_s(x). \tag{6.2}$$

For instance, if the beam is shone only on the edges of the trap, then only the high-energy atoms can interact, and only the high-energy collective spin vectors can couple together. Further, focusing the beam on the center of the trap would cause the interactions between

atoms with *even* quantum numbers to dominate.

Optical control also allows for studies of information scrambling [Pegahan et al. (2021)] in this system to be extended. In Ref. [Gärttner (2017)], spatial control of interactions was suggested as a way to "experimentally study scrambling behavior in regimes intractable to theory, to explore the possibility of fast scrambling in low temperature systems, and to investigate possible connections between chaos and fast scrambling away from the semi-classical limit."

Further manipulation of the site-to-site couplings may be achieved by temporal modulation. Note that in Eq. 3.61, if the Zeeman term dominates, $\hat{\mathbf{S}}(E) \approx \cos[\Omega_B(E)t]\hat{\mathbf{x}}' + \sin[\Omega_B(E)t]\hat{\mathbf{y}}'$, where $\Omega_B(E) = \frac{\delta\omega_x}{\bar{\omega}_x}E$. Consider varying the scattering length in time so that $a_s \rightarrow a_s \cos[\frac{\delta\omega_x}{\bar{\omega}_x}(E-E')t]$. Time-averaging, *only groups of energies which differ by $E-E'$ will be coupled*. This is possible with the temporal resolution offered by optical control, but it may also be possible to achieve using purely magnetic control of the scattering length.

It may be possible to pair these different schemes for tailoring the site-to-site couplings with site-to-site preparation. In § 5.1.1, we noted that the 0.5 ms $\pi/2$ pulse used to coherently prepare the spin vectors orthogonal to the applied magnetic field affects each energy group identically. As Ω_{12} is made smaller and smaller in comparison to $\Delta(E)$ in Eq. 5.1, it becomes theoretically possible to rotate specific energy groups in the lattice.

Finally, we note that the lattice can be made to evolve from a state in which all of the vectors are spread out, as opposed a state in which they are all aligned, by keeping $a_s = 0$ after the $\pi/2$ pulse. The energy-dependent precession rate will cause the vectors to fan out in the plane orthogonal to the magnetic field. If interactions are introduced at this stage, the $\mathbf{S}(E) \times \mathbf{S}(E')$ terms begin with a non-zero value.

6.3 Thoughts on Why the Lattice Model Fails

In Ref. [Pegahan et al. (2019)], the energy-space spin-lattice model was seen to reproduce observation in the spin density profiles well during segregation, but for longer times in the magnetized phase, the model failed. As discussed in § 3.3.1, the oscillations occur as the vectors continuously align, then spread, then align again, and so on (see Fig. 3.2). This oscillation in the length of the total spin vector is manifested in an oscillation of the center of the difference between the spin density profiles. These observed oscillations appeared to be *damped*. It was suggested that the apparent decay in the oscillations was simply due to the averaging over measurements for which the phase of the oscillation differed. However,

the individual measurements do not exhibit the expected variation over the predicted full amplitude of the oscillation. This has yet to be explained. Here we discuss this breakdown of the lattice model.

According to the model, the oscillations arise as the spin vectors begin to align, which causes the $\mathbf{S}(E') \times \mathbf{S}(E)$ term in Eq. 3.61 to decay, which allows the $\mathbf{\Omega_B}(E) \times \mathbf{S}(E)$ term to separate the vectors, which again allows the interaction term to bring them to come back together, and so on (as discussed in § 3.3.1). The oscillation of the central density difference between the spin profiles is the spatial testament to this behavior in energy space. At lower interaction strengths, the Zeeman precession dominates and there is no oscillation, resulting in a steady-state to the central spin density difference. To understand the mismatch of the model with the observations in real space, we can use these intuitions to think of the behavior in energy space.

We outline three possibilities: (1) the effect is not a consequence of the natural evolution of the system, but an artifact of some experimental issue, (2) the basic premise of evolving classical collective spin vectors is correct, but some adjustment must be made to the spin vector evolution equations, or (3) this premise does not apply for longer times.

For the first possibility, perhaps some fluctuations in the magnetic field or CO_2 beam interfer with the "natural" evolution of the system. This seems unlikely: during my PhD, I performed an experiment in which the system began to segregate and then stopped, as I used a set of auxilary coils to change the magnetic field so that $a_s = 0$. During this time without interactions, the profiles were stationary. After some waiting time, I turned off the auxiliary coils, restoring the original a_s: the system then began evolving as expected, right where it left off. If there was some "junk effect" in the experimental conditions, we would have expected that the point at which the mismatch with the model happens is a function of the *overall time* of the experiment. However, the result suggests that it is only a function of the *time during which the system interacts*.

For the second possibility, it is difficult to see how the decay in the oscillation can be accounted for by any adjustments to Eq. 3.61. We could imagine that the the basic form of the rotation equations remains correct, but the $g(E, E')$ term somehow decays, so that the system breaks out of the oscillating phase and back to the stationary phase. However, a lower interaction term (i.e., a lower a_s) is associated with a *larger* central spin density difference— a decay of the $g(E, E')$ term would result in an *increase* in the central density difference before it "flattens out," which is not observed. If the vectors do not simply rotate, then the lengths of the vectors would have to change. This, however, does not appear to be consistent in the absence of loss. Another consideration is that the mismatch with the

model only arises after segregation— is there some consequence of the spatial separation of spin states? Could there be an energetic cost to segregating? Further, if the issue is a matter of dissipation, then where would the energy go? And while the "damping of the oscillations" tempts one to add a dissipative term to the evolution equation, the central density difference doesn't decay to zero— it reaches some steady state.

The third possibility is the most open-ended. We can revisit into the assumptions that were made in the model. Perhaps energy-changing collisions happen more often than we think, and the collective spin vector picture becomes inappropriate at these higher times. This, however, is inconsistent with the calculations. Or perhaps everything is right, but the "classical" part is wrong— we neglected quantum effects (note that $\langle \hat{\mathbf{s}}_1 \times \hat{\mathbf{s}}_2 \rangle = \langle \hat{\mathbf{s}}_1 \rangle \times \langle \hat{\mathbf{s}}_2 \rangle$ only when entangled states are negelected). However, quantum-mechanical model suffers from a combinatorial explosion and its predictions cannot be calculated. Furthermore, quantum effects seem unlikely, as there are hundreds of atoms which comprise each collective spin vector.

We consider the most likely possibility to be that the collective spin vector picture becomes less and less appropriate as the system evolves is the magnetized phase in which the length of the total spin vector oscillates. Note that we assumed that the approximation in Eq. 3.53 that $\bar{n}_\perp^{jk} \approx \langle \bar{n}_\perp^{jk} \rangle_{jk} = \bar{n}_\perp$ is valid. If this assumption is not made, then the axial-energy-dependent collective spin vector picture loses its validity and we would instead have to consider the evolution of each atom at its position in a *three-dimensional* energy-space spin lattice. The differing rotation rates for each atom comprising the collective spin vector would cause the vector to break apart. This would effectively lower the effect of the interactions, causing a transition back into the phase dominated by the energy-dependent Zeeman precession. This could explain the decay in the oscillation in the central spin density profiles. A simulation with a three-dimensional lattice could be used to see if this theory begins quantitatively with the experiments. An experiment to test this hypothesis could build off of this thesis— note that the suppression of the loss serves as a probe of the magnetization. The loss-inducing beam could be made to illuminate the sample after the system begins to segregate in the magnetized phase. The loss could then be measured, and the suppression observed. The results should be predicted by the loss model in § 3.4. Then, another experiment could be run in which the system evolves until the oscillations die out, after which the loss-inducing beam illuminates the sample. If the loss is not suppressed, this provides evidence that the sample is in the Zeeman-dominated phase.

REFERENCES

Abraham, E. R. I., McAlexander, W. I., Gerton, J. M., Hulet, R. G., Côté, R., and Dalgarno, A. (1997). Triplet s-wave resonance in ^{6}Li collisions and scattering lengths of ^{6}Li and ^{7}Li. *Phys. Rev. A*, 55:R3299–R3302.

Arunkumar, N. (2018). *Designer Optical Control of Two-body Interactions in Ultracold Gases*. PhD thesis.

Arunkumar, N., Jagannathan, A., and Thomas, J. E. (2018). Probing energy-dependent feshbach resonances by optical control. *Phys. Rev. Lett.*, 121:163404.

Arunkumar, N., Jagannathan, A., and Thomas, J. E. (2019). Designer spatial control of interactions in ultracold gases. *Phys. Rev. Lett.*, 122:040405.

Bartenstein, M., Altmeyer, A., Riedl, S., Geursen, R., Jochim, S., Chin, C., Denschlag, J. H., Grimm, R., Simoni, A., Tiesinga, E., Williams, C. J., and Julienne, P. S. (2005). Precise determination of ^{6}Li cold collision parameters by radio-frequency spectroscopy on weakly bound molecules. *Phys. Rev. Lett.*, 94:103201.

Bauer, D., Lettner, M., Vo, C., Rempe, G., and Dürr., S. (2009). Control of a magnetic feshbach resonance with laser light. *Nature Physics*, 5:339–342.

Bratten, E. and Hammer, H.-W. (2006). Universality in few-body systems with large scattering length. arxiv.org/abs/cond-mat/0410417v3.

Campbell, G. K., Boyd, M. M., Thomsen, J. W., Martin, M. J., Blatt, S., Swallows, M. D., Nicholson, T. L., Fortier, T., Oates, C. W., Diddams, S. A., Lemke, N. D., Naidon, P., Julienne, P., Ye, J., and Ludlow, A. D. (2009). Probing interactions between ultracold fermions. *Science*, 324(5925):360–363.

Clark, L. W., Ha, L.-C., Xu, C.-Y., and Chin, C. (2015). Quantum dynamics with spatiotemporal control of interactions in a stable bose-einstein condensate. *Phys. Rev. Lett.*, 115:155301.

Deb, A. B. and Kjærgaard, N. (2021). Observation of Pauli blocking in light scattering from quantum degenerate fermions. *Science*, 374:972.

Deppner, C., Herr, W., Cornelius, M., Stromberger, P., Sternke, T., Grzeschik, C., Grote, A., Rudolph, J., Herrmann, S., Krutzik, M., Wenzlawski, A., Corgier, R., Charron, E., Guéry-Odelin, D., Gaaloul, N., Lämmerzahl, C., Peters, A., Windpassinger, P., and Rasel, E. M. (2021). Collective-mode enhanced matter-wave optics. *Phys. Rev. Lett.*, 127:100401.

Drever, Hall, and *et al.* (1983). Laser phase and frequency stabilization using an optical resonator. *Appl. Phys. B*, 31:97–105.

Du, X., Luo, L., Clancy, B., and Thomas, J. E. (2008). Observation of anomalous spin segregation in a trapped Fermi gas. *Phys. Rev. Lett.*, 101:150401.

Fedichev, P. O., Kagan, Y., Shlyapnikov, G. V., and Walraven, J. T. M. (1996). Influence of nearly resonant light on the scattering length in low-temperature atomic gases. *Phys. Rev. Lett.*, 77:2913–2916.

Georgescu, I. M., Ashhab, S., and Nori, F. (2014). Quantum simulation. *Rev. Mod. Phys.*, 86:153–185.

Gibble, K. (2009). Decoherence and collisional frequency shifts of trapped bosons and fermions. *Phys. Rev. Lett.*, 103:113202.

Gärttner, M., B. J. S.-N. A. e. a. (2017). Measuring out-of-time-order correlations and multiple quantum spectra in a trapped-ion quantum magnet. *Nature Physics*, page 781–786.

Hazzard, K. R. A. and Gadway, B. (2023). Synthetic dimensions. *Physics Today*, 76(4):62–63.

Huang, J. and Thomas, J. E. (2023). Decoding transverse spin dynamics by energy-resolved correlation measurement. arXiv:2309.07226 [cond-mat.quant-gas].

Huang, J. and Thomas, J. E. (2024). Energy-resolved spin correlation measurements: Decoding transverse spin dynamics in weakly interacting fermi gases.

Jagannathan, A. (2016). *Optical Control of Magnetic Feshbach Resonances by Closed-Channel Electromagnetically Induced Transparency*. PhD thesis.

Jagannathan, A., Arunkumar, N., Joseph, J. A., and Thomas, J. E. (2016a). Optical control of magnetic Feshbach resonances by closed-channel electromagnetically induced transparency. *Phys. Rev. Lett.*, 116:075301.

Jagannathan, A., Arunkumar, N., Joseph, J. A., and Thomas, J. E. (2016b). Optical control of magnetic feshbach resonances by closed-channel electromagnetically induced transparency. *Phys. Rev. Lett.*, 116:075301.

Jannin, R., van der Werf, Y., Steinebach, K., Bethlem, H. L., and Eikema, K. S. E. (2022). Pauli blocking of stimulated emission in a degenerate Fermi gas. *Nature Communications*, 13:6479.

Koller, A. P., Wall, M. L., Mundinger, J., and Rey, A. M. (2016). Dynamics of interacting fermions in spin-dependent potentials. *Phys. Rev. Lett.*, 117:195302.

Lewandowski, H. J., Harber, D. M., Whitaker, D. L., and Cornell, E. A. (2002). Observation of anomalous spin-state segregation in a trapped ultracold vapor. *Phys. Rev. Lett.*, 88:070403.

Margalit, Y., Lu, Y.-K., Top, F. , and Ketterle, W. (2021). Pauli blocking of light scattering in degenerate fermions. *Science*, 374:976.

Marinescu, M. and You, L. (1998). Controlling atom-atom interaction at ultralow temperatures by dc electric fields. *Phys. Rev. Lett.*, 81:4596–4599.

Moerdijk, A. J., Verhaar, B. J., and Nagtegaal, T. M. (1996). Collisions of dressed ground-state atoms. *Phys. Rev. A*, 53:4343–4351.

Oktel, M. O. and Levitov, L. S. (2002). Internal waves and synchronized precession in a cold vapor. *Phys. Rev. Lett.*, 88:230403.

Pegahan, S., Arakelyan, I., and Thomas, J. E. (2021). Energy-resolved information scrambling in energy-space lattices. *Phys. Rev. Lett.*, 126:070601.

Pegahan, S., Kangara, J., Arakelyan, I., and Thomas, J. E. (2019). Spin-energy correlation in degenerate weakly interacting Fermi gases. *Phys. Rev. A*, 99:063620.

Rey, A. M., Gorshkov, A. V., and Rubbo, C. (2009). Many-body treatment of the collisional frequency shift in fermionic atoms. *Phys. Rev. Lett.*, 103:260402.

Sanner, C., Sonderhouse, L., Hutson, R. B., Yan, L., Milner, W. R., and Ye, J. (2021). Pauli blocking of atom-light scattering. *Science*, 374:979.

Savard, T. A., O'Hara, K. M., and Thomas, J. E. (1997). Laser-noise-induced heating in far-off resonance optical traps. *Phys. Rev. A*, 56:R1095–R1098.

Schnemann, Engler, Grimm, and *et al.* (1999). Simple scheme for tunable frequency offset locking of two lasers. *Review of Scientific Instruments*, 70.

Smale, S., He, P., Olsen, B. A., Jackson, K. G., Sharum, H., Trotzky, S., Marino, J., Rey, A. M., and Thywissen, J. H. (2019a). Observation of a transition between dynamical phases in a quantum degenerate fermi gas. *Science Advances*, 5(8):eaax1568.

Smale, S., He, P., Olsen, B. A., Jackson, K. G., Sharum, H., Trotzky, S., Marino, J., Rey, A. M., and Thywissen, J. H. (2019b). Observation of a transition between dynamical phases in a quantum degenerate Fermi gas. *Science Advances*, 5(8). elocation-id: eaax1568.

Townes, A. (1955). Stark effect in rapidly varying fields. *Phys. Rev.*, 100:703–722.

Wu, H. and Thomas, J. E. (2012a). Optical control of Feshbach resonances in Fermi gases using molecular dark states. *Phys. Rev. Lett.*, 108:010401.

Wu, H. and Thomas, J. E. (2012b). Optical control of the scattering length and effective range for magnetically tunable feshbach resonances in ultracold gases. *Phys. Rev. A*, 86:063625.

Yu, Z. and Pethick, C. J. (2010). Clock shifts of optical transitions in ultracold atomic gases. *Phys. Rev. Lett.*, 104:010801.

Zener, C. (1932). Non-Adiabatic Crossing of Energy Levels. *Proceedings of the Royal Society of London Series A*, 137(833):696–702.

Zürn, G., Lompe, T., Wenz, A. N., Jochim, S., Julienne, P. S., and Hutson, J. M. (2013). Precise characterization of ^{6}Li Feshbach resonances using trap-sideband-resolved rf spectroscopy of weakly bound molecules. *Phys. Rev. Lett.*, 110:135301.

APPENDIX

APPENDIX A

THE HYPERFINE STRUCTURE OF LITHIUM-6

Consider a ^{6}Li atom in a magnetic field $\mathbf{B}$. The nucleus has a spin quantum number $I = 1$. To describe the spin interactions, we consider only the nucleus, with a spin operator $\hat{\mathbf{I}}$ and the single valence electron, with an intrinsic spin operator $\hat{\mathbf{s}}$. We include contributions from the hyperfine interaction, the interaction of the intrinsic electron spin with the field, and the interaction of the intrinsic nuclear spin with the field to obtain the Hamiltonian

$$\hat{H} = A_{HF}\hat{\boldsymbol{I}}_{\boldsymbol{j}} \cdot \hat{\boldsymbol{S}}_{\boldsymbol{j}} + C_e \hat{\boldsymbol{S}}_{\boldsymbol{j}} \cdot \mathbf{B} - C_n \hat{\boldsymbol{I}}_{\boldsymbol{j}} \cdot \mathbf{B} \tag{A.1}$$

where $C_e > 0$ and $C_n > 0$. Note that we have neglected spin-orbit coupling, since, for the alkali atoms, the valence electron has $\ell = 0$. In this section, we determine the eigenstates and the eigenvalues of H.

We work in the basis $|m_s\, m_I\rangle$, where $m_s \in \{-1/2, 1/2\}$, $m_I \in \{-1, 0, 1\}$ and

$$\hat{S}_z\,|m_s\, m_I\rangle = m_S\,|m_s\, m_I\rangle \tag{A.2}$$

$$\hat{I}_z\,|m_s\, m_I\rangle = m_I\,|m_s\, m_I\rangle \tag{A.3}$$

The z direction is defined by the magnetic field direction. We may express the spin operators in the other directions as

$$\hat{S}_x = \frac{1}{2}(\hat{S}_+ + \hat{S}_-) \tag{A.4}$$

$$\hat{S}_y = \frac{1}{2i}(\hat{S}_+ - \hat{S}_-) \tag{A.5}$$

where

$$\langle s, m_s' | \hat{S}_+ | s, m_S \rangle = \delta_{m_s', m_s+1} \sqrt{s(s+1) - m_s m_s'} \tag{A.6}$$

$$\langle s, m_s' | \hat{S}_- | s, m_s \rangle = \delta_{m_s', m_s-1} \sqrt{s(s+1) - m_s m_s'} \tag{A.7}$$

and likewise for the $\hat{I}_x$ and $\hat{I}_y$ operators.

We may then express $\hat{H}$ as

$$\hat{H} = \hat{H}_D + \hat{H}_{OD} \tag{A.8}$$

where

$$\hat{H}_D = A_{HF} \hat{S}_z \hat{I}_z + C_e B \hat{S}_z - C_n B \hat{I}_z \tag{A.9}$$

$$\hat{H}_{OD} = \frac{1}{2} A_{HF} (\hat{S}_+ \hat{I}_- + \hat{S}_- \hat{I}_+) \tag{A.10}$$

Note that $\hat{H}_{OD}$ is symmetric. Now, $\hat{H}_{OD} |\max(m_s)\max(m_I)\rangle = \hat{H}_{OD} |\min(m_s)\min(m_I)\rangle = 0$. Then, $|1/2, 1\rangle$ and $|-1/2, -1\rangle$ are eigenstates of $\hat{H}$

$$\hat{H} |1/2, 1\rangle = \hat{H}_D |1/2, 1\rangle = E_{++} |1/2, 1\rangle \tag{A.11}$$

$$\hat{H} |-1/2, -1\rangle = \hat{H}_D |-1/2, -1\rangle = E_{--} |-1/2, -1\rangle \tag{A.12}$$

where

$$E_{++} = \frac{1}{2} A_{HF} + \left(C_n - \frac{1}{2} C_e \right) B \tag{A.13}$$

$$E_{--} = \frac{1}{2} A_{HF} - \left(C_n - \frac{1}{2} C_e \right) B \tag{A.14}$$

Which leaves us with four more eigenvectors and eigenvalues.

Now, note that when $\hat{H}_{OD}$ operates on

$$|\phi_{m_I}\rangle = c^+_{m_I} |1/2, m_I\rangle + c^-_{m_I} |-1/2, m_I'\rangle \tag{A.15}$$

it does not couple to other $|m_s, m_I\rangle$ states if $m_I' = m_I + 1$. This means that m_I can be either -1 or 0. With two orthonormal states for both $m_I = -1$ and $m_I = 0$, all four other eigenstates of $\hat{H}$ are accounted for. We then search for the values of the coefficients in the above equations, as well as the eigenvalues E_{m_I}

$$\hat{H} |\phi_{m_I}\rangle = E_{m_I} |\phi_{m_I}\rangle . \tag{A.16}$$

This results in

$$c^{\pm}_{m_I} = \frac{A_{HF}\,\eta_{m_I}/2}{E_{m_I} \mp A_{HF}\,m_I^{\pm}/2 + B\,C_n\,m_I^{\pm} \mp C_e\,B/2}\,c^{\mp}_{m_I} \tag{A.17}$$

where $\eta_{m_I} \equiv \sqrt{1(1+1) - m_I(m_I+1)}$, $m_I^+ = m_I$, and $m_I^- = m_I + 1$. Note that $\eta_{-1} = \eta_0 = \eta = 2$. The eigenvalues are then

$$E_{m_I} = -\frac{1}{2}(\Gamma_{m_I} + \Gamma'_{m_I}) \pm \frac{1}{2}\sqrt{(\Gamma_{m_I} - \Gamma'_{m_I})^2 + A_{HF}^2\,\eta^2} \tag{A.18}$$

where

$$\Gamma_{m_I} = -\frac{1}{2}A_{HF}\,m_I + B\,C_n\,m_I - \frac{1}{2}B\,C_e \tag{A.19}$$

$$\Gamma'_{m_I} = \frac{1}{2}A_{HF}\,(m_I+1) + B\,C_n(m_I+1) + \frac{1}{2}B\,C_e. \tag{A.20}$$

The eigenvalues simplify to

$$E_{m_I} = -\frac{A_{HF}}{4} - \frac{B\,C_n}{2}(2m_I+1) \pm \frac{A_{HF}}{2}R_{m_I} \tag{A.21}$$

where

$$R_{m_I} = \sqrt{Z_{m_I}^2 + \eta} \tag{A.22}$$

and

$$Z_{m_I} = -(C_e + C_n)B/A_{HF} - (m_I + 1/2). \tag{A.23}$$

We may then obtain the eigenstates associated with each of the four eigenvalues.

We consider the electron to be in its ground state, for which $C_e = 2.002\mu_B$, where μ_B is the Bohr magneton. The hyperfine coupling constant for this state is $A_{HF} = 152.137$ MHz $\times h$. The nucleus has $C_n = +0.000448\mu_B$. In order of increasing energy, the eigenstates are

$$\begin{aligned}
|1\rangle &= \sin\theta_0\,|1/2\,0\rangle - \cos\theta_0\,|-1/2\,1\rangle \\
|2\rangle &= \sin\theta_{-1}\,|1/2\,-1\rangle - \cos\theta_{-1}\,|-1/2\,0\rangle \\
|3\rangle &= |-1/2, -1\rangle \\
|4\rangle &= \cos\theta_{-1}\,|1/2\,-1\rangle + \sin\theta_{-1}\,|-1/2\,0\rangle \\
|5\rangle &= \cos\theta_0\,|1/2\,0\rangle + \sin\theta_0\,|-1/2\,1\rangle \\
|6\rangle &= |1/2, 1\rangle
\end{aligned} \tag{A.24}$$

with eigenvalues

$$
\begin{aligned}
E_1 &= -\frac{A_{HF}}{4} - \frac{BC_n}{2} - \frac{A_{HF}}{2} R_0 \\
E_2 &= -\frac{A_{HF}}{4} + \frac{BC_n}{2} - \frac{A_{HF}}{2} R_{-1} \\
E_3 &= \frac{A_{HF}}{2} - C_n B + \frac{C_e B}{2} \\
E_4 &= -\frac{A_{HF}}{4} + \frac{BC_n}{2} + \frac{A_{HF}}{2} R_{-1} \\
E_5 &= -\frac{A_{HF}}{4} - \frac{BC_n}{2} + \frac{A_{HF}}{2} R_0 \\
E_6 &= \frac{A_{HF}}{2} + C_n B - \frac{C_e B}{2}
\end{aligned}
\tag{A.25}
$$

where

$$
\begin{aligned}
&\sin\theta_j = 1/\sqrt{1+(Z_j+R_j)^2/2} \\
&\sin^2\theta_j + \cos^2\theta_j = 1 \\
&R_j = \sqrt{Z_j^2+2} \\
&Z_0 = -(C_e+C_n)B/A_{HF} - 1/2 \\
&Z_{-1} = -(C_e+C_n)B/A_{HF} + 1/2.
\end{aligned}
\tag{A.26}
$$

These energy eigenvalues are plotted in Fig. 2.2 as a function of B.